INFERRING ICE CLOUD PROPERTIES FROM POLARIZED SUB-MILLIMETER MICROWAVE AND INFRARED SPACEBORNE OBSERVATIONS

A Dissertation

by

ADAM D. BELL

Submitted to the Office of Graduate and Professional Studies of
Texas A&M University
in partial fulfillment of the requirements for the degree of

DOCTOR OF PHILOSOPHY

Chair of Committee,	Ping Yang
Committee Members,	Kenneth Bowman
	Anita Rapp
	Michael Bishop
Head of Department,	R. Saravanan

May 2021

Major Subject: Atmospheric Sciences

ABSTRACT

Ice clouds account for significant uncertainties in our understanding of the current climate as well as our ability to predict future changes. The high spatiotemporal variability of ice clouds coupled with their unique microphysical and macrophysical properties, makes modelling efforts difficult. To reduce uncertainties associated with modeled ice cloud properties, it is essential to have long-term global measurements of ice cloud characteristics. Previous studies have shown a measurement gap exists in ice cloud sensitivity and could potentially be filled by sub-millimeter (sub-mm) wave measurements.

We present a retrieval algorithm based on the optimal estimation framework designed to retrieve ice cloud properties, which combines sub-mm and infrared (IR) radiometric and polarimetric measurements. Sub-mm and IR observations of ice clouds are complementary and exploit ice particle scattering that effectively modulates the upwelling background radiation from water vapor. The primary retrieval quantities are cloud ice water path (*IWP*), ice particle effective diameter (D_{eff}), including optional cloud top height. A novel part of this algorithm is that it utilizes polarized brightness temperatures (*TBs*) in both the high-frequency sub-mm and IR wavelength regimes, of which there is a lack of studies exploring the benefits. A state-of-the-art database of cloud ice optical properties is incorporated into the Atmospheric Radiative Transfer Model (ARTS) to stochastically simulate *TBs* from CloudSat observations over the tropics, which we use to conduct retrieval experiments. Retrieved cloud properties are

compared to the true values and statistically analyzed. Information content in measured *TBs* is also used to evaluate retrieval performance and is expressed quantitatively in terms of degrees of freedom for signal (*DOF*) and Shannon Information Content (*SIC*). Although retrieval precision varies with cloud scene, the algorithm is demonstrated to effectively infer *IWP* and D_{eff} over a wide range of cloud and atmospheric conditions and shows the best performance for clouds with moderate to low *IWP* and D_{eff}.

ACKNOWLEDGEMENTS

I would like to thank my advisor, Dr. Yang, for providing me the opportunity to attend graduate school and learn from the incredible scientists at Texas A&M University, as well as those at domestic and international conferences. I would also like to thank Dr. Yang and my committee members, Dr. Bowman, Dr. Rapp, and Dr. Bishop, for their guidance and support throughout the course of this research and in times of great difficulty.

Thanks go out to my friends and colleagues for their valuable discussions concerning this research project, and the department faculty and staff for making my graduate life at Texas A&M University a great experience. I am especially grateful to Dr. Souichiro Hioki and Dr. Masanori Saito for their extraordinary mentorship and kind encouragements. I would also like to thank Dr. Dong Wu, Dr. Patrick Stegmann, Dr. Guanglin Tang, and Mr. James Coy for their valuable discussions regarding radiative transfer and retrieval techniques. Lastly, I would like to thank my partner for all her love and support.

CONTRIBUTORS AND FUNDING SOURCES

Contributors

This work was supported by a dissertation committee consisting of Professors Ping Yang, Kenneth Bowman, and Anita Rapp of the Department of Atmospheric Sciences, and Professor Michael Bishop of the Department of Geography.

A significant portion of this research was conducted with advanced computing resources provided by Texas A&M High Performance Research Computing.

All other work conducted for this dissertation was completed by the student independently

Funding Sources

The research efforts reported in this dissertation were supported by NASA Earth and Space Science Fellowship (NESSF, 80NSSC17K0363).

TABLE OF CONTENTS

Page

LIST OF FIGURES

Page

LIST OF TABLES

Page

1. INTRODUCTION

1.1. Climate Change

As the world population rapidly approaches eight billion people and significant portions begin or continue the push for industrialization, it is more important now than ever to solidify our understanding of the current climate, so that we may better predict what the future holds, particularly through the lens of globalization. Although we are terrestrial beings, our impacts on the Earth can be spread, often perniciously, through the Earth-atmosphere system. Not unlike other dynamic systems in nature, the atmosphere exhibits significant spatiotemporal variability. We experience rapid variability of atmospheric properties, such as pressure, humidity, and precipitation as weather. Localized, long term (typically decades) statistics of the weather define the climate.

It is evident that the Earth's climate is changing. Previous studies incorporating both models and measurements showed that global average temperatures are increasing, and precipitation patterns are evolving (Soloman et al., 2007). Additionally, studies which focused more on the attribution of the aforementioned changes showed they are caused by anthropogenic influences (Hegerl et al., 2007). The most recent 5th Assessment Report by the Intergovernmental Panel on Climate Change (IPCC) noted that the human influence on the climate system is clear, with anthropogenic emissions of greenhouse gasses at the highest point in history, and that recent climate changes have widespread impacts both on human and natural systems (IPCC, 2014). For these reasons, it is imperative that we have a rigorous understanding of the climate system.

1.2. Importance of ice cloud characterization/measurements

Ice clouds account for significant uncertainties in our understanding of the current climate as well as our ability to predict future changes. In part, this is because they have unique microphysical (e.g., cloud optical thickness, ice particle shape/size) and macrophysical (e.g., cloud top height/temperature, total ice mass, cloud horizontal extent) properties (Liou, 1986). While liquid water is sometimes present, ice clouds are primarily composed of ice particles which occur in very complex shapes and consequently increase the difficulty of modeling studies. Also distinct to ice clouds is their location. Their high altitude contributes to their differing radiative properties, as compared to other clouds. Because of these inherent difficulties in modeling ice clouds, they continue to be an ongoing focus of atmospheric remote sensing (Xie et al., 2011).

Although it is well documented that ice clouds modulate the Earth's radiative budget, the overall impact ice clouds have on the climate system remains unclear. One difficulty in discerning the net effect of ice clouds on the Earth's energy budget is their large spatiotemporal variability. Ice clouds cover at least 20% of the Earth at any given moment, and up to 60 – 70% in the tropics (Buehler et al., 2007). This variability, coupled with their unique microphysical properties, yields a strong but conflicting influence on the radiation budget. Ice clouds contribute to warming of the atmosphere through the absorption and re-emission of outgoing longwave infrared radiation, referred to as the greenhouse effect. Conversely, ice clouds reflect incoming shortwave radiation, consequently cooling the atmosphere. This is referred to as the albedo effect. Thus, the net radiative effect of ice clouds is a function of their macrophysical and microphysical

properties (Liou, 1986; Ramaswamy and Ramanathan, 1989). Therefore, a holistic understanding of these ice cloud properties is paramount to achieve the robust modeling necessary to accurately quantify their net radiative effect, and subsequently understand their current and future climactic impact.

1.3. Representation of ice clouds in climate models

As previously mentioned, ice clouds can have opposing impacts on the Earth's radiation budget by means of the greenhouse and albedo effects, and these mechanisms account for a significant source of uncertainty in modeling and estimating climate sensitivity. The net magnitude and sign of these feedbacks in global climate models (GCMs) are almost exclusively determined by model assumptions (Stephens, 2005). Clouds in GCMs can be generally described by four factors or properties, all of which should be realistically represented: cloud cover, cloud optical thickness, cloud water mass, and cloud particle sizes. Therefore, to successfully model ice clouds for radiation budget considerations, we need independent and accurate knowledge of the above properties, which serve as model tuning parameters.

A particular parameter of importance is cloud ice mass per unit volume of air, called ice water content (*IWC*), or its counterpart integrated through the depth of the cloud, referred to as ice water path (*IWP*). There exist significant discrepancies in *IWC*/*IWP* among GCMs, which can differ by as much as an order of magnitude, particularly in the tropics (John and Soden, 2006; Waliser et al., 2009; Eliasson et al., 2011; Li et al., 2012). This is highlighted in Fig. 1.1 taken from John and Soden (2006) (left panel) and Eliasson el al. (2011) (right panel), which both show zonal averages of

IWP for different climate models. These inter-model discrepancies are chiefly a function of differing model assumptions or parameterizations regarding the representation of ice cloud microphysical and optical properties. Microphysical processes in ice clouds are complex and have significant variation in space and time, and consequently those endeavoring to model them must make a trade-off between computational expense and the degree to which they include physically realistic ice cloud processes. An important objective for climate modeling is to correctly model the energy budget. However, our current understanding of clouds is insufficient, and consequently balancing the energy budget is often detrimental to the realism of the modeled cloudiness. Until we have significantly improved our understanding of cloud behavior, the bulk amount of cloud is used as a prognostic variable (Sundqvist, 2002).

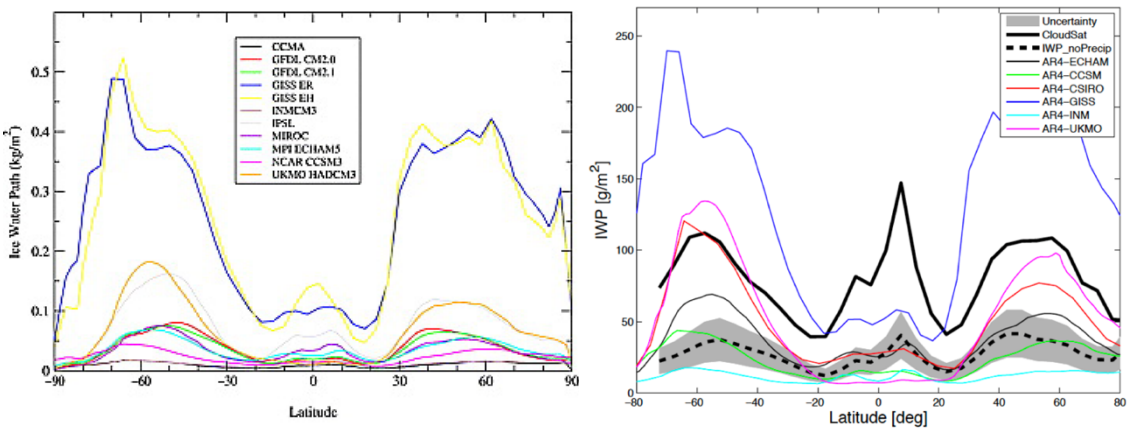

Figure 1.1: Zonal annual mean IWP from various climate models in IPCC AR4 data archive. Left: The climatology of zonal annual mean *IWP* from various climate models in the IPCC AR4 data archive. From John and Soden (2006). Right: Zonal averages of *IWP* for climate models from 100 years of monthly mean data. Reprinted from Eliasson et al., 2011.

There are several issues models must overcome concerning cirrus clouds. For instance, models face problems generating ice clouds because the processes which generate them are poorly resolved. This is especially the case in the tropics, where synoptic scale water vapor and cirrus are initially produced from microscale processes. These processes must be parameterized, which leads to large uncertainties (DelGenio, 2002). There are additional issues arising not only from the generation of ice clouds, but also the vertical transport of water vapor and formation of ice cloud particles. The former is an issue of vertical resolution (i.e., too few atmospheric layers). The latter is a function of relative humidity and assumptions regarding ice/cloud condensation nuclei (i.e., aerosol content). Further details regarding the shortcomings of the representation of cirrus clouds in models are beyond the scope of this thesis, and the reader is directed to DelGenio (2002) and references therein.

It logically follows that in order to minimize the uncertainties associated with cirrus clouds in climate models, the current necessary assumptions (e.g., ice particle size and mass) must be constrained by long term global measurements, or a climatology, of ice cloud characteristics. However, studies such as that conducted by Waliser et al. (2009) emphasize the deficiency of available cloud property measurements, which can be used to constrain the models. While there exist global and continuous datasets of satellite retrieved cloud properties, using them to constrain or validate climate models is far from trivial for many reasons (Eliasson et al., 2011). The inconsistency of ice mass among models and difficulty in validating ice mass in models and reanalyses using satellite observations is highlighted in Fig. 1.2, taken from Li et al. (2012). The figure

shows the vertical distribution of ice mass in terms of cloud ice water content (CIWC) and total ice water content (TIWC), from models and reanalyses (Fig. 1.2a-s) that specifically provide output on cloud ice. From the figure it is evident that some models capture similar magnitudes of IWC but fail to represent the spatial distribution. For example, the two GFDL models (Fig. 1.2n-o) both capture the ITCZ in tropical regions but show a significant underestimation of ice mass in the extratropical storm tracks. Observations are also provided in Fig. 1.2t-w for comparison to the models.

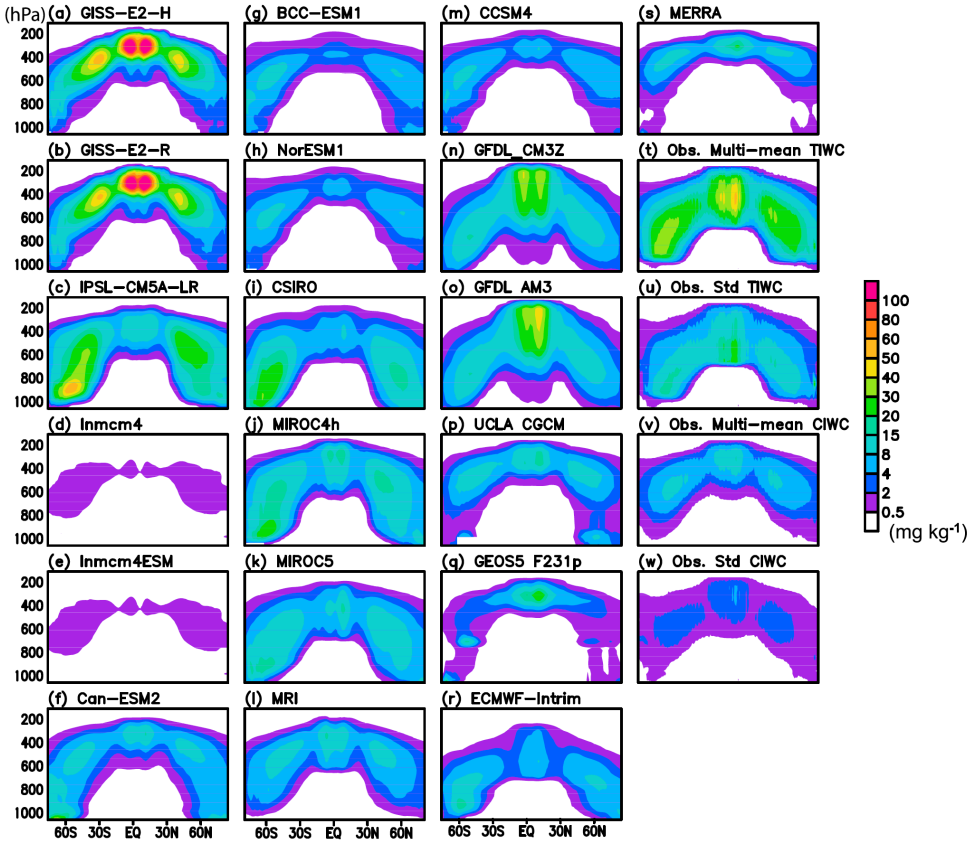

Figure 1.2: Zonally averaged annual mean CIWC from GCM simulations in CMIP5 (a-m). Also shown is TIWC from GFDL (n) CM3 and (o) AM3, CIWC from (p) UCLA CGCM, (q) NASA GEOS5, (r) ECMWF-Interim reanalysis, (s) MERRA reanalyses as well as the (t) ensemble-mean and (w) observed estimate standard deviation of four CIWP observed estimates. Reprinted from Li et al., 2012.

A primary obstacle in using satellite retrieved cloud properties to validate and constrain models is actually the definition of *IWP* and the treatment of clouds and precipitation in models, which explicitly separate ice cloud particles into precipitating particles and suspended particles. Conversely, retrieved *IWP* typically includes both suspended and precipitating particles (Waliser et al., 2009). Although satellite derived *IWP*s are defined in the same fashion, there are significant differences among existing datasets. These differences arise from differing characteristics inherent in satellite retrievals, such as the portion of the electromagnetic spectrum from which the measurements are taken (i.e., microwave to visible), active versus passive measuring, the viewing angle (i.e., nadir versus limb), and microphysical assumptions (i.e., ice particle shape and size distribution). Because there are fundamental differences in measurement techniques, they exhibit sensitivity to distinct parts of the cloud column. Notwithstanding the differing definitions of *IWP* between models and satellite retrievals, if there is a gap in sensitivity to a particular part of the cloud column or cloud microphysical conditions, observation to model comparisons will continue to be ambiguous. Therefore, we must ensure that any existing observational gaps in ice cloud sensitivity are filled so that we have a more holistic representation of global ice cloud characteristics in which to validate and constrain model *IWP*. Evidence for the existence of such a gap and the need for additional observations to fill it is provided in subsequent sections.

1.4. Satellite remote sensing of ice clouds

Observing Earth from space has been a significant motivator for launching satellites ever since the first successful weather satellite (Television InfraRed Observation Satellite, TIROS) was launched in 1960 (Stroud 1960). Since then, there have been numerous satellites launched for myriad applications, but all with the same general goal of sensing (i.e., observing) the Earth from space. Scientists and scholars have fervently analyzed these observations (or measurements) and sought to extract information from them to better understand atmospheric, terrestrial, and oceanic properties. Satellite measurements are now a critical tool by which we can glean information on the world around us, and current continuous monitoring has facilitated substantial advancements in our understanding of weather processes and the climate system. Furthermore, global remote sensing provides an important constraint on parameterizations used in models for both weather and climate applications.

In the most general sense, remote sensing hinges on our understanding of electromagnetic radiation and the manner in which it interacts with various constituents in the Earth-atmosphere system. More specifically in the case of using passive satellite remote sensing to infer cloud property information, satellites detect radiation of a particular wavelength (or frequency) that is then combined with some known physics of the objects of interest (e.g., ice clouds), and from the two we can infer something about certain properties of these objects (e.g., cloud ice mass). Although this inference, or retrieval, of cirrus cloud properties relies on several assumptions which are briefly mentioned below, we can identify and estimate the properties of cirrus clouds and clouds

in general from satellite measurements using two approaches: *active* and *passive remote sensing*. The discussion of remote sensing provided here only extends to passive remote sensing, and therefore is not a comprehensive overview of satellite remote sensing.

Remote sensing based on wavelengths from the visible to the microwave have been used to observe and infer ice cloud properties for decades now. Numerous past studies utilized measurements from the ground, airplanes, and satellites to characterize ice cloud microphysical and radiative properties. A detailed discussion of how ice clouds interact with atmospheric radiation is provided in Chapter 2. Regardless of the measurement type and retrieval technique, it can be challenging to infer even the most basic physical ice cloud parameters, such as ice mass and particle size distribution (PSD) from remote sensing measurements. A fundamental reason this is the case is because there is no analytical solution to the radiative transfer equation (introduced in Chapter 3). Even if this were not the case it still relies on a number of assumptions, such as the presence of local thermodynamic equilibrium (LTE), that radiation is monochromatic (i.e., at one wavelength/frequency), that scattering of radiation by atmospheric media is elastic (i.e., no change in wavelength/frequency with scattering), and that the cloud is vertically and horizontally homogeneous. Assumptions notwithstanding, the inversion from the measurements to cloud properties (retrieval) can also be problematic. For example, the inversion can be an ill-posed problem where you have too many unknowns and not enough measurements. This problem is discussed in greater detail in Chapter 4.

The aforementioned difficulties of relating satellite measurements to ice cloud properties are more general and extend to other remote sensing applications. There are

also complications more specifically related to inferring even basic physical properties of ice clouds, such as ice mass and PSD. One concern is that an instrument measuring radiation in a specific area of the electromagnetic spectrum is the most sensitive to ice particle sizes proportionate to the wavelengths used. The natural variability of ice particle size ranges from μm to cm, so it follows that using measurements from wavelengths most sensitive to only a discrete subset of the PSD can lead to uncertainties in retrieved properties. For example, if one is using visible, infrared, and millimeter wave measurements (i.e., sensitive to the ends of the PSD), it follows that inferred ice mass from these measurements would be erroneous. More simply put, in order to deduce ice mass from measurements we need assumptions on the complete PSD, and if our measurements can only "see" a particular portion of the PSD then our inferred ice mass is not representative of the full PSD of ice particles within the cloud (Rydberg et al., 2007).

1.5. Scope of this research and thesis objectives

The overarching goal of this work is to better understand the interaction of sub-mm radiation with ice clouds, and subsequently how observations in this spectral region can be leveraged to improve ice cloud property retrievals for the purpose of constraining and/or validating these parameters within models. The primary focus is on improving quantification of ice cloud properties in the tropics, particularly the column density of ice, or *IWP*, from simulated spaceborne measurements in the sub-mm spectral region, since models and existing measurements can vary by as much as an order of magnitude. As high frequency sub-millimeter microwave (frequencies greater than ~300 GHz)

spaceborne measurements are not yet available, the strategy to accomplish the aims of this work involves generating physically representative synthetic data with the aid of a radiative transfer simulator. Furthermore, we conduct a series of numerical experiments concerning the sensitivity of sub-mm radiation to various ice cloud properties, with an emphasis on polarization signals due to ice clouds, in order to select the most appropriate sensing frequencies. With insight from these experiments, we develop an optimal estimation-based inversion framework suitable for nonlinear problems in order to reliably infer ice cloud properties from our synthetic data.

This work is intended to provide insights into the characterization of ice cloud properties with sub-mm spaceborne measurements for the benefit of upcoming launches of sub-mm radiometers by NASA, as well as other international agencies. More broadly, the research presented here aims to contribute to one of NASA's overarching goals in Earth Science: *advance the understanding of the change in Earth's radiation balance…that result from changes in atmospheric composition.*

This thesis is organized as follows: Chapter 2 provides a brief overview of ice cloud observations in the sub-mm spectral region, as well as physical insights into the interaction of sub-mm radiation with ice clouds. This chapter also introduces the polarization of sub-mm radiation scattered by ice clouds.

Chapter 3 presents a brief discussion of the theoretical background of scattering, formally defines polarization and introduces the concept of the Stokes vectors. This chapter also defines the single scattering properties and includes a brief overview of the vector radiative transfer equation.

Chapter 4 introduces the radiative transfer simulator used as the forward model and describes the setup in the context of this work. This chapter also includes discussions of channel selection, the polarization signal due to ice clouds, and the methods for generating synthetic data. Lastly, it outlines the optimal estimation-based retrieval framework and introduces the concept of information content.

Chapter 5 presents some of the aforementioned numerical experiments to demonstrate the sensitivity of sub-mm radiances to properties of cloud ice particles, such as the refractive index and shape.

Chapter 6 provides more rigorous discussion on the polarization signals of ice clouds in the sub-mm spectral region in the context of ice cloud property retrievals. This chapter also details how ice particle orientation impacts cloud polarization signals and discusses the potential of inferring particle orientation from polarized spaceborne measurements.

Chapter 7 demonstrates and compares ice cloud property retrievals for various sets of sub-mm and IR channels, both with and without including polarized measurements.

Chapter 8 presents the overall summary and conclusions of this thesis, particularly in the context of the stated aims and goals of this research. Thoughts on the future of sub-mm remote sensing of ice cloud properties are also presented in brief.

2. REMOTE SENSING

2.1. Introduction

The discussion presented in Chapter 1 emphasized the importance of providing a climatology of global remotely sensed ice cloud properties to constrain and validate climate models. There are many existing remote sensing techniques which operate at wavelengths from the visible to microwave that have been used to fill this need. However, as briefly mentioned in the previous chapter, not all measurement wavelengths are sensitive to the same size of particles in the cloud, or even the same portions of the cloud. The two previous statements are demonstrated in Fig. 2.1, which combines figures from Waliser et al. (2009) and Eliasson et al. (2011) and shows the various measurement methods for estimated cloud ice water path (*IWP*) as well as the vertical location in the cloud in which these measurement techniques exhibit the highest sensitivity.

As is evident from the right panel of Fig. 2.1, techniques developed to infer ice cloud properties in the infrared and visible (IR+VIS) are sensitive to the uppermost layer of thick clouds. Previous studies have shown that these techniques are reliable for thin ice clouds but tend to saturate for moderate to large amounts of cloud ice (Wu et al., 2008). An advantage of active measurements is that they can provide information on the vertical profile, however they only provide limited spatial coverage. For example, active visible techniques such as the Cloud-Aerosol Lidar with Orthogonal Polarization (CALIOP) have a footprint of 333 m (Winkler et al., 2010), and active microwave

techniques (RADAR) such as the CloudSat radar have a footprint of 1.4 km (Stephens et al., 2008). It is also evident from the figure that lidar is primarily applicable to thin clouds. Conversely, passive and active microwave measurements can penetrate thick clouds and provide information on the vertical structure of ice within the cloud. This is because the wavelengths in the microwave spectrum are roughly proportional to the sizes of frozen hydrometeors and are sensitive to ice particles (Wu et al., 2008). However, current passive spaceborne microwave instruments are confined to frequencies less than 190 GHz (wavelengths greater than ~1.5 mm) and are therefore most sensitive to large frozen hydrometeors such as snow, and much less sensitive to small ice particles.

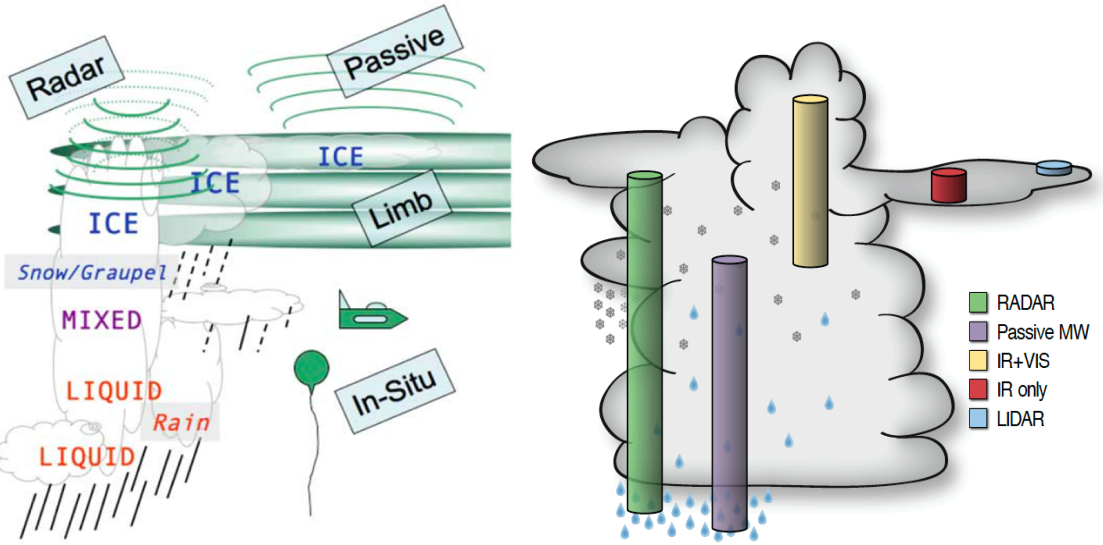

Figure 2.1: Diagram illustrating ice water content/ice water path (*IWC*/*IWP*) measurement methods (left). Reprinted from Waliser et al., 2009. Schematic figure of a thick cloud, where columns indicate approximately where in the vertical cloud the different measurements are sensitive (right). Reprinted from Eliasson et al., 2011.

Due to the significant differences in characteristics and sensitivities of the techniques mentioned above, it is reasonable to assume that they would provide different values of *IWP*. This large variance in estimated *IWP* is shown in Fig. 2.2, taken from Eliasson et al. (2011), which shows the zonally averaged *IWP* over oceans for several different satellite datasets. When comparing this figure to Fig. 1.2, you can see there is more consistency in *IWP* among observations than models, but the observed values still differ significantly. As these differences increase, so does the difficulty in using them to constrain and validate model output. It is important to note here the difficulty in comparing satellite datasets of retrieved *IWP*, which is in large part due to the uncertainty in estimating the cloud top height and base from these retrievals. Based on the previous discussion of the relation of particle size and wavelength used to the particle's scattering properties, this should be no surprise (i.e., large wavelengths have difficulty detecting thin cirrus clouds and visible/infrared wavelengths detect more thin cirrus but saturate for thick clouds).

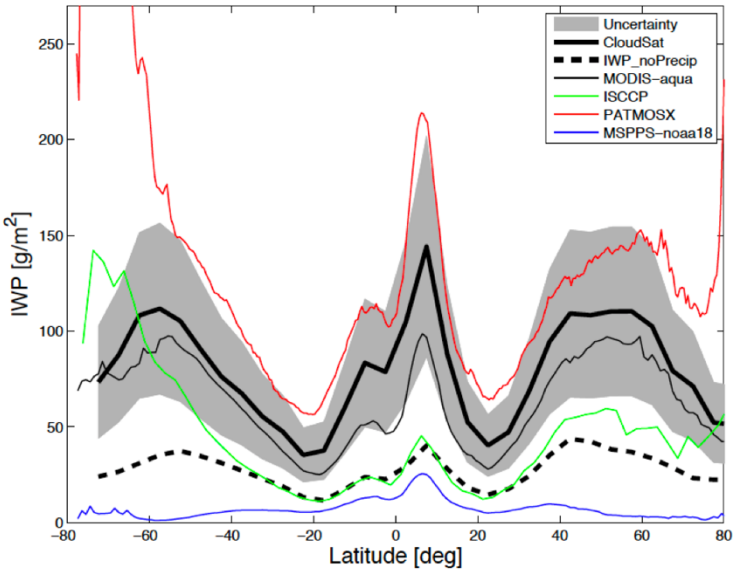

Figure 2.2: Zonally averaged *IWP* of satellite datasets over ocean. Date range is July 2006 to April 2008. The grey shaded area represents an uncertainty interval, estimated to be 40% (Heymsfield et al., 2008). Reprinted from Eliasson et al., 2011.

There are additional shortcomings to techniques leveraging the aforementioned spectral ranges. For example, *IWP* products derived using measured reflected solar radiation are only applicable during the daytime, have high sensitivity only to particles at the top of the cloud, and saturate for moderate amounts of cloud ice. Thermal infrared methods are sensitive to larger particle sizes and *IWP*, but still saturate for clouds with moderate optical thickness and *IWP*s. In contrast, current active and passive microwave methods are insensitive to optically thin clouds (i.e., smaller particles and lower *IWP*) (Jiminez et al., 2007). Thus, our existing remote sensing measurements utilizing the visible, infrared, and microwave (e.g., less than 190 GHz (~ 1.5 mm) passive and 94 GHz (~3 mm) active) spectral regions leave a gap in sensitivity between infrared (small ice particles) and microwave (large ice particles). Furthermore, as previously mentioned if we use measurements that are only sensitive to a discrete portion of the PSD, then the

estimated ice mass will only be representative of this portion of the PSD. Therefore, this gap in sensitivity between small and large ice particles also produces a lack of sensitivity to moderate *IWP* values (e.g., ~100 – 200 g/m^2). In order to obtain the necessary globally retrieved ice cloud parameters to constrain and validate the models, we need additional measurements to fill this gap in ice cloud sensitivity.

2.2. Sub-mm observations of ice clouds

Previous studies have investigated the performance of various subsets of sub-millimeter (sub-mm) measurements to fill the gap in ice cloud sensitivity (Gasiewski, 1992; Evans and Stephens, 1995a, b; Evans et al., 1998, 1999, Maio et al., 2002). For the purpose of observing high ice clouds with smaller particles, the Submillimeter-Wave Cloud Ice Radiometer (SWCIR) was developed by JPL to fly on the NASA DC-8 and observe cloud ice using channel frequencies up to 643 GHz. A study by Evans et al. (2002) demonstrated that the retrieval algorithm developed for SWCIR had an overall median retrieval errors of ~30% for *IWP* and ~15% for median mass equivalent sphere diameter. A subsequent sub-mm sensor, the Compact Scanning Submillimeter Imaging Radiometer (CoSSIR), was deployed during the Cirrus Regional Study of Tropical Anvils and Cirrus Layers (CRYSTAL) Florida Area Cirrus Experiment (FACE) campaign in 2002. CoSSIR utilized a combination of mm and sub-mm wave channels up to 640 GHz. While the sub-mm channels were noisier than expected, which led to poorer sensitivity to lower *IWP* clouds, the observations of CoSSIR further confirmed that the higher frequency sub-mm channels had an increased sensitivity to ice particle size than their lower frequency counterparts. An additional result of this study was the suggestion

of including an 874 GHz channel to improve the sensitivity to ice clouds comprised of smaller ice particles.

Although the above instruments are airborne, NASA has been making a significant effort for decades to advance spaceborne sub-mm technologies for remote sensing of ice clouds. Recently, NASA leveraged emerging CubeSat opportunities to develop IceCube, which is an 883 GHz radiometer aboard a 3U CubeSat that was launched from the International Space Station (Wu et al., 2019). IceCube produced the first global map of *IWP* from a spaceborne nadir sub-mm sensor. NASA is also funding a follow up mission SWIRP: Compact Submm-Wave and LWIR Polarimeters, which will use three channels in the mm (220 GHz), sub-mm (323, 424, 680 GHz), and IR (12 μm) bands. It is necessary to mention that sub-mm spaceborne measurements (above 200 GHz) are not entirely new. Several limb sounders have employed sub-mm frequencies around 600 GHz to observe ice clouds, such as the Microwave Limb Sounder aboard the Aura satellite (Wu et al., 2009), the Odin Sub-Millimetre Radiometer (Odin-SMR; Murtagh et al., 2002), and the Superconducting Submillimeter-Wave Limb-Emission Sounder (SMILES; Kikuchi et al., 2010) instruments. Limb viewing instruments however are beyond the scope of this work and more details can be obtained in the references above.

There are additional noteworthy studies which focused on sub-mm radiometry, such as that by Di Michele and Bauer (2006) which explored channels from 5 to 200 GHz and determined that suitable frequency bands differ for rain over land, clouds over ocean, and snow over land and ocean. Jiminez et al. (2007) took a different approach and

investigated an instrument that employed measurements around water vapor lines (183, 325, and 448 GHz) and window channels (234, 664, and 874 GHz). The benefits of sub-mm combined with previous theoretical investigations and successful field campaigns have led organizations such as the European Organisation for the Exploitation of Meteorological Satellites (EUMETSAT) to explore and plan missions, namely the near future launch of the Meteorological Operational Satellite – Second Generation (MetOp-SG) with the sub-mm Ice Cloud Imager (ICI) (Buehler et al., 2012; Liu et al., 2018; Eriksson et al., 2020c). NASA has pushed the state of the art of spaceborne sub-mm measurements through sensors such as the aforementioned IceCube and follow up mission SWIRP.

2.3. Ice cloud signals in the sub-mm spectral range

Intuitively, to fill the gap between ice cloud particle size sensitivities between infrared (small particles) and passive/active microwave measurements (large particles) requires exploration of observations that are higher frequency (smaller wavelength) than our current passive microwave radiometers. The push to higher frequencies is also motivated by the weak scattering signals at frequencies lower than 94 GHz. As mentioned in the previous section, the benefits of sub-mm wave measurements (from ~300-1000 GHz) to fill the gap in ice cloud sensitivity have been explored, and led to the planning, development, and successful deployment of a spaceborne radiometer (e.g., IceCube). This section highlights the benefits of using measurements in the sub-mm spectral region to characterize ice cloud properties and makes the case for their ability to

complement existing measurements, thus filling this observational gap in cloud ice and providing a more holistic understanding of ice cloud properties.

Before noting the benefits of sub-mm measurements, it is necessary to start with a discussion of the manner in which sub-mm radiation interacts with ice clouds. As mentioned previously, microwaves (passive and active) are capable of penetrating into most clouds and provide some information on the vertical structure within the cloud. At lower passive microwave frequencies (e.g., less than ~65 GHz), the emission from liquid clouds dominates the weak scattering signal, but at higher frequencies the scattering effects by ice clouds become significant. This is because the imaginary part of the refractive index for pristine ice is much smaller than the real part. As a result, ice particles are weak absorbers and subsequently emit little sub-mm radiation, which makes the ambient temperature of ice clouds inconsequential to radiometric measurements. It then follows that sub-mm radiation primarily interacts with ice particles through scattering. Consequently, as upwelling sub-mm radiation (arising from absorption/emission of water vapor below the cloud) reaches and interacts with ice particles in the cloud, some of the radiation is scattered out of the line of sight of a downward viewing spaceborne sensor. This has the effect of reducing the brightness temperature (*TB*) that a spaceborne sensor would measure compared to clear sky.

Figure 2.3 shows how *TB* at several sub-mm frequencies changes as a function of *IWP* (left panel) and D_{eff} (right panel). When looking at the left panel, there is a monotonic decrease in *TB* in the two highest sub-mm channels (640 and 874 GHz) as *IWP* increases, meaning there is sensitivity for inferring *IWP*. However, there is very

little sensitivity for the other sub-mm channels to *IWP*, with 448 GHz showing almost no sensitivity. The IR channel has good sensitivity to *IWP* for values less than ~50 g/m^2. This decline in sensitivity is due to the increase of optical thickness within the cloud. When looking at the right panel, there is significant sensitivity of the two highest frequency sub-mm channels to D_{eff} less than ~110 µm. The increase in *TB* at a particular D_{eff} for these two channels is likely due to increased multiple scattering. Therefore, certain *TBs* correspond to two different D_{eff} values. This can be problematic in terms of retrieval because there are multi-valued solutions to the inverse problems. At 325 GHz, there is good sensitivity to D_{eff} up to ~300 µm. In the IR channel, there is a nice monotonic relationship between *TB* and $D_{eff,}$ but sensitivity is noticeably smaller for smaller sized particles. Note, there is no sensitivity exhibited to either *IWP* or D_{eff} at 448 GHz and *TB* remains close to constant and near the clear-sky *TB*. This hints at the possibility of using 448 GHz to glean information on clear-sky *TB*.

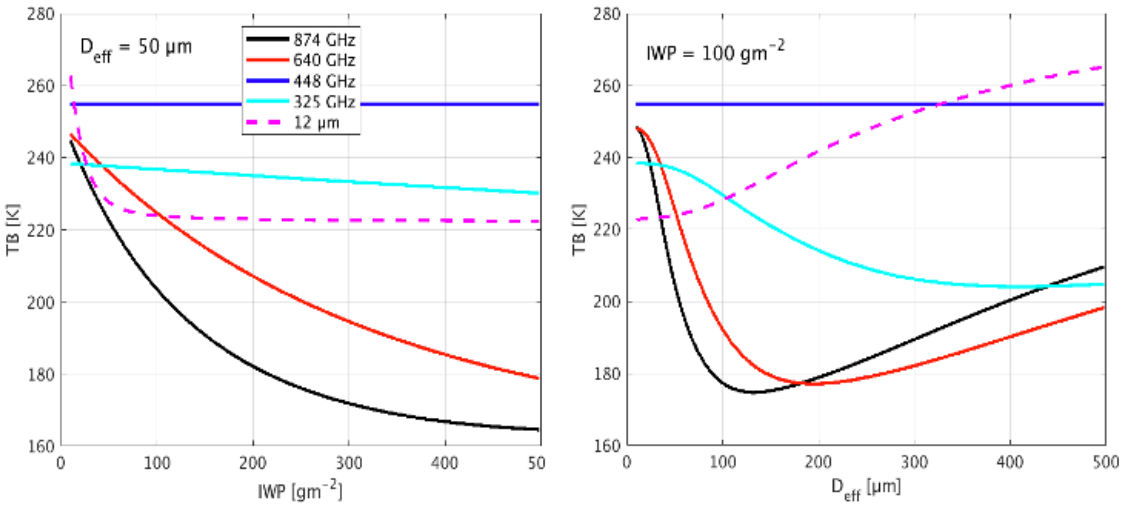

Figure 2.3: Sensitivity of *TB* to *IWP* and D_{eff} for five sub-mm channels and one IR channel. In the left panel D_{eff} is fixed at 50 µm and in the right panel *IWP* is fixed at 100 g/m2.

Considering a blackbody with roughly the same terrestrial temperature as the Earth viewed from space (280 K), the spectral (monochromatic) radiance in $W/m^2/sr/Hz$ emitted at a microwave wavelength of ~1.54 cm (20 GHz) is approximately ten orders of magnitude less (10^{-10}) less than the maximum radiance, which corresponds to a wavelength of 10.3 µm. Therefore, it is not practical to express terrestrial radiation in $Wm^{-2}sr^{-1}Hz^{-1}$ and is why it is typically expressed in *TB*, which is defined as the temperature of an equivalent blackbody that would give the same radiance at the considered wavelength (Rees, 2001, Chapter 2). For the remainder of this thesis, the aforementioned reduction in *TB* from cloud scattering compared to clear sky is referred to as *TB* depression (ΔTB) or cloud induced radiance (T_{cir}), defined as

$$\Delta \boldsymbol{TB}\ (\textbf{or}\ \boldsymbol{T_{cir}}) = \boldsymbol{TB_{Clear\ Sky} - TB_{Cloudy}}. \qquad (\mathbf{2.1})$$

Figure 2.4 provides a simple illustration of the principle of *TB* depression and sub-mm remote sensing for ice clouds.

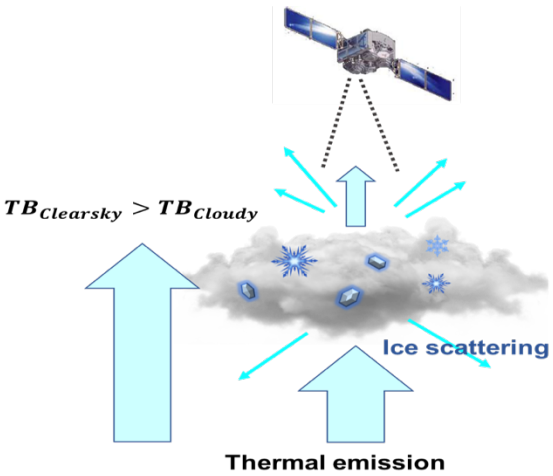

Figure 2.4: Illustration of *TB* depression ($\Delta \boldsymbol{TB}$) of sub-mm radiation due to ice clouds.

Previous studies have demonstrated the usefulness of mm and sub-mm measurements to infer ice cloud properties, such as *IWP* and ice particle effective diameter (D_{eff}) (Evans et al., 1999; Wang et al., 2001). Compared to the visible, infrared (IR), and lower frequency microwave spectral ranges, sub-mm wavelengths exhibit notable advantages. One such advantage is that the wavelengths in this spectral region are comparable to ice particle sizes which account for most of the ice mass in the cloud. As a result, the scattering process is in the Rayleigh and Mie regimes, and the extinction of ice clouds (i.e., radiometric signal) is primarily related to the volume (or mass) of the ice particles and is also sensitive to the ice particle shape and size (Maio et al., 2001). Because the effect of the interaction of ice particles with the upwelling radiation impinging from below the cloud is to scatter radiation partly out of the line of sight of the detector, we see a *TB* decrease (or ΔTB increase) as cloud cover increases. This relationship between *TB* depression (ΔTB) and the mass of cloud ice (or *IWP*) is another significant benefit of using sub-mm radiometry. The difficulty in relating the ΔTB to ice mass primarily arises in the case of high *IWP*, where the signal saturates due to increased multiple scattering. However, the upwelling radiation does not saturate for most ice clouds, meaning that the radiative transfer remains linear (i.e., ΔTB is proportional to *IWP*).

Figure 2.5 shows simulations similar to those in Fig. 2.3, except ΔTB is shown in the y-axis. Similar patterns are evident in these figures, such as the high sensitivity to *IWP* when *IWP* is small (< 50 g/m^2) for the IR channel until the signal is saturated. Again, we see a good relationship between the highest frequency sub-mm channels to

IWP, with some saturation occurring when *IWP* becomes large. In the right panel, there is significant sensitivity to D_{eff} for the highest frequency sub-mm channels, but ΔTB again reaches a maximum and begins to decrease. Note however, that ΔTB at 325 GHz and 12 μm exhibits a mostly monotonic response to D_{eff} and could possibly be used to mitigate the multivalued solution problem in the highest sub-mm frequencies.

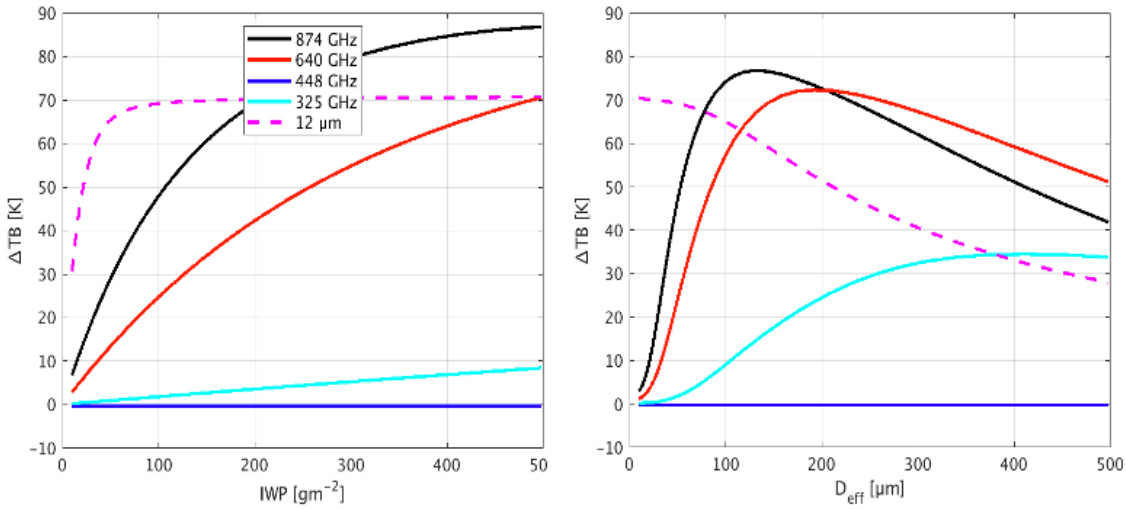

Figure 2.5: Sensitivity of ΔTB to *IWP* and D_{eff} for five sub-mm channels and one IR channel. In the left panel D_{eff} is fixed at 50 μm and in the right panel *IWP* is fixed at 100 g/m2.

Lastly, since there is significant water vapor absorption in this frequency range, the lower atmosphere is opaque in most cases, meaning that emission from the surface and low clouds does not contribute to the upwelling radiation. This simplifies retrievals over surfaces with differing emissivity. It is important to mention however, that while in general we can imagine the interaction of ice clouds with sub-mm radiation as simply a layer of ice resting atop a radiation source, the resultant cloud signal is also a function of cloud height. For example, if the conditions are such that the ice cloud altitude is too

low, then the lower portion of the cloud will be in the vertical region which is influenced by water vapor absorption. This is the so-called water vapor screening effect, and to mitigate this we must employ different channels with different sensing heights, or clear sky weighting functions.

Because of these benefits, sub-mm wave measurements have the capacity to obtain information from upper tropospheric ice cloud layers and improve the retrieval of ice cloud properties. However, even the most ideal measurement systems are incomplete without a retrieval system, which necessitates an accurate forward model (i.e., radiative transfer solver). The accuracy of the forward model, and consequently the retrieval, relies on the quality of necessary assumptions on the microphysical properties of ice particles within the cloud. The radiative properties (e.g., cross-sections and phase matrix) are contingent on the physical properties of the scattering object. It follows that a realistic representation of ice particles within clouds is a significant factor contributing to retrieval accuracy. The remainder of this section provides a brief discussion of some microphysical properties which significantly influence the radiative (e.g., scattering) properties of ice particles, particularly as they relate to the following section on the polarization of sub-mm radiation. While it is also necessary to understand the properties below for liquid hydrometeors, the following sections are solely concerned with frozen hydrometeors in the context of ice cloud remote sensing. A more detailed discussion of the single scattering properties of ice particles is provided in Chapter 3.

2.3.1. Complex permittivity of ice

It is necessary to have knowledge of the dielectric properties of ice in order to successfully model cloud radiative properties. One such property is the complex permittivity, which is a measure of the polarizability of a dielectric object and is equal to the square of the particle refractive index. The complex permittivity of pure ice is one of the foundational components which determine ice scattering properties. However, it depends on many factors and it is therefore challenging to acquire the true value of the permittivity of ice particles. A study by Jiang and Wu (2004) developed an empirical model based on an existing model and parameterizations for the purpose of analyzing Microwave Limb Sounder (MLS) cloud measurements. They demonstrated that for ice particles ranging from ~100-300 μm, a 20% uncertainty in the imaginary part of the permittivity results in up to ~10% errors in extinction coefficient and single scattering albedos, and that only a 5% uncertainty in the real part produces the same magnitude of errors. It is important to note that the error decreases as observing frequency increases, with the highest frequency (640 GHz) having an error of ~1%. A study by Xie et al., (2009) found that absolute variations of brightness temperatures due to uncertainties in ice permittivity were more than 1K, although this work focused on millimeter microwave frequencies (89-183 GHz). As an additional complication, the refractive index of ice is sensitive to temperature in the sub-mm spectral region. Ding et al. (2017) demonstrated the sensitivity of ice particle scattering properties in the sub-mm region to ice refractive index at different temperatures. In Chapter 5 we present an information content-based investigation of the temperature effects on the refractive index, and

subsequent contributions to ice cloud property retrieval biases over sub-mm and infrared wavelengths.

2.3.2. Ice particle size distribution

The particle size distribution (PSD) provides the number of particles per unit volume having a diameter (or radius) D, in the range of $D + dD$ and typically follows some known distribution (e.g., gamma or lognormal). It is necessary to assume some size distribution of ice particles when modeling their radiative properties. Since the scattering capability of an ice particle (or any scattering object) is a function of its size and the considered wavelength, it logically follows that variation in the PSD contributes to the difficulties in understanding the interaction of radiation with clouds and consequently can be a source of significant uncertainties in remote sensing of ice cloud properties (Hogan et al., 2006).

2.3.3. Ice particle shape

The shapes of ice particles can be quite complex and vary significantly within individual clouds and from cloud to cloud. This complexity in shape makes quantifying ice particle scattering and absorption effects from measured radiation non-trivial. It has typically been the convention to assume ice particles as spheres for the purpose of radiative transfer and retrievals (e.g., Evans et al., 2005). This is due to the simplicity of calculating the single scattering properties of spheres compared to irregular particles, since these properties are strongly a function of particle shape. However, over the last couple of decades, improvements in electromagnetic light scattering calculations have allowed for more realistic representations of ice particles, such as plates, hexagonal

columns, and aggregates. The computational burden required to compute the single scattering properties of more complex irregular shapes (and at different wavelengths) is still in most cases quite large even for state-of-the-art supercomputers. Furthermore, computing the scattering properties for irregularly shaped ice particles is not something that can be achieved on the fly. Fortunately, there exist databases of single scattering properties for various irregular shapes which are of substantial benefit to researchers without access to such computing facilities (e.g., Yang et al., 2005; Brath et al., 2020). In Chapter 5 we investigate how assuming a particular ice particle shape model to represent natural ice particles influences particle single scattering properties, and the subsequent impact in remote sensing applications of ice cloud properties.

2.3.4. Ice particle orientation

Computing the scattering properties of cloud ice particles depends on the dielectric properties of the particles, as well as their shape, size distribution, and orientation. Ice particles in clouds are usually irregularly shaped and randomly oriented (Noel et al., 2006), but due to aerodynamic forces preferential orientation is possible (Noel et al., 2005). Preferential orientations can increase the scattering effects of ice particles, and more specifically can enhance polarization signals in passive sub-mm measurements (Xie et al., 2012; Defer et al., 2014). Due to the difficulty of computing single scattering properties of ice particles with a preferred orientation (e.g., horizontal), it is typically the case that particles are assumed to be randomly oriented in remote sensing application. However, since ice particles do in some cases exhibit a preferential orientation, which influences particle scattering (such as generating halos and arcs) and

the polarization of scattered sub-mm radiation, it is important to be cognizant of the implications of particle orientation in remote sensing of ice cloud properties. In Chapter 6 we explore how particle orientation, such as horizontal, impacts simulated polarized *TBs*.

2.4. Microwave observations of polarized radiation

As previously presented, higher microwave frequencies (e.g., sub-mm) exhibit significant scattering signals from frozen hydrometeors compared to their lower frequency counterparts. This often serves to reduce the observed *TB* and can provide information on the properties of ice clouds. How sub-mm radiation interacts with frozen hydrometeors (e.g., ice particles) is complicated because it is a function of cloud properties, such as the mass of ice and the particle size distribution (PSD), as well as properties of the particles, such as their shape, orientation, and dielectric properties. Observations show that irregularly shaped ice particles within clouds can possess a preferred orientation, which is an important consideration for the transfer of radiation in the atmosphere. It is well known that this preferred orientation produces strong dichroism effects, and subsequently induces a polarization difference (*PD*) between horizontal and vertical polarization observations (Evans and Stephens, 1995b; Maio et al., 2003). Particles polarize incoming polarized radiation due to scattering, and since sub-mm radiation interacts with ice particles primarily through scattering, polarization considerations are important. In order to simplify radiative transfer and remote sensing algorithms, ice particles have usually been assumed to be spherical and randomly oriented, and radiation emanating from the cloud was assumed to be unpolarized.

However, *PD* can be combined with *TB* to provide additional information and further constrain retrievals of ice cloud properties. For the purpose of this thesis, we define *PD* as

$$PD = TB_v - TB_h \,, \tag{2.2}$$

where subscripts *v* and *h* correspond to vertical and horizontal polarization states, respectively. A more detailed discussion of polarization signals in the sub-mm spectral region due to ice clouds, as well as the value added by polarized measurements to ice cloud property retrievals is provided in Chapters 6 and 7.

3. SCATTERING AND RADIATIVE TRANSFER THEORY

3.1. Introduction

Electromagnetic radiation is an important process that facilitates energy transfer in the atmosphere, and electromagnetic scattering by particles is important in many atmospheric remote sensing applications (Mishchenko et al., 2002; Liou, 2002). More specifically, electromagnetic radiation refers to oscillating electric and magnetic fields that transport electromagnetic energy as they travel through a medium. The propagation of electromagnetic radiation through a medium, such as the Earth's atmosphere, and the interaction with the matter within is described by the theory of atmospheric radiative transfer. Radiation can be absorbed, scattered or emitted, as it interacts with atmospheric constituents such as gases, aerosols, or hydrometeors. The relative importance of each type of interaction depends on the type of particle (e.g., liquid, ice, dust aerosol, etc.) and the wavelength of interest within the electromagnetic spectrum.

As previously mentioned, ice particles typically interact with sub-mm electromagnetic radiation through scattering. The importance of incorporating polarization into radiative transfer and remote sensing applications in this spectral region is first mentioned in Chapter 2 and emphasized further in Chapters 4, 5, and 6. Therefore, it is important to provide a general overview of electromagnetic light scattering and polarization and describe the single scattering properties necessary for these applications. We can further clarify particle scattering electromagnetically if we consider the particle as a discrete elementary electric charge. If an oscillating

electromagnetic wave impinging on the particle excites the charge such that it oscillates with the same frequency as the incident wave, secondary electromagnetic waves will radiate in all directions. In the case of an absorptive particle, energy will be dissipated from the incident wave into the particle. Scattering and absorption are both mechanisms which reduce the amount of energy from the incoming wave, and the sum of the magnitudes of their respective reductions is referred to as extinction.

The example above of an electromagnetic wave impinging on and exciting a discrete electric charge (particle), or even an aggregate of charges, understates the complexity of electromagnetic scattering. In reality, the secondary waves that are the products of each oscillating charge also interact with and excite other nearby charges. Superimposing the secondary waves in order to quantify the total scattering field now becomes significantly more complicated because we must account for the phase differences of the waves, which are a function of the particle and the configuration of the charges comprising it (Mishchenko et al., 2002). Therefore, it is impractical to compute the scattered field by superimposing all secondary waves produced by these charges. A much more tractable approach is to consider a macroscopic particle that is comprised of elementary charges with some particular density and refractive index. We can then solve the Maxwell equations for this new macroscopic electromagnetic field to calculate the scattered field.

Now we have a formalism in which to compute scattered radiation for a single particle or an ensemble comprised of a limited number of elements. However, in reality it is often the case that radiation is scattered by large groups of particles with significant

spatiotemporal variability, for instance clouds of ice crystals, water droplets, or aerosol particles. As mentioned above, a collection of particles can be treated as a fixed ensemble at a given time. However, since measurement time is finite, we actually measure a statistical average over a substantial number of different ensemble realizations.

Solving the Maxwell equations in this fashion is not computationally feasible, so we must make approximations or assumptions to significantly simplify the problem. Let us assume that particles within the cloud are sufficiently distant from one another such that their scattering is independent of one another, e.g., each particle scatters as if the others did not exist. We could then approximate the scattered field as the sum of the fields generated by individual particles. This is the so-called *single scattering approximation*. If the assumption holds that each particle is randomly positioned, sufficiently distant from all other particles (i.e., in the far field zone) and that we can ignore phase interferences (i.e., incoherent scattering), then the scattering (and absorption) properties of a small volume element of particles can be computed by summing the respective properties from all particles within that volume.

The single scattering approximation is not valid when the medium contains a large number of particles. In this case we must consider the interaction of each particle with the incident radiation as well as radiation scattered by other particles, i.e., each particle scatters radiation which has already been scattered by another particle. This is referred to as multiple scattering and the approach here is to solve the radiative transfer equation. It is important to note that this approach still assumes scattering particles are

randomly positioned and are sufficiently separated such that extinction (scattering plus absorption) within a volume element can be calculated by incoherently adding the respective properties of all particles within this volume.

This chapter provides the theoretical background and definitions involving scattering and polarization and forms a basis for the introduction of the radiative transfer equation discussed in section 3.5, which is necessary to understand simulations and models presented in subsequent chapters. Regarding some concepts in this chapter, such as methods to compute the single scattering properties, detailed derivations are beyond the scope and framework of this thesis, and in these cases qualitative explanations are provided. The scattering theory presented here is primarily referenced from Mishchenko et al. (2002), Liou and Yang (2016), and detailed derivations related to concepts in this chapter can be found in these references.

3.2. Scattering theory

Light is made up of electromagnetic waves which propagate at the speed of light c, as governed by the fundamental Maxwell's equations. Electromagnetic radiation can be described by properties such as phase δ, intensity I and polarization, and is characterized by electric and magnetic vectors **E** and **H**, respectively. If the vibration of the electric vector **E** is focused on a particular plane along the propagation direction, it can be said that the light is polarized in that direction. By leveraging the above properties, we can gain information through remote sensing. Note that the particular quantity to be exploited is a function of the measurement technique and spectral region.

Let's consider monochromatic (single wavelength) electromagnetic waves that propagate in the *z* direction, and express them in terms of the complex valued electric field components

$$\mathbf{E}_v = \mathrm{e}_v E_{v0} \mathrm{e}^{-i(\omega t - kz - \delta_v)} \tag{3.1}$$

$$\mathbf{E}_h = \mathrm{e}_h E_{h0} \mathrm{e}^{-i(\omega t - kz - \delta_h)} \tag{3.2}$$

where k is the wavenumber, t is the time, ω is the angular frequency, $\mathrm{e}_{v,h}$ are the amplitudes, and $\delta_{v,h}$ denote the phases. If the wave encounters a particle along its propagation path, there are two physical mechanisms which can remove energy from the incident wave, absorption and scattering. This removal, or attenuation, of energy from the incident wave is referred to as extinction and is defined as the sum of the energy attenuated due to both scattering and absorption. If the wave is propagating through a non-absorbing medium, scattering will be the sole mechanism of extinction. A discussion of absorption is presented in later sections.

How radiation incident on a scattering object is scattered depends on the wavelength/frequency as well as inherent properties of the scattering object, such as the size, shape, orientation, and refractive index. Here we introduce an important parameter called the *size parameter* that describes the relationship between the size of the scattering object and the wavelength of the incident radiation, defined as

$$x = \frac{2\pi r}{\lambda} \tag{3.3}$$

where r is the radius of the scattering object and λ is the wavelength. As mentioned above, scattering processes lead to extinction of energy contained in the incident wave.

Furthermore, all scattering processes induce polarization of incoming light. Light is considered polarized in a certain direction when the vibration of the electric vector, **E** in Eqns. 3.1 and 3.2, is concentrated in that direction along the propagation direction. Thus, we can define the polarization direction as the direction of the electric vector. For example, the *v* and *h* subscripts in these equations denote vertical and horizontal polarization, respectively. More specifically, the electric field vector is decomposed into two components, $\mathbf{E}_v$ and $\mathbf{E}_h$, which are orthogonal to each other (i.e., parallel and perpendicular) in relation to an arbitrary reference plane through the direction of propagation *z*. In addition to the direction of vibration of the electric vector, we need to consider the phase difference between the two components of this vector to further describe the polarization of light as possibly circular or elliptical polarization. The phase difference between the two waves and the relative magnitudes of E_{v0} and E_{h0} (the vertical and horizontal electric field components at time 0) in the above equations determines the polarization. More simply, we can now quantitatively say that the polarization is defined by the orientation of the electric field and the extent to which it varies with time.

In addition to polarization, to gain a more holistic understanding of scattering processes we need to define two more terms, permittivity and permeability. Together, they are complex values which characterize the response in a medium to external electric and magnetic fields, respectively. In order to relate these properties to the complex valued electric field components (shown in the equations above), it is necessary to provide a few other relations. The angular frequency ω is related to the cyclical

frequency ν as $\nu = 2\pi\omega$ and the wavenumber k is related to the wavelength λ as $k = 2\pi/\lambda$. Additionally, it holds that the wavenumber $k = \frac{\omega n}{c} = \frac{\omega}{c}\sqrt{\epsilon_r \mu_r}$, where the refractive index $n = \sqrt{\epsilon_r \mu_r}$, the relative permittivity is ϵ_r, and the relative permeability of the medium is μ_r. As mentioned above, the permeability and permittivity can take on complex values, and consequently the refractive index and wavenumber can also be complex-valued, i.e., $n = n_r + in_i$ and $k = k_r + ik_i = (n_r + in_i)\frac{\omega}{c}$. From this, we can write Eqns. 3.1 and 3.2 as follows:

$$\mathbf{E}_v = \mathrm{e}_v E_{v0} \mathrm{e}^{-k_i z} \mathrm{e}^{-i(\omega t - k_r z - \delta_v)} \tag{3.4}$$

$$\mathbf{E}_h = \mathrm{e}_h E_{h0} \mathrm{e}^{-k_i z} \mathrm{e}^{-i(\omega t - k_r z - \delta_h)} \, . \tag{3.5}$$

It is evident from these equations that the wave now propagates at a different speed. Furthermore, there is now an attenuating exponential which is dependent on the magnitude of the imaginary refractive index n_i. This equation highlights the impact of refractive index on scattering calculations for both ice and liquid hydrometeors, which are needed in remote sensing applications. It is important to note that the refractive index (for liquid water and ice) varies significantly with frequency. Furthermore, in the microwave spectral region, as is used in this work, there is a considerable dependence of the refractive index on temperature (Ding et al., 2017). This dependence, and the subsequent impact on radiative transfer calculations and retrievals, is discussed in more detail in Chapter 5.

3.3. Definition of polarization and the Stokes Vector

In the previous section we defined polarization in terms of the relative magnitudes of the amplitudes and phase differences of the electric field. However,

typical instruments used in remote sensing are not capable of measuring electric or magnetic fields. Therefore, to understand polarization through measurements, we have to define it in terms of something instruments can measure, i.e., intensity. For this, we define the Stokes vector:

$$\mathbf{I} = \begin{bmatrix} I \\ Q \\ U \\ V \end{bmatrix} = \frac{1}{2}\sqrt{\frac{\epsilon_0}{\mu_0}} \begin{bmatrix} E_{0v}E_{0v}^* + E_{0h}E_{0h}^* \\ E_{0v}E_{0v}^* - E_{0h}E_{0h}^* \\ -E_{0v}E_{0h}^* - E_{0h}E_{0v}^* \\ i(E_{0h}E_{0v}^* - E_{0v}E_{0h}^*) \end{bmatrix} \tag{3.6}$$

where asterisks signify complex conjugation. It is then possible to express the Stokes vector as total intensity of an electromagnetic wave, and in terms of the vertical and horizontal polarizations:

$$I = I_v + I_h \tag{3.7}$$

$$Q = I_v - I_h. \tag{3.8}$$

Since we only consider linear polarization in this work, the U and V components are omitted. We now have measurable quantities relating to the polarization of electromagnetic radiation.

3.4. Ice particle single scattering properties

This section provides a very brief overview of the single scattering properties which are necessary to quantify scattering, extinction, and absorption by ice particles. A thorough discussion of the various methods available to calculate the single scattering properties of ice particles is beyond the scope of this thesis, but a brief description of the methods applicable in the sub-mm spectral region is provided in Chapter 5.

3.4.1. Phase matrix

The transformation of the Stokes vector of an incident wave to that for a scattered wave is described by the phase matrix. Every element of the 4 x 4 phase matrix is real-valued, has units of area, and depends on the scattering angle (θ from 0 to 2π relative to 0° = the propagation direction z) and azimuth angle (ϕ from 0 to π relative to the defined direction of vector x = 0°). For the purpose of light scattering and radiative transfer, if no assumptions are made concerning the position (i.e., orientation) or shape of the particle, the scattering phase matrix is typically denoted **P** with the following format:

$$\mathbf{P} = \begin{bmatrix} P_{11} & P_{12} & P_{13} & P_{14} \\ P_{21} & P_{22} & P_{23} & P_{24} \\ P_{31} & P_{32} & P_{33} & P_{34} \\ P_{41} & P_{42} & P_{43} & P_{44} \end{bmatrix}. \tag{3.9}$$

The first element (i.e., phase function P_{11}, or the magnitude or intensity of the ray) is usually normalized to unity over the scattering angle sphere (area 4π) as:

$$\int_0^{2\pi} d\phi \int_0^{\pi} \frac{P_{11}(\theta)}{4\pi} \sin(\theta)\, d\theta = 1. \tag{3.10}$$

It is convenient here to define the asymmetry factor, g, as the first moment of the phase function:

$$g = \frac{1}{2}\int_{-1}^{1} P\,(cos\theta) \cos\theta dcos\theta \tag{3.11}$$

When particles are considered randomly oriented and have a plane of symmetry, we can apply the law of reciprocity (van de Hulst, 1957). As a result, we have the following relationships between the phase matrix elements: $P_{12} = P_{21}$, $P_{13} = -P_{31}$, $P_{14} = P_{41}$, $P_{23} = -$

P_{32}, $P_{24} = P_{42}$, $P_{34} = -P_{43}$. Furthermore, we derive the following relationships: $P_{13} = P_{14} = P_{23} = P_{24} = 0$, and $P_{31} = P_{32} = P_{41} = P_{42} = 0$ (Liou, 2002). Consequently, there is symmetry in the phase matrix such that only six elements are nonzero and different, P_{11}, P_{12}, P_{22}, P_{33}, P_{34}, and P_{44}. Therefore, non-spherical particles which are randomly oriented and obey the law of reciprocity possess the following phase matrix

$$\mathbf{P} = \begin{bmatrix} P_{11} & P_{12} & 0 & 0 \\ P_{12} & P_{22} & 0 & 0 \\ 0 & 0 & P_{33} & P_{34} \\ 0 & 0 & -P_{34} & P_{44} \end{bmatrix}. \tag{3.12}$$

However, when considering a particle with a preferential azimuthal orientation and there is no plane of symmetry, the law of reciprocity cannot be applied, and the full phase matrix is required.

3.4.2. Extinction matrix

First, we define the extinction coefficient, β_e, as the product of the mass extinction cross section and the density of the particle. The extinction coefficient can essentially be thought of as optical depth (τ), since the two are related by the following:

$$\tau = \int_x^\infty \beta_e \, dz. \tag{3.13}$$

Since extinction is simply the sum of scattering and absorption, it logically follows that β_e is the sum of the absorption and scattering cross sections. It is convenient here to define the single-scattering albedo, $\widetilde{\omega}$, as the ratio of the scattering and extinction coefficients, i.e.,

$$\widetilde{\omega} = \frac{\beta_s}{\beta_e}. \tag{3.14}$$

When considering horizontally oriented particles, the extinction coefficient is governed by the energy characteristics of the incident beam and its state of polarization, or dichroism of the scattering media (Liou, 2002). As a result of dichroism, the extinction coefficients corresponding to the Stokes vector are represented by the 4 x 4 extinction matrix (Liou, 2002). In the special case of the exact forward direction (scattering direction 0°), attenuation of incident radiation is expressed by the extinction matrix, **K**. When particles are assumed to be randomly oriented with at least one plane of symmetry, the extinction matrix is independent of direction and polarization, and is subsequently diagonal. However, when assuming a horizontal particle orientation the extinction matrix has only three independent elements and may be written according to Mishchenko (1991) as

$$\mathbf{K} = \begin{bmatrix} \beta_{\mathrm{e}} & \beta_{pol} & 0 & 0 \\ \beta_{pol} & \beta_{e} & 0 & 0 \\ 0 & 0 & \beta_{e} & \beta_{cpol} \\ 0 & 0 & \beta_{cpol} & \beta_{e} \end{bmatrix}, \tag{3.15}$$

where β_{pol} and β_{cpol} are the polarized and cross-polarized components of the extinction coefficients with respect to the incident Stokes vector. Here we also define extinction efficiency, Q_{ext}, as the ratio of the extinction cross section to the average projected area of the particle.

3.4.3. Absorption vector

If the temperature of a particle is above absolute zero, it will emit radiation. When assuming local thermodynamic equilibrium (LTE), the emissivity of a medium is equal to its absorption. The energetic and polarization characteristics of such emitted

radiation is described by a four component Stokes emission column vector. For the Stokes emission vector, also called the particle absorption vector, we can derive the absorption vector as a function of the Planck blackbody radiation (ARTS Theory Guide; Eriksson et al., 2020b). To calculate this value, which is required by ARTS, we need Q_{ext}, $(1-\tilde{\omega})$, as well as particle area, volume, density, and intended *IWP*.

3.5. Vector radiative transfer equation

Under the assumptions of fully elastic scattering and local thermodynamic equilibrium, the radiative transfer equation including polarization and multiple scattering is:

$$\frac{\mathrm{d}\mathbf{I}(\nu,\mathbf{r},\hat{\mathbf{n}})}{\mathrm{d}s} = -\mathbf{K}(\nu,\mathbf{r},\hat{\mathbf{n}})\mathbf{I}(\nu,\mathbf{r},\hat{\mathbf{n}}) + \mathbf{a}(\nu,\mathbf{r},\hat{\mathbf{n}})B_{\nu,p}(\nu,\mathbf{r}) + \int_0^{4\pi}\mathbf{Z}(\nu,\mathbf{r},\hat{\mathbf{n}},\hat{\mathbf{n}}')\mathbf{I}(\nu,\mathbf{r},\hat{\mathbf{n}}')\mathrm{d}\hat{\mathbf{n}}', \quad (3.16)$$

where s is the distance along the propagation direction $\hat{\mathbf{n}}$, ν is the frequency, $\mathbf{r}$ is the position in the atmosphere (relative to the origin of the coordinate system, generally within the scattering particle), $\mathbf{Z}$ is the phase matrix, $\mathbf{a}$ is the absorption vector, $\mathbf{K}$ is the extinction matrix, $B_{\nu,p}$ is the Planck function of the incident radiation (generally sunlight) at atmospheric pressure p, and $\mathbf{I}$ is the specific intensity vector. The specific intensity vector is a superposition of the Stokes parameters and fully describes the incident radiation, e.g., $\mathbf{I} = (\mathrm{I}, \mathrm{Q}, \mathrm{U}, \mathrm{V})^{\mathrm{T}}$. It is also important to note that $\mathbf{K}$, $\mathbf{a}$, and $\mathbf{Z}$ are bulk or ensemble averaged quantities. Equation 3.16 describes radiation along a particular line of sight and is modulated by the three terms on the right-hand side of the equation. The first term is a sink (i.e., the negative sign) and represents attenuation due

to extinction. The sources of this attenuation are absorption and scattering out of the line of sight. The remaining terms are both source terms, with the second one being a blackbody emission source. The third term (second source term) describes radiation which is scattered from any direction into the line of sight. It is the primary task of radiative transfer models to solve Eq. 3.16. There are many methods to solve this equation, and the iterative scattering solver available in ARTS that was used for the work presented is described in Chapter 4.

4. METHODS

4.1. Atmospheric Radiative Transfer Simulator (ARTS)

A large amount of research has been devoted to developing dedicated forward models (radiative transfer simulators) to simulate satellite radiances for different sensors operating in different spectral regions. Radiative transfer models can be described as either physical (e.g., line-by-line) or fast models (e.g., Radiative Transfer for TIROS Operational Vertical Sounder; RRTOV). Physical models are more computationally expensive, although parameterizations can be used to improve speed, but the accuracy then depends on the parameterizations. Since this work involves conducting many numerical experiments of a hypothetical sub-mm spaceborne radiometer, this study uses a physical model, specifically the Atmospheric Radiative Transfer Simulator (ARTS). This section provides a general description of ARTS and highlights certain aspects which are relevant to the rest of this work but is by no means a comprehensive description of ARTS. More details regarding the capabilities of ARTS is presented in Buehler et al. (2018). For further information on the usage and underlying theory behind ARTS, the reader is directed to the ARTS User Guide (Eriksson et al., 2020a) and ARTS Theory Guide (Eriksson et al., 2020b), which are included in the ARTS distribution. ARTS is open-source and can be freely downloaded from https://www.radiativetransfer.org/getarts/.

ARTS is a publicly available vector radiative transfer model initially developed to deal with passive millimeter (mm) and sub-millimeter (sub-mm) measurements but

has since been extended to cover the complete thermal infrared (IR) spectral range (Buehler et al., 2018). Since ice clouds primarily scatter sub-mm radiation, it is essential to use a model such as ARTS which solves the radiative transfer equation (RTE) considering multiple scattering. To achieve the most realistic simulation, a radiative transfer model should consider the effects of preferentially oriented non-spherical particles, which both serve to polarize upwelling radiation. The treatment of polarization, which is implemented in ARTS, requires that the radiative transfer equation be solved in full Stokes Vector form and not simply for scalar intensity.

4.2. Forward model and ARTS setup

Brightness temperatures of upwelling radiation from ice clouds and for a clear sky are simulated using ARTS version 2.2. Auxiliary data describing the atmospheric profile and cloud characteristics (e.g., ice particle scattering properties) are input into ARTS to simulate all four components of the Stokes Vector with respect to the two vertically integrated cloud parameters of interest, ice water path (*IWP*) and ice particle effective diameter (D_{eff}). The following sections provide a brief overview of important components of ARTS and how they relate to the forward model employed in this work. Finally, since ARTS is a physical model and therefore slower than other models, we present some optimizations to improve computation speed.

4.2.1. Description of the atmosphere

ARTS can model the atmosphere with differing dimensionality ranging from 1D to 3D. In the 1D case, the atmosphere is considered to be spherically symmetric, meaning that there is no latitudinal or longitudinal variation in atmospheric properties

(e.g., temperature, water vapor) and these quantities only vary with the vertical pressure coordinate. Furthermore, due to the spherical geometry of the 1D case, radiation varies only with vertical viewing direction (i.e., viewing zenith angle) and has no azimuthal dependence. It is important to note that 1D in this case is simply a naming convention chosen for simplicity and convention by the ARTS developers and does not represent a true one-dimensional atmosphere. Clouds or clear sky in the 1D case imply a completely cloud covered or cloud-free Earth, but this simply means that a satellite pixel views a small enough area that when radiation is scattered to another vertical grid column, the cloud (or cloud-free) characteristics are the same at the same level. While this is obviously unrealistic, it differs little from cloud with a significant horizontal extent (and model grid cells or satellite pixels are assumed small enough that sub grid-scale clouds average out on a large scale), so there is merit in using a 1D setup to explore the upper limit of how ice clouds scatter and polarize upwelling sub-mm radiation. The 1D case is used exclusively for the remainder of work presented. A schematic of a 1D atmosphere inside ARTS is shown in Fig. 4.1.

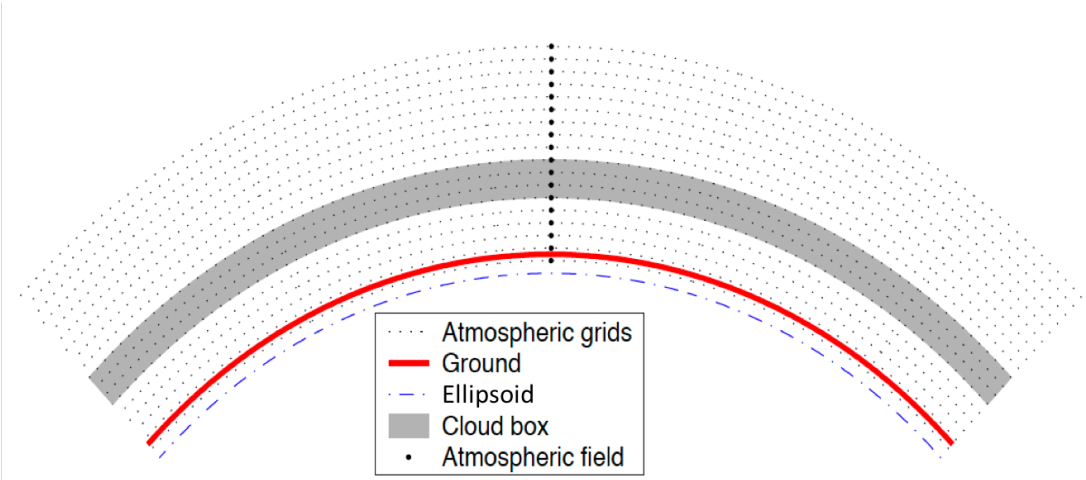

Figure 4.1: Schematic of a 1D atmosphere in ARTS. Due to the spherically symmetric nature of the atmosphere, the radius of the ellipsoid, surface, and all pressure levels are constant everywhere. Fields are specified by a value at each pressure level. The cloud box can extend either from the surface to a specified pressure level, or between two pressure levels (as shown above). The surface must be above the lowermost pressure level, as indicated in this figure. Reprinted from ARTS User Guide, 2020.

The gray area in Fig. 4.1 denotes the "Cloud box" which contains the simulated cloud and other scattering objects. In order to reduce computational time, scattering calculations are limited to the cloud box which is defined vertically by two pressure surfaces. The top boundary condition to compute the scattering within the cloud is the incoming clear sky radiation. Therefore, it is important to ensure that when determining the lower and upper cloud box boundaries, no radiation emanating from the cloud be allowed to reenter the cloud box in another location. An example of this would be a case in which there is an optically thin layer between the cloud and the ground, and ground reflection is significant. To be precisely correct, the cloud box should extend to the ground. However, since scattering calculations are only conducted within the cloud box, this significantly increases computation time. For the purpose of this work the ground is treated as a blackbody (not reflecting radiation), and due to significant water vapor

absorption in the sub-mm range, the atmosphere between the cloud and ground is optically thick. Consequently, radiation emerging from and reentering the cloud box is not a concern in this work. This is beneficial in that the cloud box can be moved away from the surface and be much smaller, which reduces computation time for scattering calculations.

4.2.2. Sensor characteristics

The handling of observation geometry in ARTS is very flexible and can be used to effectively simulate different observation geometries and sensor characteristics. ARTS requires that both the viewing directions and observed location be specified. The observation location is expressed by latitude, longitude, and the geometric altitude. Viewing directions are defined by the azimuthal and zenith angles. For the purpose of a 1D atmosphere, there is no horizontal variation in atmosphere/cloud properties so latitude and longitude can be arbitrary, and radiation is only a function of zenith angle, so azimuth angle is unimportant. In this study we simulate *TB*s corresponding to a typical conical scanning radiometer with a viewing zenith angle of 53.5˚.

ARTS has the ability to perform monochromatic pencil beam simulations but can also be provided a sensor response function to convolve a spectrum. Since there are currently no operational down-looking spaceborne instruments operating at the sub-mm frequencies considered in this work, the sensor response function is assumed to be a Gaussian centered at the desired frequency with some assumed half width at half maximum. Further details of the specific frequencies and wavelengths utilized in this work are provided in Section 4.3.

4.2.3. Surface properties

The radiative background is the radiative intensity at a starting point of the propagation path that is in the direction of the line of sight. Four possible radiative backgrounds exist in ARTS, including space, the surface, the surface of the cloud box, and the interior of the cloud box. The radiative background of the surface is the sum of surface emission and radiation reflected by the surface. When considering microwave frequencies less than 200 GHz, the surface has a significant impact on the upwelling *TB*. However, frequencies greater than 200 GHz have an absorption spectrum which is dominated by water vapor lines and continuum absorption. Therefore, the surface contribution to upwelling radiation for these frequencies is negligible, except in very dry conditions. While emissivity can simply be user specified in ARTS, it does include the FAST microwave Emissivity Model version 6 (FASTEM) (Kazumori and English, 2015), which calculates emissivity based on incidence angle, frequency, and surface wind/temperature. Although ice cloud remote sensing in the sub-mm spectral region is advantageous because low clouds and the surface do not contribute to the upwelling radiation, for simplification and consistency a constant surface emissivity of 0.6 is prescribed, which corresponds to ocean surfaces.

4.2.4. Gas absorption

Absorption coefficients are obtained in ARTS through a combination of line-by-line calculations as well as continua and complete absorption models (e.g., Rosenkranz, 1993; Rosenkranz, 1998). Line-by-line calculations are more accurate, but since the gas absorption must be computed at each point along the propagation path, it is much more

computationally expensive. The general idea is that the complete models are meant to be used alone, and the pure continua are meant to be used in conjunction with explicit ARTS line-by-line calculations. To reduce computation time for comparable simulations (same absorbing species and volume mixing ratios), ARTS allows for the preparation of a gas absorption lookup table. It is also possible to calculate the absorption matrix on-the-fly within radiative transfer calculations. As previously mentioned, ice particles primarily scatter sub-mm radiation and absorption is negligible. Therefore, only gaseous absorption is included in this work for the purpose of simulating clear sky and cirrus induced brightness temperatures (*TB*s).

Gaseous absorbers considered for all sub-mm frequencies in this study are N_2, O_2, and H_2O. Water vapor has a strong electric dipole moment and subsequently has a significant number of rotational transitions in this spectral region. Absorption due to water vapor is computed with the complete absorption model by Rosenkranz (1998), which is specially designed to quickly calculate absorption in frequencies from 1-1000 GHz. The total water vapor absorption computed by the model is described by the sum of line and continua absorptions. A complete absorption model is also used to calculate the absorption due to diatomic oxygen (O_2) (Rosenkranz, 1993). In the case of molecular nitrogen, it contains no magnetic or electric dipole moment and shows no rotational spectral signal for the microwave frequencies considered in this work. Regardless, nitrogen can absorb radiation in this spectral region through collision induced absorption (CIA). However, this effect is particularly small compared to absorption due to water vapor, so we do not consider CIA for the purpose of this work and simply employ the

continua model outlined in Rosenkranz (1993). Further details of the continua and complete models, such as line catalogs and line shape functions are beyond the scope of this document. For more information, the reader is directed to ARTS Theory and sources within.

Characterizing gaseous absorption for IR wavelengths requires a substantial increase in the number of monochromatic pencil beam calculations compared to the microwave spectral region. To accurately determine IR gaseous absorption and subsequently radiances, it is necessary to have profiles of atmospheric gases. To reduce computation time of IR radiances, we employ a gas absorption lookup table, which includes absorption due to H_2O, O_3, N_2O, O_2, HNO_3, ClO, and N_2. There are additional methods to reduce the time to simulate IR radiances, as described in section 4.2.6.

4.2.5. Scattering radiative transfer solver

Scattering of sub-mm radiation by molecules and aerosols can be neglected, but ice clouds primarily scatter in the mm and sub-mm spectral region. This requires the radiative transfer equation (RTE) to be solved with the consideration of multiple scattering, which ARTS handles in a rigorous manner. ARTS is capable of fully polarized radiative transfer calculations, where the polarization state is expressed in terms of the Stokes formalism. There are two scattering solvers provided in ARTS, a Monte Carlo (MC) and a Discrete Ordinate Iterative (DOIT) solver. In simple terms, the DOIT method solves the radiative transfer equation at a number of discrete zenith angles, with accuracy dependent on the grid discretization. Although DOIT is implemented in ARTS for 1D and 3D atmospheres, it is recommended for use only with

1D atmospheres. Therefore, since this study only considers a 1D atmosphere the DOIT scattering solver is used exclusively. A brief description of the DOIT scattering solver is provided here. Further details concerning DOIT can be found in Chapter 9 of the ARTS Theory Guide (Eriksson et al., 2020b) and Emde et al. (2004).

A schematic of the DOIT method is shown in Fig. 4.2, adapted from ARTS Theory. It is important to note that the first guess field (typically clear-sky radiance) can be chosen arbitrarily, so by choosing a first guess that is close to the solution the number of required iterations can be reduced. A convergence test is performed after each iteration and if the difference in the absolute value of all Stokes vector elements for the new and old radiation fields is smaller than some user defined limit, then the final solution is reached. Therefore, due to the computational burden of iterative methods, defining the appropriate convergence criteria is a balance between accuracy and computation time. The user can also define differing convergence limits for different Stokes Vector components. In this work we adopt a convergence limit of 0.01 K (in Rayleigh Jeans brightness temperature) for the first component of the Stokes Vector and 0.001 K for all other components.

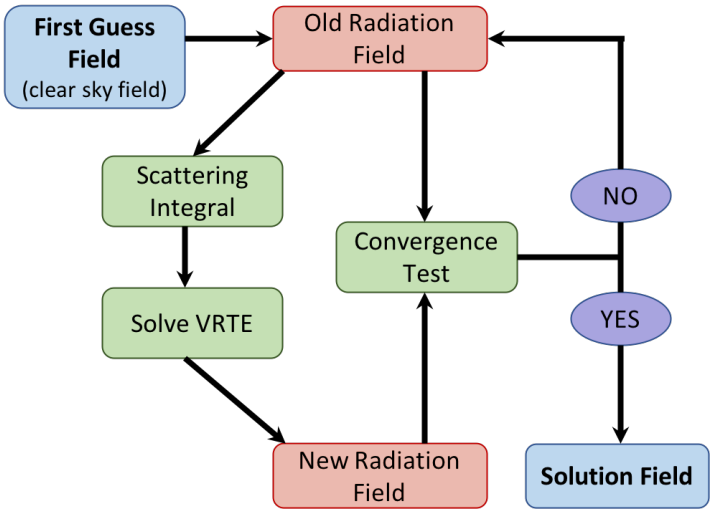

Figure 4.2: A schematic of the iterative method in the ARTS DOIT scattering solver. Adapted from ARTS Theory Guide, 2020.

The DOIT method leverages the single scattering approximation, meaning that the optical depth for one propagation path is assumed to be much less than 1 and subsequently multiple scattering can be ignored along this path step. Users are able to define propagation path step lengths, and therefore can select a coarse grid inside the cloud box. However, it is important to note that it is incumbent on the user to ensure the optical depth, due to scattering along propagation paths, is sufficiently small such that the single scattering approximation is valid. The optical depth along a propagation path is a function of the single scattering properties of the scattering/absorbing media, with the maximum optical depth (τ) due to particles defined as

$$\tau_{max} = \langle \boldsymbol{K} \rangle \cdot \Delta s \,, \tag{4.1}$$

where $\langle \boldsymbol{K} \rangle$ is the ensemble averaged extinction matrix and Δs is the length of the propagation path step. It is assumed that $\tau_{max} \ll 0.05$ for all the radiative transfer simulations used in this work. Ensuring the optical depth due to particles along the

propagation path is sufficiently small (i.e., particle number density is small) allows application of the single scattering approximation.

When using iterative methods to solve the vector radiative transfer equation, it is important to consider the vertical resolution (number of grid points) within the cloud box since that is what determines the number of iterations. For example, suppose we assume N pressure levels inside the cloud box. Since the radiation field is updated at each grid point with consideration only paid to the adjacent grid cells, at least N-1 iterations are necessary to propagate scattering effects from lowest levels in the cloud to the top of the cloud. Therefore, previous iterative methods suffer when a fine grid resolution is required within the cloud to resolve cloud inhomogeneities. As a solution, ARTS employs a "sequential update of the radiation field" which divides updates to the radiation field into three parts (e.g., down-looking, up-looking, and limb). By using this method, the number of iterations no longer depends on how many pressure levels are prescribed for the cloud and is now only a function of the cloud optical thickness or number of multiple scattering events. Further details concerning the sequential update technique are beyond the scope of this thesis and are provided in ARTS Theory. Even though this method improves speed when considering high resolution in clouds, numerical experiments conducted to determine an optimal vertical cloud resolution show that a minimum of ten pressure levels within the cloud is necessary for TB to converge.

4.2.6. Speed improvements

The success of operational retrievals relies on a fast forward model which can simulate real world measurements. Although it is not a goal of this work to provide an

operational ice cloud retrieval algorithm, increased forward model speed significantly reduces the computational time to conduct numerical experiments (e.g., sensitivity analyses) which are important for algorithm development. The following sections highlight some factors which influence forward model computation time, as well as techniques that are used to reduce this time.

4.2.6.1. Zenith angle considerations

As noted above, DOIT relies on discretization of the scattering field zenith angles. The zenith angle is simply the angle between the zenith direction and the desired line of sight. It is evident from this statement that the zenith angle thus depends on how the zenith (or nadir) is defined. In ARTS, zenith directions are defined to be along the line which passes the center of the coordinate system and the point of concern. Fig. 4.3 provides a schematic definition of zenith and azimuth angles for a particular line of sight. From the figure it is evident that zenith angle has a valid range of 0-180° depending on if the instrument is down or up-looking. For a nadir (down-looking) instrument $\theta = 180°$. As mentioned previously, for this work we consider the viewing zenith angle (VZA) of a typical spaceborne scanning radiometer to be $\theta = 53.5°$. In ARTS, this VZA corresponds to an upward-looking instrument and therefore we must adjust the VZA within ARTS to ensure we are modeling the proper viewing geometry.

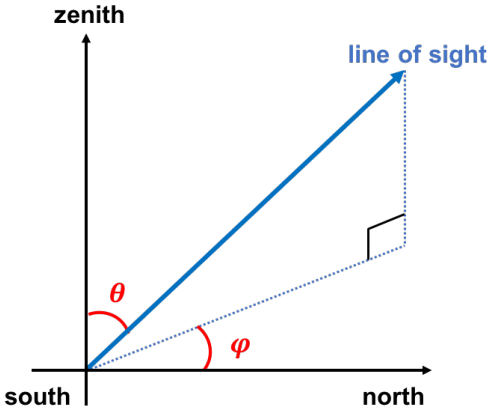

Figure 4.3:A schematic depiction of zenith ($\boldsymbol{\theta}$) and azimuth ($\boldsymbol{\varphi}$) angles. Adapted from ARTS User Guide, 2020.

The accuracy of the DOIT method is largely a function of the discretization of the zenith angle. This can be explained by considering the intensity as a function of zenith angle. It makes sense that the intensity at $\theta = 0°$ (upward-looking) approaches zero while $\theta = 180°$ (downward-looking) provides maximum intensity, and that a significant increase of intensity occurs at roughly $\theta = 90°$. This is because thermal emission from the ground and lower atmosphere is considerably larger than that from trace gases in upper atmosphere. Since the Stokes Vector at the intersection point of two propagation paths is obtained by interpolation, there can be significant interpolation errors if the discretization of the zenith angle grid is too coarse. One solution would be to utilize very fine resolution equidistantly spaced zenith angle grids, but this substantially increases computation time. Consequently, a method is required to optimize the zenith angle grid. To mitigate this, the scattering integral is computed on a coarser zenith angle grid, since the accuracy does not suffer, and the zenith angle grid is optimized to provide the radiation field to a certain accuracy.

Another concern regarding the zenith angle grid arises when attempting to simulate infrared radiances. For the infrared wavelengths used in this work, the scattering phase function has a pronounced forward peak, while in the microwave spectral region the phase function is much smoother. Therefore, since the DOIT method discretizes the phase function, an extremely fine angular grid may be needed to fully characterize strongly nonlinear phase functions, as is the case with the forward peak in infrared simulations. This is also the case any time the phase function has significant oscillations. There are existing techniques to deal with this issue, however none are currently implemented in ARTS. Therefore, we treat this problem by truncating the scattering phase matrix and provide it and other necessary scattering properties to ARTS. The truncation technique used is the δ-fit method, which fits the phase function with a limited number of Legendre polynomials in order to accurately simulate radiance. Specific details of the δ-fit method are beyond the scope of this thesis but are provided in Hioki et al. (2016).

4.2.6.2. Bulk optical properties

The length of time needed to simulate cloudy *TB*s in ARTS can be significant, depending on the atmosphere/cloud conditions and the frequency of interest. A substantial amount of that time is dedicated to preparing the bulk scattering properties for ARTS (e.g., extinction/phase matrix and absorption vector). Preparing these properties involves integrating values from a database over a particle size distribution (PSD). The PSD utilized in this work is a gamma distribution defined as:

$$n(D) = N_0 D^{\mu} e^{-\lambda D} \tag{4.2}$$

where D is the size or maximum dimension of the particle, N_0 is the intercept parameter, λ is the slope parameter, and μ is the shape parameter. A gamma distribution with effective variance of 0.1 is used as the PSD exclusively in this work unless otherwise noted. From the PSD, we know the number of particles present as a function of particle size. This is then used to compute the ice particle effective diameter (D_{eff}). D_{eff} is essentially a ratio of the volume of the PSD to its projected area, or more technically the ratio of the 3rd and 2nd moments of the size distribution. For nonspherical particles D_{eff} is calculated as follows:

$$Deff = \frac{3}{2}\frac{\int_{D_{min}}^{D_{max}} V(D)n(D)\mathrm{d}D}{\int_{D_{min}}^{D_{max}} A(D)n(D)\mathrm{d}D}, \tag{4.3}$$

where D_{max} and D_{min} are the maximum and minimum sizes of the particles, and n is the number of ice particles as determined by the PSD (Yang et al., 2005).

Since there is no function built into ARTS to compute the single scattering properties of ice particles, they must be supplied as input. While there are methods in ARTS to calculate particle size distributions, single scattering properties files are very large even for an individual frequency. Therefore, to save computational resources, bulk optical property calculations are conducted external to ARTS and include the following steps:

1. Extract values of maximum dimension, total volume and projected area, extinction efficiency, single scattering albedo, asymmetry parameter, and scattering phase matrix elements for a specific wavelength from the optical property database (e.g., Yang et al., 2005).

2. Calculate the desired effective diameter using the equation above.
3. Combine the desired ice water path (*IWP*) with the prescribed cloud geometric thickness to determine the number of particles in each layer within the cloud according to the following equations:

$$IWC = \int_{D_{min}}^{D_{max}} \rho_{ice} V(D) n(D) \mathrm{d}D \tag{4.4}$$

$$IWP = \int_{z_{bot}}^{z_{top}} IWC \ \mathrm{d}z \tag{4.5}$$

where *IWC* is the ice water content, *n* is the again the number density, ρ_{ice} is the density of ice, and *V* is the volume in the first equation and z_{top} is the cloud top height and z_{bot} is the cloud base height in the second equation.

Preparing the bulk optical properties in this fashion saves computational time and makes it easier to prescribe a particular D_{eff} and *IWP* within the cloud, which are the two main parameters of interest.

4.2.6.3. Lookup table generation

Forward model simulations necessary for retrievals can be acquired in two ways. First, an online model can be used in which the radiative transfer simulator is run at each retrieval iteration. This requires a very fast radiative transfer simulator. There is also the option of an offline model in which many radiative transfer simulations are conducted and put into a lookup table (LUT) for retrieval purposes. A LUT essentially stores the dependent variables (e.g., *TB*) as a function of the independent variables (e.g., D_{eff} and *IWP*). The benefit of the online model is the ability to compare measurements to model output at any point in the parameter space without sacrificing accuracy due to

interpolation. However, when using an offline model and LUT, the speed is significantly increased but the resolution of the LUT becomes an important consideration. The desired resolution is a function of the nonlinearity between the dependent and independent variables, retrieval type, and memory constraints. Intuitively, if the LUT has a coarse grid, the accuracy of *TB* attained from interpolation between two *IWP* values depends more heavily on how linear the response of *TB* is to *IWP* between IWP_1 and IWP_2. The effect of nonlinearity when interpolating decreases as resolution increases, and if the *TB* is computed for infinitesimal increments of *IWP*, then there would be no error due to interpolation. However, this is obviously not feasible and there has to be some practical trade-off between the range and resolution of the LUT.

Using ARTS, we can simulate *TB* at two orthogonal polarizations for sub-mm frequencies in ~30-40 seconds, including the time needed to prepare the bulk scattering properties. Computation time significantly increases for infrared simulations, taking ~120-130 seconds. This increase is mainly due to the increased gas absorption computation. This length of times obviously precludes ARTS from being an online model. Consequently, it was necessary to modify the forward model to develop LUTs that can be used for retrievals. A sizeable amount of effort was placed on developing a forward model which strikes a balance between efficiency and accuracy. A modified Akima interpolation scheme is selected, which is piecewise cubic Hermite interpolation. The Akima algorithm also produces piecewise polynomials with continuous first order derivatives, and is used to compute the Jacobians (or weighting function), which is a

matrix of the partial derivative of the forward model output with respect to the state vector element as,

$$\mathbf{K}_{ij} = \partial F_i(\mathbf{x})/\partial x_{j.} \tag{4.6}$$

Note, it is common to represent the Jacobian and the extinction matrix (i.e., Eq. 3.15) with **K**. For the remainder of this document, **K** represents the Jacobian, and the extinction matrix is denoted as *K*.

The details of the original Akima formulation can be found in Akima (1970). This algorithm was selected because it produces fewer undulations compared to spline interpolations, is well equipped to deal with rapid changes between flat regions, and because it is a local cubic interpolant, it generalizes to 2-D and higher dimensional n-D grids. In the original Akima algorithm, the slope is computed on the desired interval and the derivative at a sample point is simply the equally weighted average of nearby slopes. In the modified algorithm, more weight is given to the side with a lower slope, subsequently helping to reduce overshoot. Equations for the original weights for an interval from x_i to x_{i+1} are

$$w_1 = |S_{i+1} - S_i| \tag{4.7}$$

$$w_2 = |S_{i-1} - S_{i-2}|, \tag{4.8}$$

where S_i is the slope in the interval. The new weights used are as follows:

$$w_1 = |S_{i+1} - S_i| + \frac{|S_{i+1} + S_i|}{2} \tag{4.9}$$

$$w_2 = |S_{i-1} - S_{i-2}| + \frac{|S_{i-1} + S_{i-2}|}{2} \tag{4.10}$$

Through careful selection of the parameter space discretization and interpolation method, the time needed to simulate *TB* for changes in D_{eff} and *IWP* is significantly reduced. The *TB* simulation time with ARTS is reduced from ~30 s to ~0.2 s for sub-mm and from ~120 s to ~0.1 s for infrared. It is also essential that the accuracy does not suffer. To verify the accuracy, we compute *TB* at discrete values of *IWP* and D_{eff} directly in ARTS and compare these values to those obtained through interpolation of the much coarser resolution LUT. Figures 4.4, 4.5, and 4.6 show the differences in *TB* computed with ARTS versus *TB* computed with the interpolated forward model for 640 GHz, 874 GHz, and 12μm, respectively. First, note that *TB* is accurate to within 0.5 K over the entire parameter space for both sub-mm and infrared bands. The accuracy of sub-mm *TBs* in Figs. 4.4 and 4.5 is well within the uncertainties of measured *TB* from the Compact Scanning Submillimeter-wave Imaging Radiometer (CoSSIR; Evans et al., 2005) flown during the Tropical Composition, Cloud and Climate Coupling (TC4) experiment (Toon et al., 2010). Uncertainties obtained from calibration target fluctuation statistics for retrievals on 19 July 2007 were 2.38 and 4.03 K at 640 and 874 GHz, respectively (Evans et al., 2012).

It is also evident when comparing the accuracy of sub-mm *TB* (Figs. 4.4 and 4.5) to infrared *TB* (Fig. 4.6) computed from the LUTs, that infrared *TB* is overall more accurate than its sub-mm counterpart. This is because the response of sub-mm *TB* to changes in *IWP* and D_{eff} is significantly more nonlinear than in the infrared, which is demonstrated in Fig. 2.3. Considered individually, these figures also provide insight into the areas of the parameter space where a nonlinear response of *TB* to *IWP* and D_{eff}

occurs, and consequently retrievals may have larger uncertainties. Nonlinearity, particularly in the context of the combination of multiple measurements is further discussed in section 4.6. Generally speaking, the parameters of interest in a retrieval are determined as the ones that most closely simulate the observations. Therefore, it is essential to understand the forward model error and represent it appropriately in the retrieval scheme. It is important to note that we compute *TB* accuracy shown in these figures assuming a single layer ice cloud from 9 to 11 km, a typical tropical atmosphere, and a roughened hexagonal column aggregate particle shape. Similar analyses are conducted for varying cloud top heights (6-15 km), atmospheric profiles, particle shapes (e.g., plate, single hexagonal column), and frequencies (e.g., 243, 325, and 448 GHz). For brevity, those results are not included here, but in all cases *TB* accuracy remains within the uncertainties provided in Evans et al., 2013.

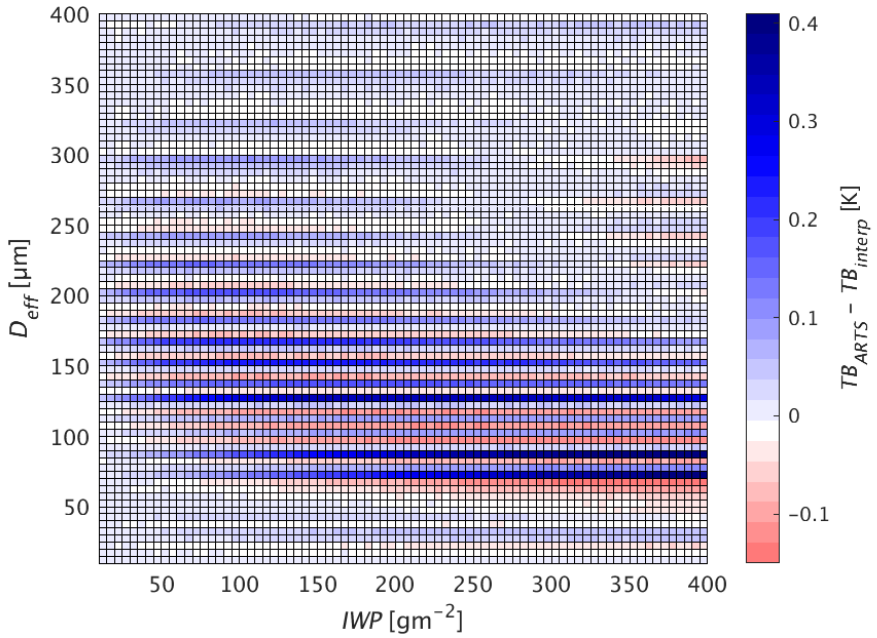

Figure 4.4: Forward model *TB* accuracy as a function of *IWP* and D_{eff} at 640 GHz.

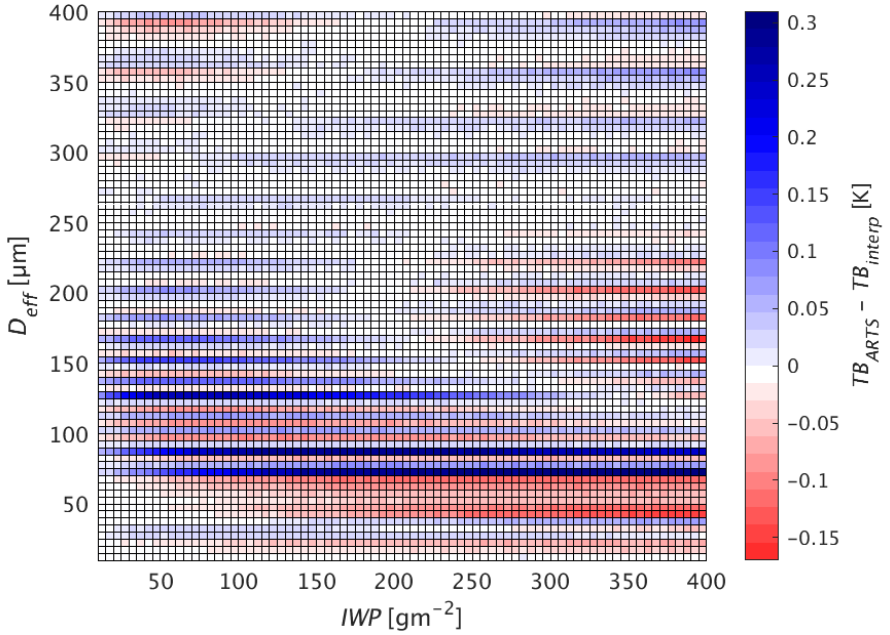

Figure 4.5: Forward model *TB* accuracy as a function of *IWP* and D_{eff} at 874 GHz.

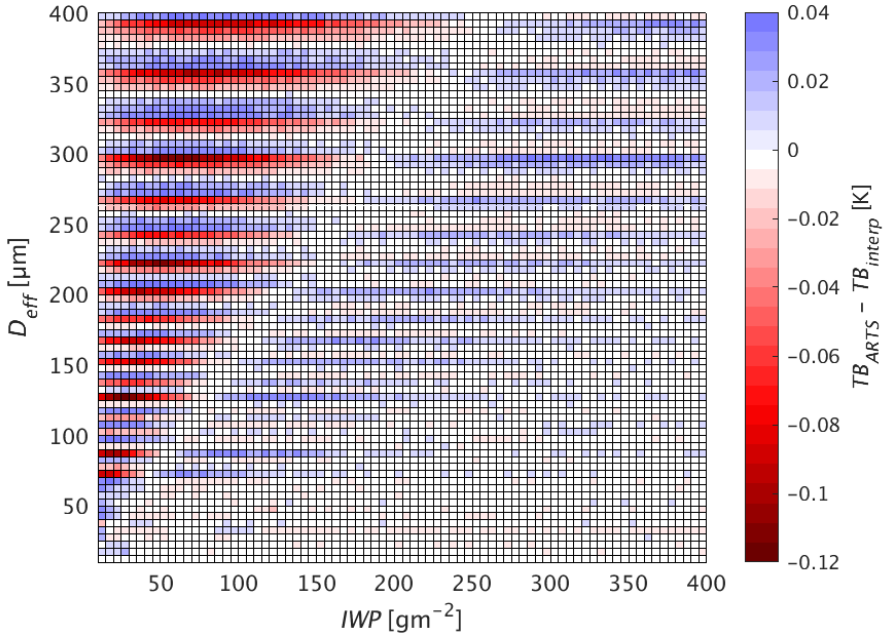

Figure 4.6: Forward model *TB* accuracy as a function of *IWP* and D_{eff} at 12 µm.

As mentioned in Chapter 2, *TB* depression (ΔTB) or cloud induced radiance, is the difference between observed cloudy radiance and that for the same atmosphere without clouds and is nicely correlated to ice mass in the sub-mm spectral region. Consequently, it is not sufficient to understand the *TB* error for only cloudy observations. Therefore, we compute the clear sky *TB* at sub-mm frequencies for a typical tropical atmosphere and compare that to *TB* computed after applying random Gaussian noise to the same atmospheric profile. The forward model *TB* error for the purpose of subsequent retrievals is then represented as

$$\delta TB = \sqrt{\delta TB_{clear}^2 + \delta TB_{cloudy}^2}\,, \tag{4.11}$$

where δTB_{cloudy} is $TB_{ARTS} - TB_{interp}$ (as shown in Figs. 4.4 – 4.6) averaged over the entire parameter space and δTB_{clear} as described above. For example, assuming a cloudy and clear sky *TB* errors of 0.5 and 0.25 K, respectively, ΔTB has an error of 0.56 K.

4.3. Channel selection

Sub-millimeter wave remote sensing of ice clouds has been widely investigated in recent years to retrieve ice cloud mass and particle size, although most work to this point has been theoretical. Determining the optimal number and frequencies of channels to provide measurements for retrievals is not straightforward, and various methods are available for this determination. Here we employ a simple novel approach to quantify the sensitivity, and therefore the applicability of a wide range of frequencies to simultaneously retrieve *IWP* and D_{eff}. We compute LUTs of *TB* as a function of *IWP* and

D_{eff} for a selection of frequencies near water vapor lines and oxygen lines, and in atmospheric windows, shown in Table 4.1. If an offset frequency is listed, the radiance is measured at two frequencies, the center frequency plus and minus the offset (such as 182.3 and 184.3 GHz in the first channel), because the atmosphere is more transparent at those frequencies than at the center frequency, so the radiance is obtained from a lower atmospheric layer.

Table 4.1: *Channels considered in the channel selection process. Units are GHz unless denoted otherwise (* indicates channel wavelength in the specified number of μm).Wavelengths are also provided in parentheses (in μm) for the microwave channels.*

Center frequency [GHz](μm)	Offset frequencies [GHz]	Absorber
183.3 (~1635.5 μm)	1, 3, 7	Water vapor
220 (~1362.7 μm)	2.5	Water vapor
325 (~922.4 μm)	1.5, 3.5, 9.5	Water vapor
380.2 (~788.5 μm)	0.8, 1.8, 3.3, 6.2	Water vapor
448 (~669.2 μm)	1.4, 3, 7.2	Water vapor
487.2 (~615.3 μm)	0.8, 1.2, 3.3	Oxygen
640 (~468.4 μm)	-	Window
874 (~343.0 μm)	-	Window
11*	-	Infrared window
12*	-	Infrared window

Orthogonality between two LUTs of differing wavelengths or frequencies is a measurement of sensitivity, or more precisely, the ability to infer (or retrieve) the two parameters separately from measurements at these wavelengths. In other terms, if LUTs are orthogonal in a particular region of the parameter space, the two measurements contain sufficient information content such that these parameters are entirely separable. However, in reality, LUTs are rarely orthogonal or even consistent throughout the parameter space. We provide some examples below further explaining sensitivity.

Figure 4.7 is a hypothetical LUT showing the *TB*s as a function of *IWP* and D_{eff} computed in two arbitrary channels (while unlabeled here, the red and black lines correspond to roughly evenly spaced values of *IWP* and D_{eff} in the realistic natural range). From this figure the idea of sensitivity becomes clearer. In the upper right corner of the figure corresponding to high *TB*s at both bands, the isolines for *IWP* and *Deff* show moderate separation for IWP (in black), but for D_{eff} it is not possible to differentiate one isoline from another. Therefore, in this part of the parameter space, we can say that there is little information content in these two measurements to retrieve particle size, but there is significantly more information about *IWP*. This is a situation in which the inverse problem is simultaneously over and under-constrained, meaning the number of unknowns (2; *IWP*, D_{eff}) is equal to the number of measurements (2; $TB_{\text{Bands1,2}}$), but the number of independent pieces of information is less than the number of unknowns. Consequently, we can say these measurements have little sensitivity to D_{eff} in this portion of the parameter space.

A different problem can arise and is illustrated by the bottom left part of Fig. 4.7 corresponding to low *TB*'s for both bands. If you think of the LUT as being a plane in *IWP*, D_{eff}, and *TB* space, you can see that it is "folded" in on itself when *TB*s for both bands are small. This becomes a problem of uniqueness (i.e., multi-valued solutions) and implies there exists distinct states which map onto the same location in measurement space. In this situation, we cannot distinguish either state using the measurements, and therefore they possess no sensitivity to *IWP* and D_{eff} in this portion of the parameter space. Conversely, when looking at the center of the LUT (e.g., TB_{Band1} = 220K and

TB_{Band2} = 245K) it is evident the isolines of D_{eff} and *IWP* become more orthogonal. This is indicative of higher information content, higher sensitivity, and subsequently, the ability to simultaneously infer *IWP* and D_{eff} from these measurements within a reasonable range of uncertainty. Note that this example is incomplete because it does not account for many factors such as random *TB* errors, nonuniform ice particle sizes in the satellite pixel, a partly cloudy pixel, or contaminants such as cloud water droplets or aerosols.

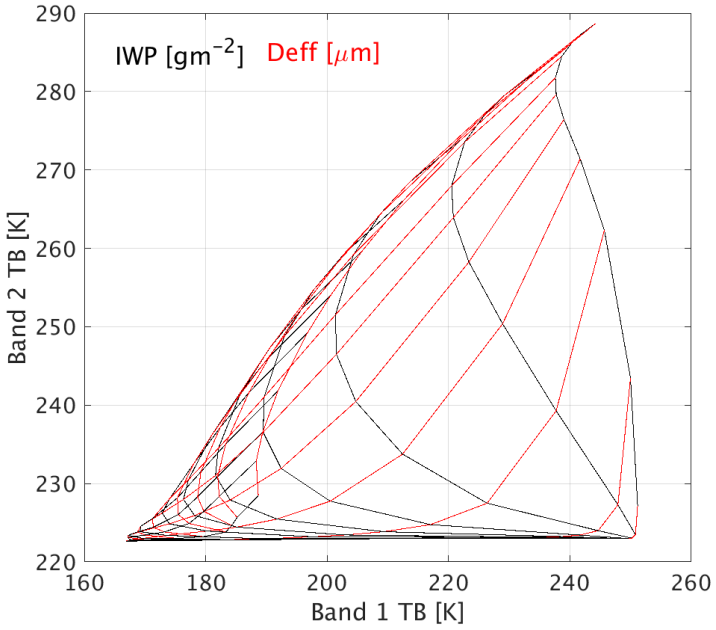

Figure 4.7: Illustrative example lookup table (LUT) for two arbitrary bands. The *TB* calculated at the different bands as provided as a function of *IWP* (black lines) and D_{eff} (red lines).

In order to determine the optimal combination of frequencies to employ in the retrieval, we must first quantify the orthogonality of all combinations of LUTs computed from the candidate frequencies in Table 4.1. To quantify orthogonality, we compute the

determinant of the Jacobian over the entire state space, denoted S (hereafter also referred to as sensitivity):

$$S(LUT_1, LUT_2, IWP, Deff) = \begin{vmatrix} \frac{\partial TB_1}{\partial IWP} & \frac{\partial TB_1}{\partial Deff} \\ \frac{\partial TB_2}{\partial IWP} & \frac{\partial TB_2}{\partial Deff} \end{vmatrix}, \quad (4.12)$$

where TB_1 and TB_2 are the brightness temperatures simulated at two different frequencies. For this analysis, *TB*s are the average of their vertical and horizontally polarized components. We discuss the implications of polarization in subsequent sections. If two LUTs are orthogonal, the determinant will be -1 or +1. Therefore, if the magnitude of the absolute value of the determinant approaches 1, it is indicative of higher orthogonality or sensitivity and denotes a high potential of the two bands to retrieve *IWP* and D_{eff} simultaneously. Because we must compute sensitivity for every unique combination of bands and state-space pairs, the results are multidimensional and difficult to succinctly plot. Therefore, to demonstrate the performance of these bands for typical cloud conditions, the sensitivity is averaged over all discrete parameter space pairs when *IWP* and D_{eff} range from 10-200 g/m^2 and 10-100 μm, respectively. Figure 4.8 shows the results of these calculations. There are two important takeaways from this figure:

1) In general, there is merit in combining infrared and sub-mm measurements to retrieve *IWP* and D_{eff} simultaneously.
2) The sub-mm channels, which demonstrate the highest sensitivities when paired with infrared bands, are 640 and 874 GHz.

Since this study is of a demonstrative nature, the rest of the presented work focuses on sub-mm frequencies of 640 and 874 GHz, and infrared wavelengths of 11 and 12 μm.

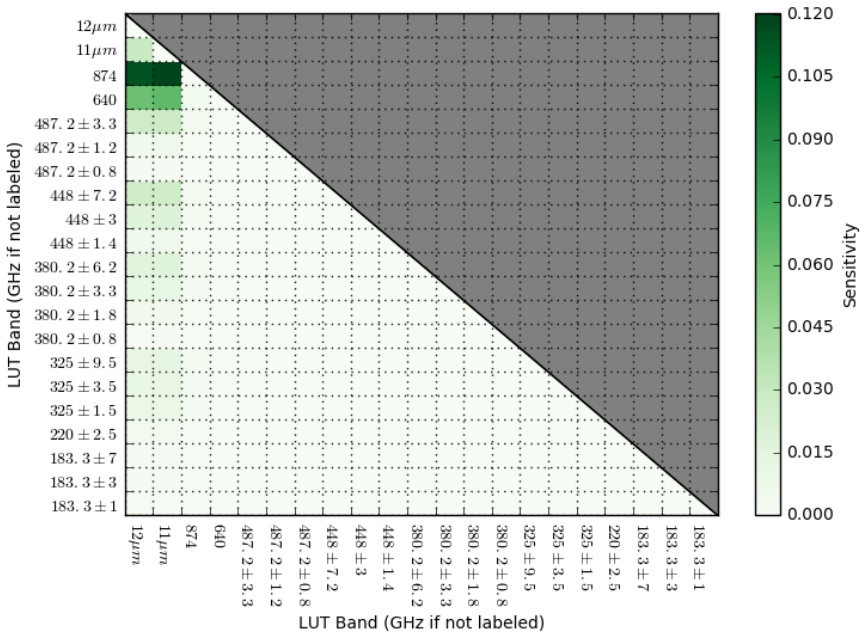

Figure 4.8: Average sensitivity for all unique pairs of channels in the selection study. This figure includes all synthetic pixels with *IWP* (D_{eff}) less than 200 g/m^2 (100 μm).

4.4. Polarization difference analysis

Particles can polarize incoming unpolarized radiation through scattering, and since microwave radiation interacts with ice particles primarily through scattering, polarization considerations here are important. One technical distinction is that polarized radiative transfer calculations require more than simply the phase function and absorption, scattering and extinction coefficients. When solving the vector radiative transfer equation, we need the entire phase and extinction matrix, as well as the absorption coefficient vector. This increases the computational burden of preparing the

scattering properties for ARTS. However, a benefit of ARTS is that the scattering solver (DOIT) generates the entire radiation field, which can be valuable in gaining a physical understanding of the polarization effects within the cloud. Previous studies such as Xie and Maio (2011) show that the polarization difference (*PD*) is proportional to the mass of ice in the cloud, but they only considered frequencies up to 340 GHz. One objective of this thesis is to extend the investigation of the effects of different cloud parameters on polarization signals to higher sub-mm frequencies (640 and 874 GHz) where we expect higher sensitivity to smaller ice particle scattering.

To facilitate this investigation, we compute the *PD*, defined as the difference of brightness temperatures at two orthogonal (vertical and horizontal) polarization states ($TB_v - TB_h$). *PD* can provide information on microphysical properties such as particle shape, size, and orientation. Based on the results of the channel selection study, we initially explore *PD* for the two sub-mm window frequencies stated above, since scattering signatures are more evident, as well as two IR channels (11, 12 μm). The results are shown in Fig. 4.9, assuming a single layer ice cloud from 9 to 11 km containing ice particles which are aggregates of severely roughened hexagonal columns that are randomly oriented and follow a gamma PSD.

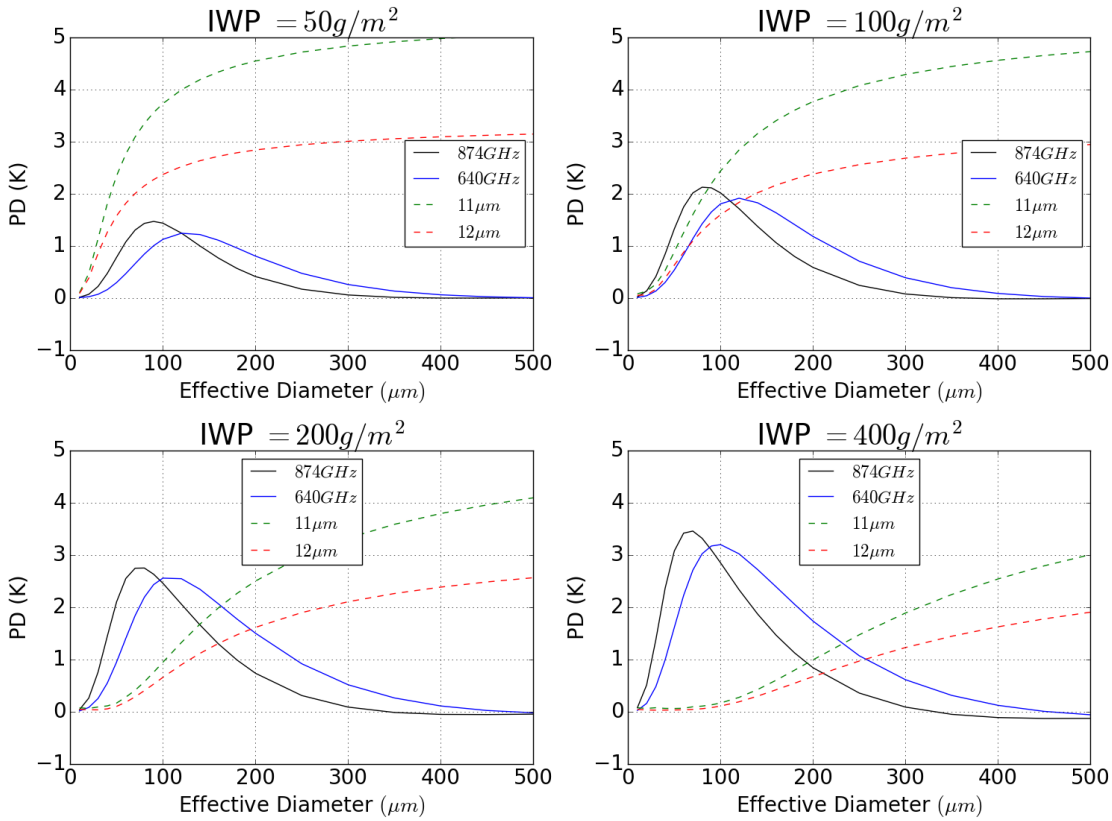

Figure 4.9: *PD* sensitivity to *IWP* and D_{eff} at two sub-mm and two IR channels. Each figure represents a different *IWP* (50, 100, 200, and 400 g/m^2). The solid lines denote the two sub-mm channels (640, 874 GHz) and the dashed lines represent two infrared channels (11, 12 μm).

In all panels of Fig. 4.9, *PD* is positive for sub-mm frequencies and increases monotonically at a particular D_{eff} as *IWP* increases (i.e., from top left panel to bottom right). When considering a single *IWP*, *PD* increases with D_{eff} until reaching a peak at some critical D_{eff}, and then declines toward zero as *Deff* continues to increase. The occurs because as particles become larger multiple scattering begins to dominate, and there is less vertically polarized radiation scattered into the line of sight. Also, note that this critical D_{eff} is different for the two sub-mm frequencies and is smaller for the larger frequency. Since the opacity is greater at higher frequencies which are more sensitive to smaller particles, *PD* begins to decrease at smaller particle sizes for larger frequencies.

When particles are randomly oriented, polarization signals are due to radiation which is scattered into the line of sight because it is the only phase matrix that has nonzero off-diagonal elements. Positive *PD* values occur when radiation scattered out of the direction of propagation is horizontally polarized, leaving vertically polarized radiation in the propagation direction. Horizontally polarized radiation is scattered into the direction of propagation. Consequently, if less radiation is scattered into than out of the line of sight, then the *PD* will be positive.

Again, note that regardless of *IWP*, sub-mm *PD* increases to a maximum at some critical particle size, and then decreases toward zero as D_{eff} continues to increase. This decrease is likely due to the increased multiple scattering. Therefore, we can say that *PD* is mainly sensitive to ice particles in a certain range of sizes, and this range is a function of the frequency and cloud conditions. Although the magnitude varies based on cloud conditions, the D_{eff} peak remains consistent and indicates that sub-mm *PD* is more sensitive to smaller ice particles and IR is more sensitive to larger particles. Also note that *PD* for IR channels saturates for a constant D_{eff} as *IWP*. In other words, assuming a D_{eff} of 200 μm in all four panels, *PD* decreases as *IWP* increases. This saturation effect, or decrease in *PD* as *IWP* increases, is due to the increase in optical thickness. However, sub-mm *PD* does not saturate or diminish as *IWP* increases (at a constant D_{eff}). Accordingly, the lack of saturation in sub-mm bands as *IWP* increases demonstrates the potential for retrieving particle diameter in optically thick clouds.

When *IWP* and D_{eff} are small, IR is more sensitive to smaller particles, but the sub-mm *PD* signal is likely not detectable for these small particles. However, as

expected for small *IWP*, cloud scattering from sub-mm channels is less than scattering from IR channels, and therefore the relative magnitude of *PD* from microwave channels should be smaller. Conversely, when *IWP* is large, the relative magnitude for IR becomes smaller than sub-mm, for small particles. These differing areas of sensitivity provide evidence that a combination of *PD* measurements in these wavelength regimes is potentially beneficial in determining of ice particle diameter for a wide range of cloud optical thickness values. This conclusion, however, is limited to clouds assuming randomly oriented hexagonal column aggregate shapes. The influence of particle shape on *PD* and *TB* is provided in Chapter 5 and impacts due to particle orientation are presented in Chapter 6.

4.5. Synthetic data generation

Due to the current lack of availability of spaceborne sub-mm measurements, it is necessary to generate synthetic data that is physically representative of typical atmospheric and cloud properties in order to conduct the numerical experiments essential in retrieval algorithm development. To accomplish this, we leverage one year of data (2008) from various CloudSat (Stephens et al., 2008) products. CloudSat is one part of a constellation of satellites referred to as the A-Train (e.g., CloudSat, CALIPSO, PARASOL, Aqua, Aura, GCOM-W1) flying in the same sun-synchronous orbit roughly 705 km above the Earth's surface. Aboard CloudSat is the Cloud Profiling Radar (CPR) operating at a nominal frequency of 94 GHz, providing a vertical resolution of 500 m, and cross and along-track resolutions of 1.4 km and 1.8 km, respectively.

The first step in data generation involves filtering. Since this work focuses on tropical ice clouds, we remove all pixels outside $\pm 20°$ latitude. We then extract data from these three CloudSat products: 2B-CLDCLASS-LIDAR, 2C-ICE, and ECMWF-AUX. The variables utilized are provided in Table 4.2. Additional filtering is conducted to ensure that the cloud phase is solely ice and we eliminate clouds which have multiple layers, so that concerns of vertical inhomogeneity do not significantly impact our simulations. These cloud and profile parameters are provided to ARTS to simulate *TB* and *PD*, at a viewing angle of $53.5°$. There are known limitations and uncertainties in these CloudSat products. Consequently, measurements synthesized from these values would likely not be in complete agreement with anticipated future satellite sub-mm measurements. However, we feel that generating data in this fashion still carries a sufficient physical representation of atmospheric and cloud conditions. This is ultimately useful for conducting numerical experiments needed to develop a retrieval algorithm to infer properties of tropical ice clouds from sub-mm and IR measurements, in advance of building and launching a satellite instrument sensing at these frequencies.

Table 4.2: *CloudSat products and variables used to generate synthetic measurements*

Product	**Variables**	**Notes**
2B-CLDCLASS-LIDAR	Cloud Phase	Ice phase only
	Cloud Layer	Single layer only
	Cloud Layer Base	
	Cloud Layer Top	
2C-ICE	Retrieved *IWP*	Ensure $IWP > 0$ g/m^2
	Retrieved Effective Radius	Ensure $D_{eff} > 10$ g/m^2
ECMWF-AUX	Pressure	
	Temperature	
	Specific Humidity	

4.6. Retrieval overview

Optimal estimation is a form of nonlinear regression intended to solve the inverse problem but can be thought of more broadly as a balance between what measurements can inform us about the state and our previous knowledge of the state. This method is selected due to its straightforward treatment of experimental errors (Sourdeval et al., 2013). We also include the information content as an additional metric of quantifying retrieval quality. It is important to consider information content in addition to overall retrieval accuracy, because there may be a set of measurements that carry substantial information only in highly under-constrained problems. This can lead to significant uncertainties in retrieval products due to the ill-posed nature of the problem. Taken together, retrieval accuracy and information content effectively provide a quantitative description of the retrieval process from observations to final products and also present a mechanism for critical objective assessments of different algorithms.

A general overview of the retrieval method is provided in Fig. 4.10. The first stage involves combining the single scattering properties (e.g., phase/extinction matrices and absorption vectors) of a specified ice particle habit (shape) with atmospheric (e.g., temperature, pressure, and volume mixing ratios of all relevant absorbing species) and cloud (e.g., cloud top height and geometric thickness) properties to produce the LUTs. In the second stage, *TB* and *PD* are computed from the LUT corresponding to an initial guess of *IWP* and D_{eff}. Further details of the retrieval method and information content is provided in the following sections.

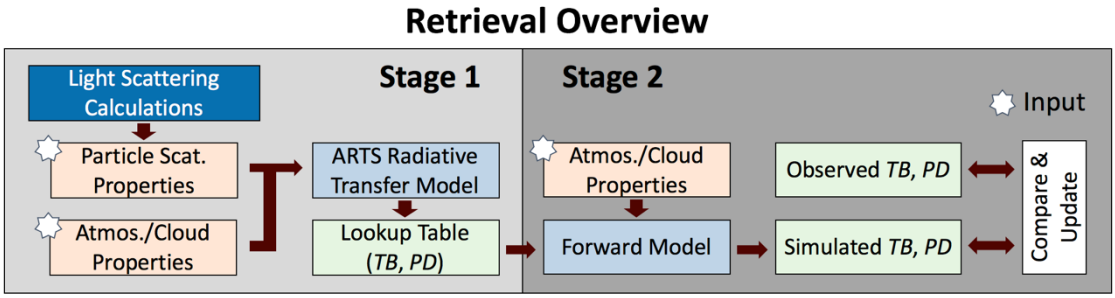

Figure 4.10: An overview of the retrieval framework. All starred boxes are inputs into the retrieval.

4.6.1. Optimal estimation framework

The optimal estimation method is used to solve an inverse problem and in essence, fits forward model output to measurements under the constraints of some *a priori* probability distribution of the state vector (Rodgers, 2000). The problem to be solved is described as

$$\mathbf{y} = \mathrm{F}(\mathbf{x}, \mathbf{b}) + \boldsymbol{\epsilon} \tag{4.13}$$

$$\mathbf{x} = \begin{bmatrix} IWP \\ D_{eff} \\ \dots \end{bmatrix} \tag{4.14}$$

$$\mathbf{y} = \begin{bmatrix} \Delta TB_{640GHz} \\ \Delta TB_{874GHz} \\ TB_{12\mu m} \\ \dots \end{bmatrix}, \tag{4.15}$$

where **x** is the state vector, **y** is the measurement vector, **b** is the model parameter vector, F(**x**, **b**) is the forward model (i.e., simulated measurement vector), and $\boldsymbol{\epsilon}$ is the measurement model uncertainty vector. In the measurement vector **y**, ΔTB corresponds to the brightness temperature difference (i.e., $TB_{\text{clear sky}} - TB_{\text{cloudy}}$). The model parameter vector, **b**, contains ancillary parameters that are not perfectly known to the observer and

not retrieved from the measurements, but are needed by the forward model (e.g., the assumed ice particle model, satellite viewing zenith angle, and cloud top height). Note that the above quantities in **x** and **y** represent examples of possible state and measurement vector quantities, and therefore is not meant to imply these are the only values used in the rest of the presented work.

We find the optimal estimation of the state vector by minimizing the following scalar cost function,

$$\mathrm{J} = [\mathbf{y} - \mathrm{F}(\mathbf{x}, \mathbf{b})]^{\mathrm{T}} \mathbf{S}_{\mathbf{y}}^{-1} [\mathbf{y} - \mathbf{F}(\mathbf{x}, \mathbf{b})] + (\mathbf{x} - \mathbf{x}_{\mathrm{a}})^{\mathrm{T}} \mathbf{S}_{\mathrm{a}}^{-1} (\mathbf{x} - \mathbf{x}_{\mathrm{a}}), \tag{4.16}$$

where $\mathbf{S}_{\mathrm{a}}$ and $\mathbf{S}_{\mathrm{y}}$ are the *a priori* uncertainty covariance matrix and the measurement covariance matrix, respectively. It is evident from the equation above that if the probability density function (PDF) attributed to $\mathbf{x}_{\mathrm{a}}$ is not too narrow (i.e., retrieval parameters not highly constrained by *a priori* assumptions), the cost function offers an assessment of the consistency between the forward model and the measurements. Because of nonlinearity in this problem, there is no general explicit expression for locating optimal solutions. Therefore, they must be found numerically and iteratively (Rodgers 2000). For this purpose, the Levenberg-Marquardt iterative method is used to find the zero of the gradients of the cost function J. Following the formalism of Rodgers (2000), the threshold of an optimal solution should be roughly the number of measurement elements, m (i.e., ~3 shown in Eq. 4.15). Since no actual sub-mm measurements are currently available, the measurement noise has to be estimated. Because of this, we select a threshold of $2m$ to obtain an optimal solution, which is

slightly larger than that outlined in Rodgers (2000). The measurement error covariance matrix is separated into the following:

$$\mathbf{S}_{\mathrm{y}} = \mathbf{S}_{\mathrm{fwd}} + \mathbf{S}_{\mathrm{meas}} + \mathbf{S}_{\mathrm{unknown}}, \tag{4.17}$$

where $\mathbf{S}_{\mathrm{fwd}}$ is the uncertainty due to assumptions made in the forward model such as the atmospheric profile, $\mathbf{S}_{\mathrm{meas}}$ represents noise related to satellite measurement signals, and $\mathbf{S}_{\mathrm{unknown}}$ denotes the uncertainty associated with cloud and atmospheric characteristics that are challenging to quantify, such as cloud 3D effects. In order to calculate the forward model uncertainty, many simulations are conducted in which water vapor and temperature profiles are perturbed and added to random Gaussian noise. Since there are currently no spaceborne sub-mm sensors operating at the frequencies used in this work, we assume a noise equivalent temperature difference (NEΔT) of 2 K for all sub-mm channels. NEΔT is the *TB* difference that produces a change in signal equivalent to the radiometer noise level. This value is based on estimates from clear-sky flight data. For $\mathbf{S}_{\mathrm{unknown}}$, we assume a diagonal matrix, and since it is very challenging to quantify uncertainty due to cloud inhomogeneity and 3D effects (clouds partly obscuring each other when viewed from the side), we assume a constant proportion of 5% of the signal in all channels. Cloud inhomogeneity and polarization effects will have follow-on impacts for ice cloud retrievals which depend on 1D unpolarized forward models. Differences arising between 3D and 1D have two main causes:

1. Field of view (FOV) averaging over radiances that are in the nonlinear radiative transfer regime, or have a large optical path, will cause systematic biases when compared to a 1D representation with equivalent FOV averaged cloud optical

depth. This is referred to as beam-filling and is not much of a concern for sub-mm measurements, since sub-mm typically lies in the linear radiative transfer regime.

2. Actual 3D radiative transfer effects resulting from photon transport perpendicular to the viewing direction through inhomogeneity which is not present in the 1D representation. This is the 3D radiative transfer effect.

Note that rigorous characterization of cloud 3D effects is beyond the scope and framework of this thesis.

Another reason Optimal Estimation algorithms are a popular choice for remote sensing retrievals is the explicit parameterization of the sources of error and the capability to propagate them into approximations of retrieval uncertainty. The error is defined as

$$\mathbf{S}^{-1} = \mathbf{K}^{\mathrm{T}}\mathbf{S}_{\mathrm{y}}^{-1}\mathbf{K} + \mathbf{S}_{\mathrm{a}}^{-1}, \tag{4.18}$$

where **K** is the Jacobian matrix defined in Eq. 4.6. Retrieval uncertainty is the square root of the diagonal elements of **S**.

4.6.2. Levenberg-Marquardt iteration

A significant issue in retrievals is the existence of nonlinear inverse problems, which can arise from having a nonlinear forward model, or can be imposed by an *a priori* constraint (i.e., a non-Gaussian pdf as *a priori* information). The primary difference between linear and nonlinear problems is that in the nonlinear case there is no general explicit expression for locating optimal solutions. Consequently, optimal solutions in the nonlinear case must be found numerically and iteratively. Newtonian

iteration is an uncomplicated numerical method capable of finding the zero of the gradients of the cost function if the problem is only moderately nonlinear (Rodgers, 2000). Methods such as Newton's and Gauss-Newton will locate the minimum of the cost function in one step if the cost function is precisely quadratic in x. Conversely, it is possible that the surface is so poorly represented by a quadratic that a step taken is meaningless or even increases the residual. To mitigate this, the Levenberg-Marquardt (LM) algorithm was developed to find the local minimum of the nonlinear least squares problems.

The original iteration proposed by Levenberg (1944) included a damping term (γ_i) which is chosen at each step to minimize the cost function. The LM algorithm combines two numerical minimization techniques. If γ approaches 0, then the step tends toward the Gauss-Newton method, and if γ approaches infinity, the step tends toward the steepest descent method (Rodgers, 2000). Therefore, we can say the LM algorithm adaptively adjusts the parameter updates between the Gauss-Newton and the steepest descent update. The iteration equation is

$$\mathbf{x}_{i+1} = \mathbf{x}_i + [(1+\gamma)\mathbf{S}_\mathrm{a}^{-1} + \mathbf{K}_i^\mathrm{T}\mathbf{S}_\epsilon^{-1}\mathbf{K}_i]^{-1} \left\{\mathbf{K}_i^\mathrm{T}\mathbf{S}_\epsilon^{-1}[\mathbf{y} - \mathbf{F}(\mathbf{x}_i)] - \mathbf{S}_\mathrm{a}^{-1}[\mathbf{x}_i - \mathbf{x}_\mathrm{a}]\right\}. \quad (4.19)$$

There is some experimentation required when utilizing this method to determine an appropriate initial γ as well as the factor by which it increases or decreases each iteration. The conventional approach, which is adopted for this work, is to select a large initial γ value so that the first updates are small steps in the steepest descent direction. The overall flow of the iteration process is as follows. For the first iteration, we provide

an initial **x** and γ, and then the cost value is computed. From there, we compute a new **x** based on Eq. 4.19 and compute the cost again. If this cost is greater than the previous one, we increase γ and try again (without updating **x**). We compute the cost again based on the new γ, and if the cost is less than the previous cost value (which is the goal) then we check for convergence. The retrieval has converged on an optimal solution if $\mathrm{J}_{i+1} - \mathrm{J}_i$ is small (typically less than 1) and $\mathrm{J}_{i+1} < m$, where m is the number of elements in the measurement vector **y**. This is a typical convergence criterion. As mentioned in the previous section, we define an optimal solution for the purposes of this work using $2m$ (e.g., if the number of elements in the measurement vector is 2, we denote a solution as optimal if the cost function is less than 4).

4.6.3. Information content

Solving the inverse problem is not always straightforward. For example, the problem could be ill-conditioned or ill-posed, and is often nonlinear. To acquire an understanding of the nature of the problem, investigating properties of the information contained in the measurements is useful. Previous studies have implemented information content theory analyses before, or in conjunction with, retrievals to quantify the amount of information expected for the parameters to be retrieved successfully (e.g., Sourdeval et al., 2013). Through this analysis, retrieval algorithms can be designed in a way to maximize the information in measurements, therefore ensuring that sufficient information is present to retrieve the parameters of interest.

In this study, we first compute the degrees of freedom for signal (*DOF*), which represents the number of independent pieces of information (related to the parameters to

be retrieved) present in the measurement. In broader terms, we can consider *DOF* as an intuitive non-dimensional metric of the value added by the observations projected onto a specific state variable. We define *DOF* as

$$DOF = \mathrm{tr}(\mathbf{A}) , \tag{4.20}$$

where **A** is the averaging kernel matrix, which is the derivative of the posterior state with respect to the true state, defined as

$$\mathbf{A} = {}^{\partial \hat{\mathbf{x}}}/_{\partial \mathbf{x}} . \tag{4.21}$$

Another way to understand **A** is to think about the diagonal terms as representative of the sensitivity of each retrieved parameter to its corresponding truth.

The second aspect of information content utilized in this study is Shannon Information Content (*SIC*), which is essentially a measure of the relative improvements to our *a priori* knowledge that results from the addition of measurements (Rodgers 2000). Since the idea of *SIC* is typically less familiar and intuitive than *DOF*, we present this simple analogy. Conceptually, it is analogous to refining a tape measure by subdividing each prior division into several new divisions, which is a function of *SIC*. Therefore, the larger the *SIC*, the more information content is present, subsequently leading to a higher resolution of tick marks and allowing one to resolve the quantity of interest more accurately. For completeness, we include a brief summary of salient characteristics of the information content methodology. In this work, the information content *SIC* is defined as the reduction in entropy *S* between states P_x(final state) and P_a(initial state),

$$SIC = S(\mathrm{P_x}) - S(\mathrm{P_a}) . \tag{4.22}$$

If we assume that distributions of the above states are Gaussian, information can be rewritten in terms of their covariances **S**,

$$SIC = \frac{1}{2}\log_2|\mathbf{S}_x\mathbf{S}_a^{-1}|\,, \tag{4.23}$$

where the initial state covariance ($\mathbf{S}_a$) is typically represented as the expected climatological range of ice cloud properties, and the final state covariance ($\mathbf{S}_x$) is described by the error covariance matrix of the retrieved cloud properties (L'Ecuyer et. al., 2005).

5. SUB-MM RADIANCES AND ICE CLOUD PROPERTIES

Since there are currently no available spaceborne sub-mm measurements at the frequencies considered in this study, and because there are missions planned to leverage sub-mm measurements for ice cloud property retrievals, an overarching goal of this work is to develop a holistic understanding of how sub-mm radiation interacts with ice clouds. To that end, a significant portion of this project is devoted to conducting a series of numerical experiments to investigate the response of upwelling sub-mm radiation to differing ice cloud characteristics. A particular emphasis is placed on understanding vertical and horizontal polarization signatures, and their ability to provide additional information on ice cloud microphysical properties, such as particle shape and orientation. Expanding our knowledge of the interaction of ice clouds with sub-mm radiances allows for the development of robust algorithms to infer ice cloud properties once planned sensors are operational and data is available. Furthermore, as it is necessary to make assumptions in retrievals to reduce the degrees of freedom of the problem to make it more tractable, conducting these numerical experiments facilitates assessment of the impact and appropriateness of these assumptions.

In Chapter 4 we outlined the tools and methods necessary to accomplish the above goals. In this chapter we present some of the numerical experiments conducted. The sensitivity of the refractive index of ice to temperature in the sub-mm spectral region and the subsequent impact of assuming a fixed cloud top height (i.e., temperature) on retrievals of *IWP* and D_{eff} is discussed in Section 5.1. In Section 5.2 we demonstrate

how assuming a single ice particle shape (or habit) impacts such retrievals when using unpolarized measurements. We also investigate the additional information content provided by polarized measurements, since polarization is sensitive to particle shape.

5.1. Temperature dependence of refractive index

As mentioned in Chapter 1, General Circulation Models vary in their estimation of cloud *IWP* by as much as an order of magnitude. Imposing constraints from observations is difficult for several reasons, but a major challenge is that ice mass retrievals are generally ill conditioned (i.e., less information content in the observations than in the solution). Even with the benefits mentioned in Chapter 2 of sub-mm radiometry to infer ice mass, it is necessary to make assumptions in ice cloud retrievals such as particle shape which effects the particle single scattering properties. Previous studies such as Ding et. al. (2017) have demonstrated the sensitivity of ice particle single scattering properties in the sub-mm spectral region to ice refractive index at certain temperatures. Here we present an information content-based investigation of the temperature effects on the refractive index, and subsequent contributions to ice cloud property retrieval biases over sub-mm and infrared wavelengths.

Accurate calculations of the single scattering properties of ice particles, such as extinction efficiency (Q_{ext}), single scattering albedo ($\tilde{\omega}$), asymmetry parameter (g), and scattering phase matrix (P), are essential to accurately retrieve ice cloud properties. Successful calculation of these properties requires knowledge of the complex refractive index of ice, as well as its dependence to environmental factors such as temperature. Recall, the real part of the refractive index determines the phase speed of

electromagnetic waves (i.e., how fast it propagates through a medium) and the imaginary part is related to the rate of absorption of the wave. Figure 5.1 below, taken from Ding et al. (2016), shows the dependence of the real and imaginary parts of the refractive index on temperature and sub-mm frequencies up to ~1000 GHz. From this figure you can see that the real part of the refractive index exhibits a weaker frequency dependence than the imaginary part and remains fairly constant over this frequency and temperature range. The imaginary part decreases with increasing frequency but increases with increasing temperature.

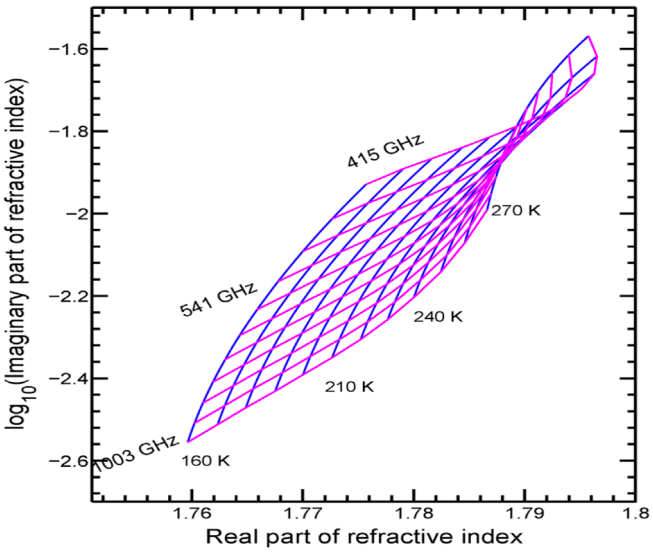

Figure 5.1: Temperature sensitivity of the refractive index in the sub-mm spectral region. The base ten log of the imaginary (real) part is shown in the y (x) axis. Reprinted from Ding et al., 2017.

The sensitivity of the refractive index to temperature can lead to errors in retrievals, if for instance you assume a particular cloud height/temperature that varies from the temperature at which the single-scattering properties are calculated. Figure 5.2

demonstrates how the temperature sensitivity of the refractive index can lead to differences in single scattering albedo. From Fig. 5.2 we see that as temperature increases, the single scattering albedo decreases. This makes sense because as temperature increases the imaginary part of the refractive index increases, and consequently so does absorption. To better understand the sensitivity of the single-scattering properties of ice particles to temperature and subsequent implications in cloud property retrievals, we pose the following scientific questions:

1. What is the bias of retrieved *IWP* and D_{eff} when assuming a fixed temperature in scattering property calculations at sub-mm frequencies?
2. If a bias exists, is it reduced by the addition of infrared (IR) measurements, in which the refractive index is less sensitive to temperature?

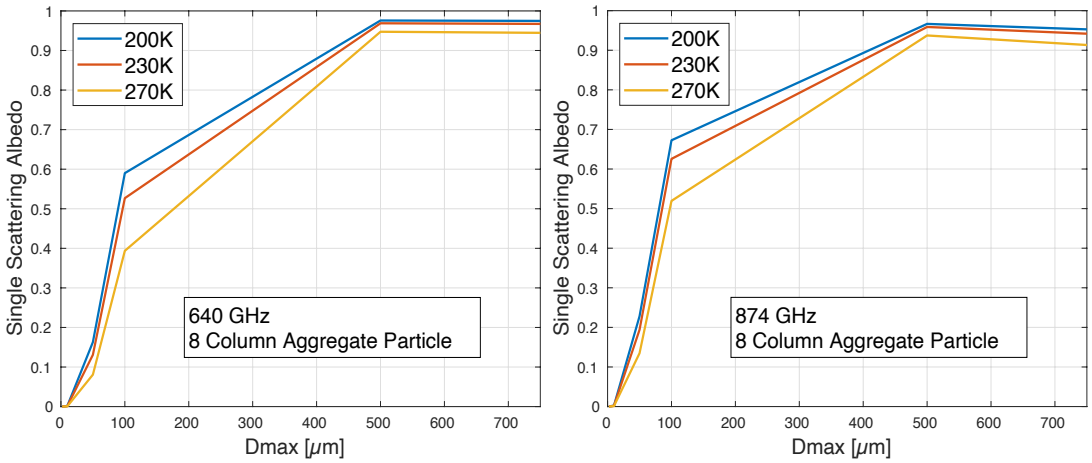

Figure 5.2: Single scattering albedo for two sub-mm channels at three temperatures. Albedo is shown as a function of particle maximum diameter (Dmax)

5.1.1. Impact of temperature dependent refractive index on retrievals

To address the above questions and explore how the temperature dependence of sub-mm refractive indices impacts retrievals, we employ the following experimental setup:

- Control: single-scattering properties are computed at 200 K, which are used to generate both the synthetic data as well as the retrieval lookup table (LUT).
- Experiment 1: synthetic data is the same as in the control, but the single-scattering properties used to generate the retrieval LUT are computed at 230 K.
- Experiment 2: same as Experiment 1, except single-scattering properties and subsequent retrieval LUT are computed at 250 K.
- Experiment 3: variable temperature is used to compute single-scattering properties, which correspond to the cloud top height. This is used for both the data generation and the retrieval.

In order to determine the retrieval bias, we calculate the Mean Bias Error (MBE) defined as total, or in terms of *IWP* or D_{eff} as:

$$\mathrm{MBE}_{\mathrm{Total}} = \mathrm{mean}\left(\mathbf{x}_{\mathrm{true,i,j}} - \mathbf{x}_{\mathrm{retrieved,i,j}}\right);\ \ \mathbf{x} = \left[IWP_{\mathrm{j}}, Deff_{\mathrm{j}}\right] \tag{5.1}$$

$$\mathrm{MBE}_{IWP} = \mathrm{mean}\left(\mathbf{x}_{\mathrm{true,i,j}} - \mathbf{x}_{\mathrm{retrieved,i,j}}\right);\ \ \mathbf{x} = \left[IWP_{\mathrm{j}}, 150\mu\mathrm{m}\right] \tag{5.2}$$

In Eqns. 5.1 and 5.2, i = 500, meaning we compute the error of one pixel 500 times then take the mean value of these errors to be the MBE.

We also employ two metrics of information content, degrees of freedom for signal (*DOF*) and Shannon Information Content (*SIC*). In all simulations a 1 km thick ice cloud from 9 to 10 km is assumed for a tropical atmosphere, and the viewing zenith angle is 53˚. Ice particles are assumed to follow a gamma size distribution with an

effective variance of 0.1. Figure 5.3 shows the MBE of retrieved *IWP* for the experiments defined above, when only using sub-mm measurements. The Control and Experiment 3 have roughly the same distribution and magnitude of MBE. This is not surprising since they both utilize LUTs generated from single-scattering properties which are calculated at the cloud top temperature. As expected, Experiment 2 shows the poorest performance, since it contains the largest gap in temperatures used to generate the synthetic data and LUTs.

Next, focus on the uppermost right area of the panels in Fig. 5.3 where *IWP* and D_{eff} are large. As you move from the Control to Experiments 1 and 2, this area goes from overestimating *IWP* (negative MBE) to underestimating it (positive MBE). A similar result is shown in Ding et al. (2017). This can be explained by the following. As *IWP* increases, a smaller fraction of atmospheric emission below the cloud is transmitted to the top of the cloud. As *IWP* continues to grow, it reaches a threshold at which the cloud obstructs nearly all radiation emitted below the cloud. Consequently, the sensor is now simply measuring the radiation above the cloud, which is practically invariant with *IWP*. In the case of Experiment 2, the retrieval LUT is generated from scattering properties calculated at 250 K compared to those used to generate the synthetic data which are computed at 200 K. As *IWP* and D_{eff} increase to produce an increasingly optically thick cloud, *TB* computed from 250 K is larger than *TB* computed at 200 K. This leads to an underestimation of retrieved *IWP*, and in the case of Fig. 5.3 a positive MBE.

It is also worthwhile to note that the differences among the presented experiments primarily occurs at large particle sizes. This is because the dependence of

the single-scattering properties on temperature increases at higher frequencies and larger particles. Above we presented an explanation for the positive MBE at high *IWP* and D_{eff} in Experiment 2. Now let us consider the enhanced negative MBE for large D_{eff} and moderate *IWP* values. As temperature increases, the imaginary part of the refractive index increases, and the single scattering albedo decreases. This signifies and increase in absorption and a decrease in scattering. As a consequence, TB and ΔTB are biased low and high, respectively, which results in the overestimation of *IWP* and produces the enhanced negative MBE seen in the bottom left panel of Fig. 5.3.

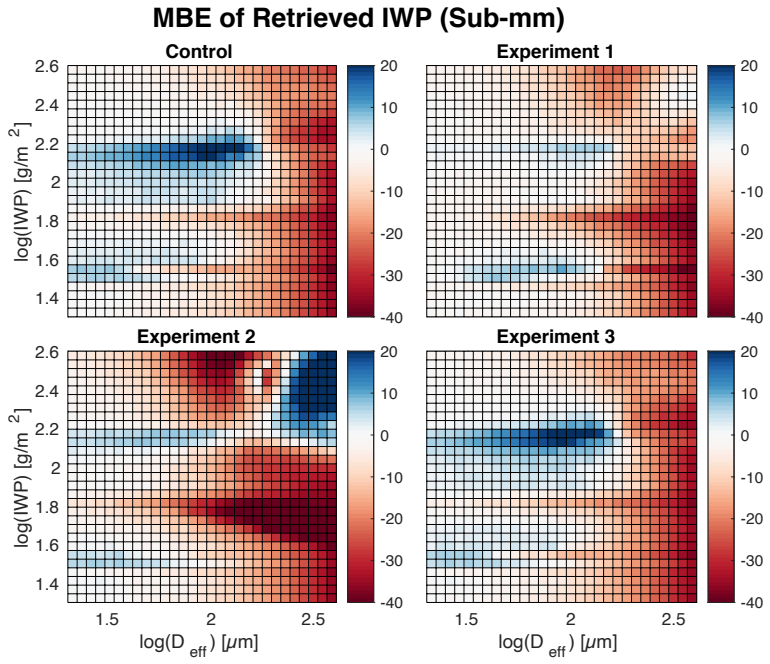

Figure 5.3: Mean Bias Error (MBE) of retrieved *IWP* for only sub-mm measurements. Each panel represents one of the experiments mentioned above. X and Y axes denote the log (base 10) of D_{eff} [μm] and *IWP* [g/m^2], respectively.

To further demonstrate that the temperature dependence of single-scattering properties is the most significant at large frequencies and large particles, we retrieve D_{eff}

but isolate the response to individual *IWP* and D_{eff} values. The results are provided in Fig. 5.4, which shows MBE of retrieved D_{eff} as a function of *IWP* at intermediate and larger D_{eff} values (150 and 250 μm). The first things to note about this figure is that Experiment 2 again exhibits the largest bias, and there is little difference between Experiment 3 and the Control. However, the main takeaway from this figure is the transition from negative to positive bias shown in the right panel. Notice that when *IWP* is less than roughly 100 g/m^2 the bias from the experiments is negative, and as *IWP* increases the bias becomes positive. This is primarily due to the nonlinearity of sub-mm *TB* and ΔTB for the *IWP* and D_{eff} values shown in Fig. 5.4. In this region of the parameter space, the nonlinearity is significant, and leads to ΔTB peaks at roughly 130 and 200 μm for 874 and 640 GHz, respectively. To clarify, when plotting ΔTB as a function of D_{eff} for a particular *IWP* shown in Fig. 5.4, ΔTB is almost zero for very small D_{eff} values and increases with increasing D_{eff} until reaching a maximum at roughly 130 μm (for 874 GHz and *IWP* of 100 g/m^2), and then decreases as D_{eff} increases. Therefore, the reason all the biases of retrieved D_{eff} are negative in the left panel, is because a D_{eff} of 150 μm corresponds to mostly the left side of the ΔTB peak. As mentioned previously, as the temperature at which the single-scattering properties becomes larger, *TB* decreases and ΔTB increases. This causes the retrieval to overestimate the true D_{eff}, and hence the negative MBE in the left panel of Fig. 5.4. The converse is true for the right panel. An increase in ΔTB resultant from single-scattering properties calculated at a higher temperature leads the retrieval to underestimate the true D_{eff}. Again, note that the right panel suffers most from the nonlinear response of *TB* to D_{eff}, leading to a multivalued

solution problem. Therefore, it may be necessary to add additional measurements which are sensitive in that range to further constrain the retrieval. Lastly, note the magnitude of the differences among experiments in the two panels, and that the larger magnitude for D_{eff} of 250 µm further demonstrates the dependence of the single-scattering properties on temperature increases for larger particles.

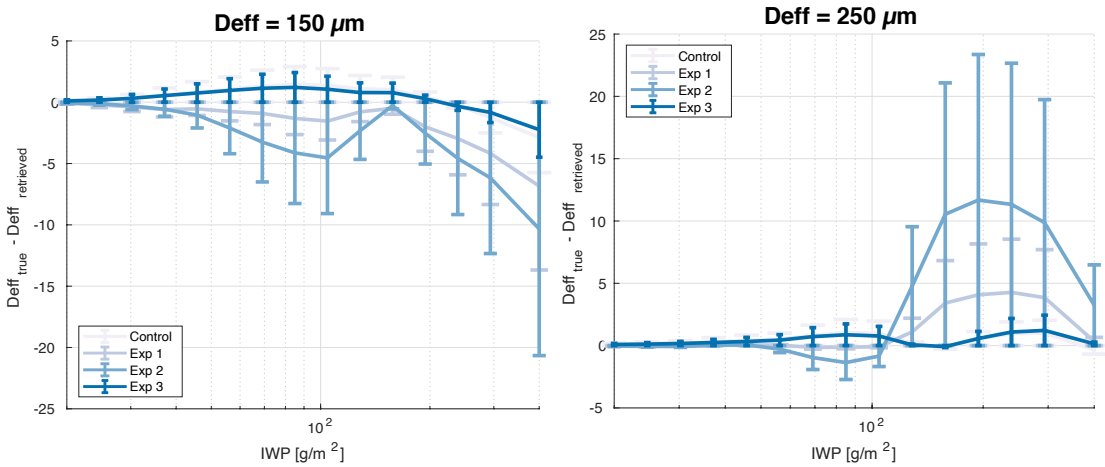

Figure 5.4: MBE of retrieved D_{eff} as a function of *IWP* for sub-mm and IR measurements. The true values of D_{eff} are set to 150 µm (left) and 250 µm (right). Units are in µm.

Now that we have demonstrated the potential for bias of retrieved *IWP* or D_{eff} when assuming a fixed temperature in scattering property calculations, we can proceed and address the second question posed. Here we investigate whether the addition of IR measurements can reduce this bias. The MBE of retrieved *IWP* and D_{eff} are provided in Figs. 5.5 and 5.6, respectively. These retrievals utilize both sub-mm and IR measurements (640, 874 GHz; 12 µm). First note that MBE of retrieved *IWP* (Fig. 5.5) is positive in more regions of the parameter space than for the MBE of retrieved D_{eff}

(Fig. 5.6). Based on how MBE is defined, a positive value implies the retrieval is underestimating the true value.

When comparing Figs. 5.3 and 5.5, we see improvement in the Control (top left panels). However, there is little or no improvement to the remaining experiments. This means there is not sufficient information content or sensitivity present in the IR measurements to overcome the bias which results from assuming the incorrect temperature to compute the scattering properties of ice particles. In addition, it is further evident that the poorest performance corresponds to Experiment 2. In this panel we again see that the MBE of retrieved *IWP* is negative in many cases, with a significant enhancement of negative MBE when particles are large. The reason for this is the same as described above for the same phenomenon in Fig. 5.3. To reiterate, as the temperature at which the single-scattering properties are computed increases, the imaginary part of the refractive index increases, and the single scattering albedo decreases. The net effect is increased absorption and decreased scattering, which leads ΔTB to be biased high and results in the retrieval overestimating the true *IWP* (i.e., a negative MBE).

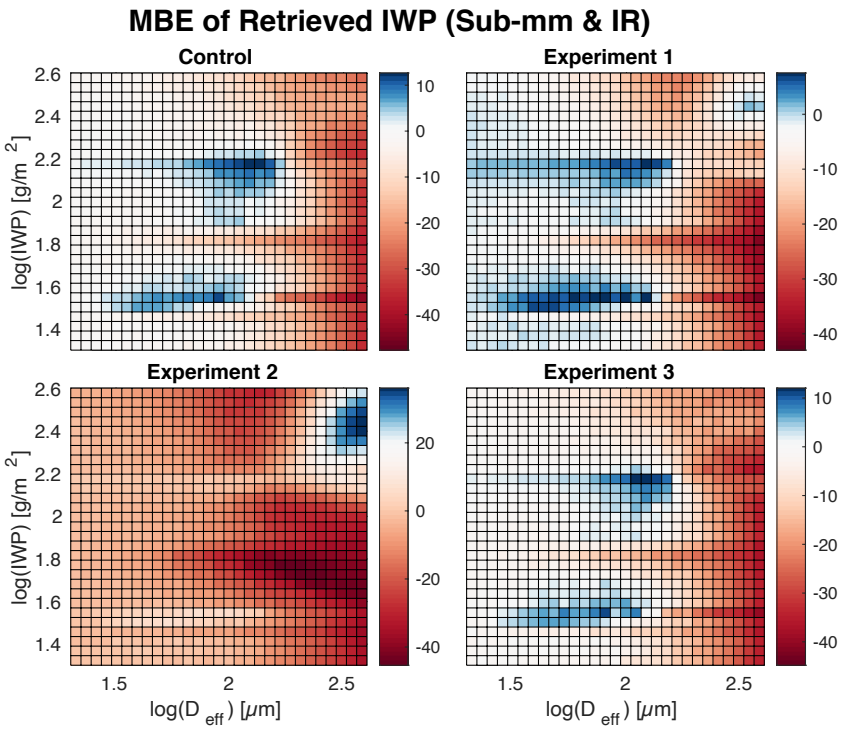

Figure 5.5: MBE of retrieved *IWP* for sub-mm and IR measurements. Units are in g/m^2.

Overall, there is little variation in the MBE of retrieved D_{eff} (Fig. 5.6), with the exception of the striping feature for moderate to small *IWP* and large D_{eff}. Again, this is likely due to the nonlinear nature of sub-mm *TB*, which results in multivalued solutions. We previously explained the issue of multiple solutions for Fig. 5.4 in terms of one state variable (e.g., a plot of ΔTB versus D_{eff}). Let us discuss it now in terms of the whole parameter space. For example, in the event there are two solutions, meaning two pairs of D_{eff} and *IWP* can produce roughly the same *TB*, the cost function can be thought of as a plane with two minimum values, with the global minimum being the true solution. If the solution is trapped in a local minimum, but it is not the true solution, we must add an additional measurement or employ some regularization (smoothing) technique to the parameter space. For D_{eff} retrievals at small *IWP* (where MBE is positive in Fig. 5.6),

adding an IR measurement most often results in the retrieval converging on the smaller of the two possible D_{eff} values. This leads the retrieval to underestimate the true D_{eff} and consequently produces a positive MBE. However, for *IWP* values outside those that show a positive MBE of retrieved D_{eff}, adding an IR measurement results in the retrieval converging on the true solution.

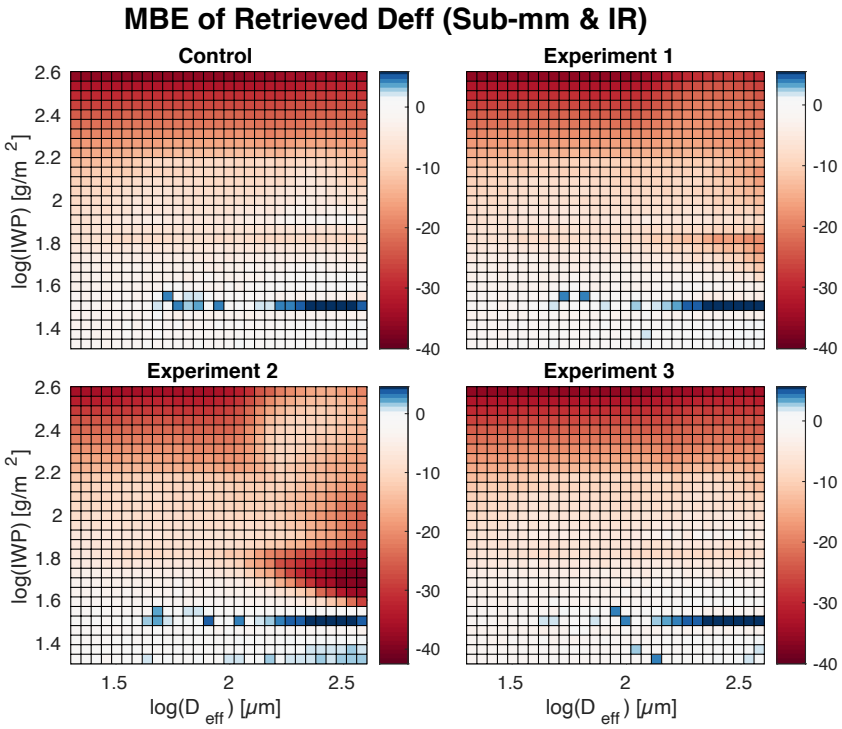

Figure 5.6: MBE of retrieved D_{eff} for sub-mm and IR measurements. Units are in μm.

Comparing the panels in Fig. 5.6, it is evident that Experiment 2 (bottom left) again provides the least consistency between true and retrieved D_{eff}. Note that the MBE of retrieved D_{eff} shows the familiar large negative value at small to moderate *IWP* and large D_{eff} as is demonstrated in previous figures. This means that the retrieved D_{eff} is overestimated compared to the true value. As mentioned above, *TB* simulated from ice

particle single-scattering properties calculated at 250 K is larger than *TB* when scattering properties are computed at 200 K. This translates to a reduced ΔTB. Because ΔTB decreases with increasing D_{eff} in this part of the parameter space (negative slope), the reduction in ΔTB that results from calculating particle scattering properties at a higher temperature leads to a larger retrieved D_{eff}, and consequently a negative MBE.

These experiments show that the temperature assumed in calculating the single scattering properties of ice crystals leads to a bias in sub-mm *TB*, and subsequently retrieved *IWP* and D_{eff}. The larger the discrepancy between the temperature assumed in light scattering calculations and the temperature within the cloud, the larger potential for significant bias of retrieved *IWP* and D_{eff} . While the addition of IR measurements can improve such retrievals, the relative improvement from this additional measurement does not wholly compensate for the bias introduced from assuming an unrepresentative temperature to calculate the scattering properties of ice particles. This is one indication that the cloud top height should also be retrieved. Finally, it is worth reiterating that the dependence of the single-scattering properties on temperature increases for larger particles.

5.1.2. Temperature sensitivity of sub-mm refractive indices and information content

In addition to conducting retrievals, we leverage degrees of freedom for signal (*DOF*) and Shannon Information Content (*SIC*), to further understand how the temperature dependence of sub-mm refractive indices impacts ice cloud property retrievals. Details of the *DOF* and *SIC* are provided in Chapter 4. The *DOF* of retrievals

using only sub-mm measurements and retrievals which include an IR measurement are presented in Figs. 5.7 and 5.8, respectively. When looking at the sub-mm only case (Fig. 5.7), note that there are several pixels with little or no information in the area of low *IWP* and D_{eff}. As a technical note, the retrieval can still converge on a solution that is not "optimal", meaning the cost function converged, but to a larger value than what is prescribed for an "optimal" retrieval. This criterion is typically set to equal the number of elements, m, in the measurement vector (Rodgers 2000). However, for this work we select a threshold for an optimal solution to be $2m$, which in the case of sub-mm only is 4. This allows for solutions with increased measurement noise, and because there are no current spaceborne measurements we erred on the side of larger values when estimating measurement noise. If the retrieval does not return an optimal solution, the resultant *DOF* and *SIC* are not included in the average. Furthermore, if the percent of pixels which provide an optimal solution in a bin is more than one standard deviation from the median value for the entire parameter space, we do not average the values of *DOF* or *SIC* in that pixel and it is marked white.

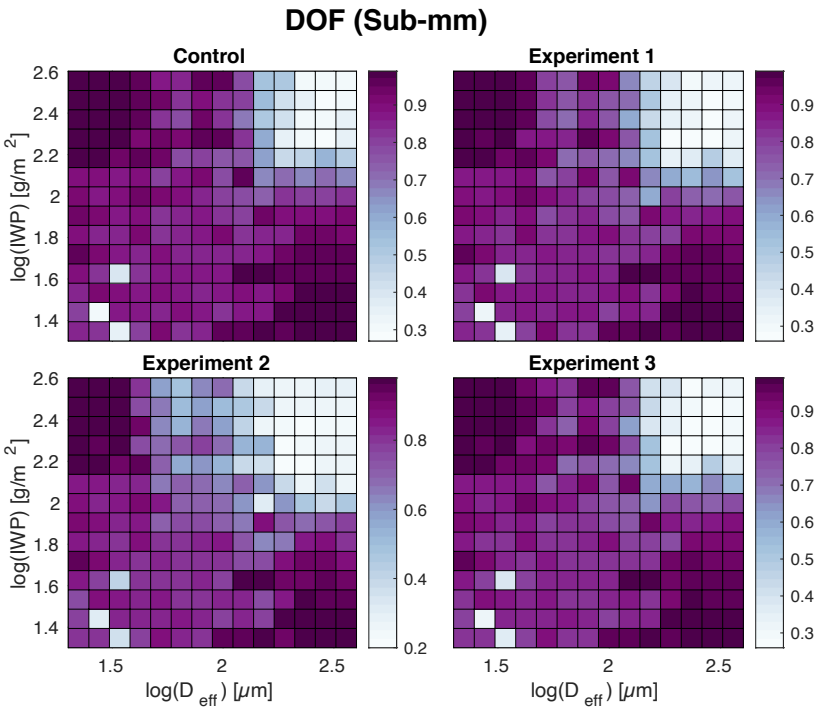

Figure 5.7: *DOF* for temperature sensitivity experiments using only sub-mm measurements.

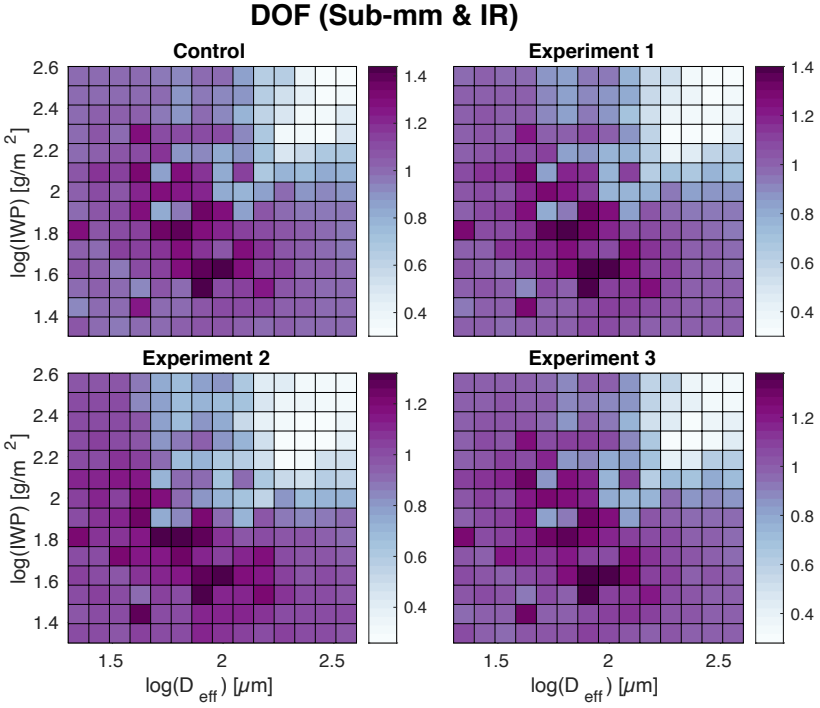

Figure 5.8: *DOF* for temperature sensitivity experiments using sub-mm and IR measurements.

An important takeaway in comparing *DOF* for both the sub-mm only case (Fig. 5.7) and the case when IR is included (Fig. 5.8) is that the magnitude of *DOF* is much larger in the latter. The largest *DOF* values increase from ~1 when only sub-mm measurements are utilized and increases to ~1.4 after including an IR measurement in the retrieval. Recall, *DOF* represents the number of independent pieces of information (related to the parameters to be retrieved) present in the measurement. It is also useful to think about *DOF* in terms of the trace of the averaging kernel matrix, **A**. The averaging kernel matrix, as defined in Eq. 4.20, is the derivative of the posterior state with respect to the true state. In other words, the diagonal elements of **A** represent the sensitivity of each retrieved parameter to its corresponding truth. Taking the trace simply sums up these diagonal elements to provide the total *DOF*. A larger *DOF*, with 2 being the theoretical maximum for these retrievals, therefore signifies sufficient information is present to simultaneously retrieve the two parameters of interest. In other words, there exists sufficient independent pieces of information such that the two parameters are separable. The increase of *DOF* between Figs. 5.7 and 5.8 further demonstrates the usefulness of including IR and sub-mm measurements to simultaneously infer *IWP* and D_{eff}.

Now comparing the different experiments for both cases, it is apparent that there is little distinction among them in terms of information content, although it is evident that Experiment 2 exhibits the lowest overall *DOF*. This makes intuitive sense as the temperature difference used in the single scattering property calculations (i.e., synthetic data and retrieval LUT) is the largest. Figures 5.7 and 5.8 also illustrate the lack of

information for large *IWP* and D_{eff}. This is expected because as *IWP* and D_{eff} increases, the difference between clear and cloudy sub-mm TB saturates due to increased optical thickness and multiple scattering within the cloud. Therefore, in the case of these optically thick clouds, there is not sufficient information content in the measurements (independent pieces of information) to infer either *IWP* or D_{eff}, let alone both simultaneously.

Let us now look at the *SIC* corresponding to the sub-mm only retrieval and when IR is added, which is presented in Figs. 5.9 and 5.10, respectively. Recall that *SIC* is essentially a measure of the relative improvements to our *a priori* knowledge that results from the addition of measurements (Rodgers, 2000). Figures 5.9 and 5.10 show that there is still little information when *IWP* and D_{eff} are large. Note, there is again low information content (small *SIC*) for sub-mm only retrievals (Fig. 5.9) when *IWP* and D_{eff} are small. This means that for optically thin clouds (small *IWP* and D_{eff}), sub-mm measurements provide little improvement to our *a priori* knowledge regarding the *IWP* and D_{eff} of these clouds. However, when adding an IR measurement (Fig. 5.10) there is a significant increase in *SIC* for lower *IWP* and moderate to small sized particles, where IR measurements are sensitive. Also note the maximum magnitude of *SIC* in the sub-mm only case is ~2 and increases to 5.5 when an IR measurement is included. This again speaks to the usefulness of combining sub-mm and IR measurements.

Similar to *DOF*, there is also little variance in *SIC* among the different experiments, with the exception to some extent of Experiment 2. In terms of both *DOF* and *SIC*, the most noticeable difference between Experiment 2 and the others is the

reduction of information at moderate D_{eff} values and large *IWP*. This happens because this is an area which already has particularly low sensitivity to D_{eff}. For example, if we again consider plotting ΔTB as a function of D_{eff}, we see that for moderate *IWP* and large D_{eff} the slope of the curve small. Therefore, it is easy to imagine how in this case a small change in the y-axis of this imaginary plot can lead to a significant change in x. Consequently, by assuming a specific temperature to calculate the single scattering properties of ice particles can lead to a difference of several K when computing *TB*.

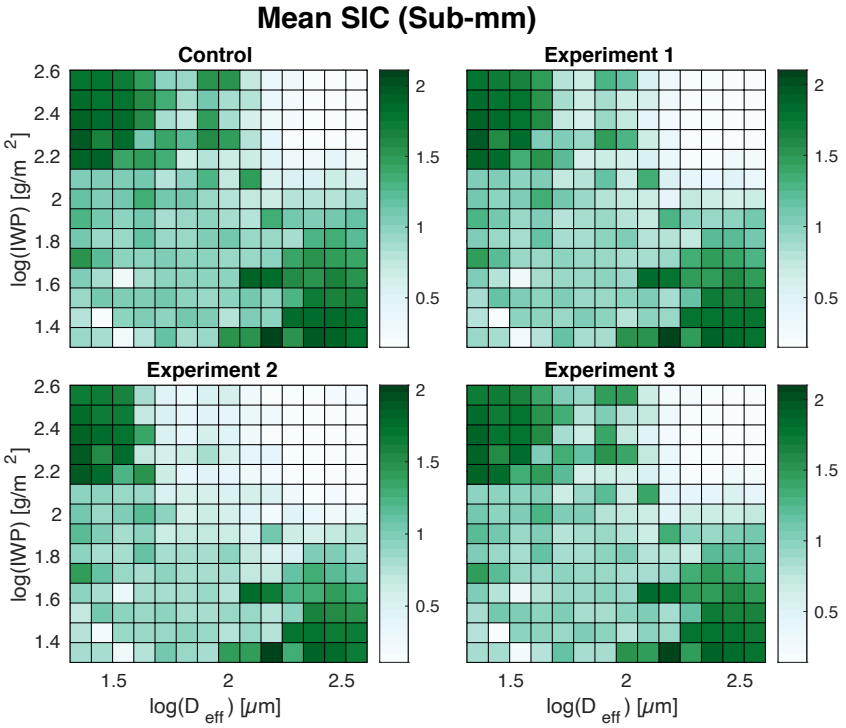

Figure 5.9: *SIC* for temperature sensitivity experiments using only sub-mm measurements.

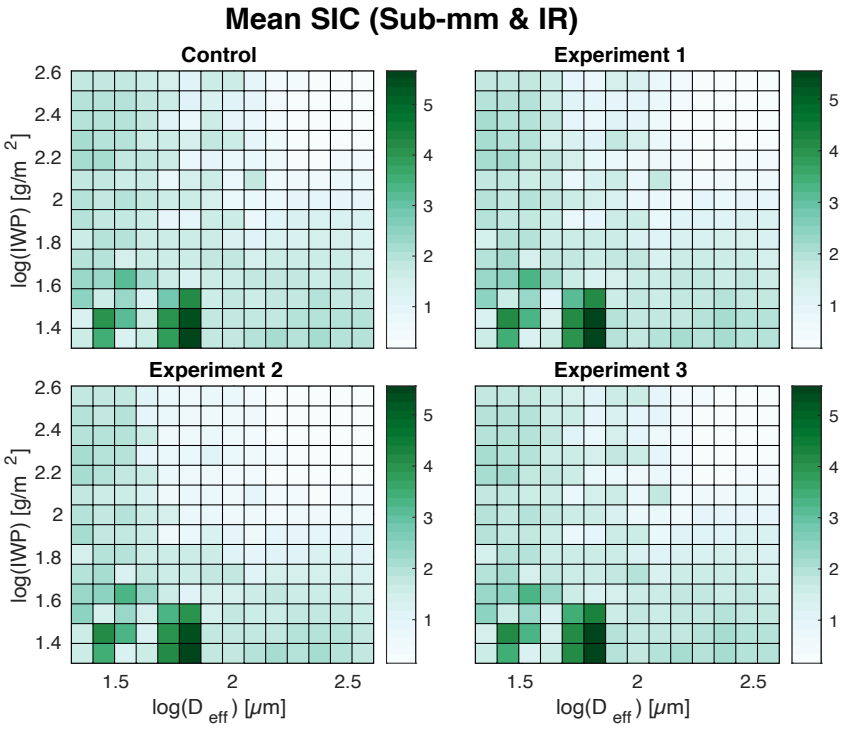

Figure 5.10: *SIC* for temperature sensitivity experiments using sub-mm and IR measurements.

5.1.3. Conclusions

In order to simulate the *TB* associated with ice clouds, it is necessary to compute the single scattering properties of the ice particles within cloud. These properties, which explain the interaction of electromagnetic radiation and ice particles, depend on the dielectric properties of the particle, as well as particle shape, size distribution, and orientation. Of particular importance when considering the particle composition, is the complex index of refraction, which varies with the frequency and the temperature of the particle. While it has previously been the convention to select a singular refractive index per measurement band, studies such as that by Ding et al. (2017) showed that the refractive index in the sub-mm spectral region is sensitive to temperature. This is particularly the case for large particles. To understand how this sensitivity is manifested

in ice cloud property retrievals, we simulated synthetic data using ice particle single scattering properties which were computed at 200 K, and retrieval LUTs are computed at different temperatures.

These experiments show that the temperature assumed in calculating the single scattering properties of ice crystals leads to a bias in sub-mm *TB*, and subsequently to biases of retrieved *IWP* and D_{eff}. The larger the discrepancy between the temperature assumed in light scattering calculations and the temperature within the cloud, the larger the bias in retrieved *IWP* and D_{eff}. While the addition of IR measurements can improve such retrievals, the relative improvement from this additional measurement does not wholly compensate for the bias introduced from assuming an unrepresentative temperature to calculate the scattering properties of ice particles. This is one indication that the cloud top height should also be retrieved. An information content analysis further demonstrated the benefits of combining sub-mm and IR measurements, and provided a better understanding of the magnitude and location (i.e., where in the parameter space) of improvements from adding IR. We also demonstrated that sensitivity of the refractive index to temperature primarily manifests in retrieval bias when the two assumed temperature differences become significant.

5.2. Ice particle shape

A fundamental assumption in ice cloud remote sensing is the ice particle shape, or habit. Early studies assumed ice particles to be spherical, primarily due to the ease in computing the scattering properties (i.e., Mie theory). Since then, significant advancements have been made in calculating single scattering properties (light scattering

calculations). Such advancements include the improved geometric optics method (IGOM; Yang and Liou, 1996) and the Invariant Imbedding T-Matrix (II-TM) method (Bi and Yang, 2014). For the sub-mm frequencies considered in this work, the size parameter is sufficiently small such that the II-TM is suitable for all realistic particle sizes and the IGOM is applied only for large particles at high frequencies (Ding et al., 2017).

In this section, we investigate how particle shape influences particle single-scattering properties and the subsequent impact of assuming a particular shape in remote sensing applications of ice cloud properties. Although the shape impact should be greater for visible and near infrared channels, where single scattering albedos could result in significant multiple scattering, it is important to understand these impacts for microwave channels as well. To this end, we select several different ice particle models, including an aggregate of severely roughened hexagonal columns as used in the MODerate Resolution Imaging Spectroradiometer (MODIS) Collection 6 cloud products (MC6), an aggregate of smooth hexagonal columns, a single plate, and a single hexagonal column. Depictions of the particles are provided in Fig. 5.11. For this analysis we only utilize the two highest frequency sub-mm channels, 640 and 874 GHz, as well as one IR channel at 12 μm. The *IWP* and D_{eff} are varied within clouds while other cloud characteristics such as the cloud top height (10 km), geometric thickness (1 km), and particle size distribution (gamma with effective variance of 0.1) are kept constant. For this analysis we pose the following scientific questions:

1. What is the bias of retrieved *IWP* and D_{eff} in sub-mm bands due to assumed ice particle habit?
2. How does that bias change when IR bands are incorporated into the retrieval?
3. What additional information can be gained from adding polarization measurements?

Figure 5.11: Illustration of the four ice particle habits used in the shape sensitivity study. Shown is an aggregate of severely roughened hexagonal columns (top left), aggregate of smooth hexagonal columns (top right), plate (bottom left), and single hexagonal column (bottom right).

5.2.1. Impact of particle shape on retrievals

The experimental setup of this analysis is as follows. All synthetic data is generated assuming the MC6 ice particle. We then perform separate retrievals, each assuming one of the four available habits shown in Fig. 5.11. Furthermore, two separate cases are considered. Since ice particles scatter sub-mm radiation more efficiently than IR radiation, we first investigate the impact of particle shape on retrievals of *IWP* and D_{eff} using only sub-mm measurements. In the second case, we include IR measurements and compare with sub-mm only retrievals to glean further insight to the value added from IR measurements. Since the focus of this analysis is to understand the impact of

particle shape on sub-mm *TB*, and subsequently retrievals, we select the MC6 particle for generating all IR synthetic data and retrieval LUTs. In addition to the retrievals, we perform information content analyses utilizing the two metrics of information content used in Section 5.1, *DOF* and *SIC*. These information content analyses are again conducted for both *IWP* and D_{eff} over the entire parameter space.

Figure 5.12 shows the retrieval of *IWP* for the first scenario (sub-mm only case). As is evident from the figure, retrieved *IWP* agrees pretty well with the true *IWP* for all shapes considered. The MC6 particle (top left Fig. 5.12) provides the highest level of agreement in *IWP*, which is expected and serves as a control in this analysis since the MC6 particle is used to both generate synthetic data and compute the retrieval LUT. Interestingly, the single column performed better than the aggregate of smooth columns. The scale of surface roughness assumed in the MC6 particle is much less than these sub-mm wavelengths, and therefore have little impact on the scattering properties. However, the inclusion of surface roughness provides a noticeable difference in retrievals of *IWP*. It is also evident when looking at the RMS errors shown in Fig. 5.12 that *IWP* retrieved assuming a plate particle deviated the most from the control (top left Fig. 5.12).

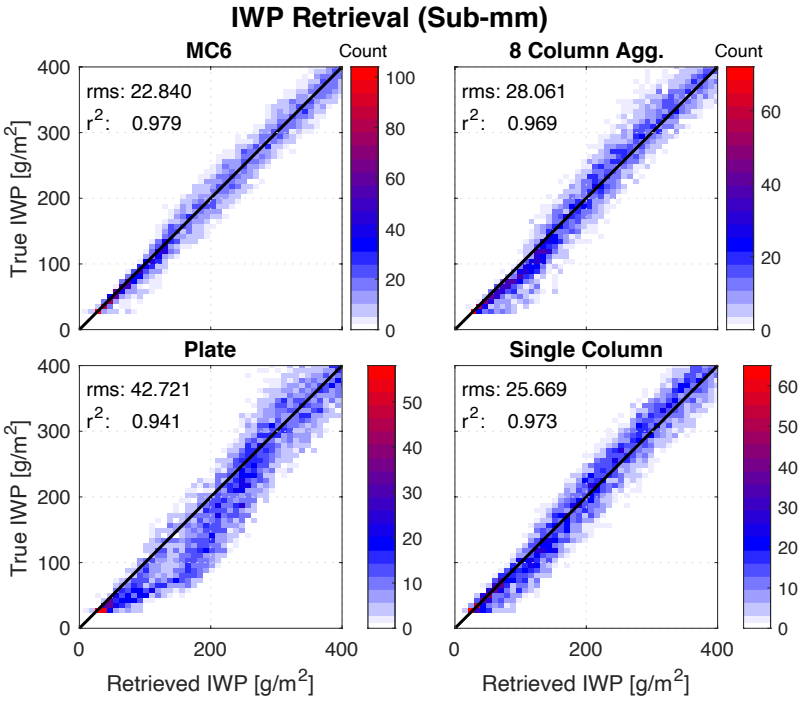

Figure 5.12: Retrieved *IWP* for all ice particle shapes considered, using only sub-mm measurements. Each of the four sub-panels correspond to a different ice particle habit, labeled at the top.

The results for retrieved D_{eff} are provided in Fig. 5.13. As expected, there is less agreement between the different particle shapes as for retrieved *IWP*. This is because the cloud induced radiance (ΔTB), or the difference between clear and cloudy *TB*, is proportional to the volume (mass) of ice. The plate particle again provides the largest bias or deviation from the control, as confirmed by the large RMS error. It is important note that retrieved D_{eff} deviates the most from the true value for moderate particle sizes (~75–150 μm) for all but the plate particle. This is because the response of ΔTB to these particle sizes is nearly quadratic, and therefore the solution to the inverse problem is multi-valued.

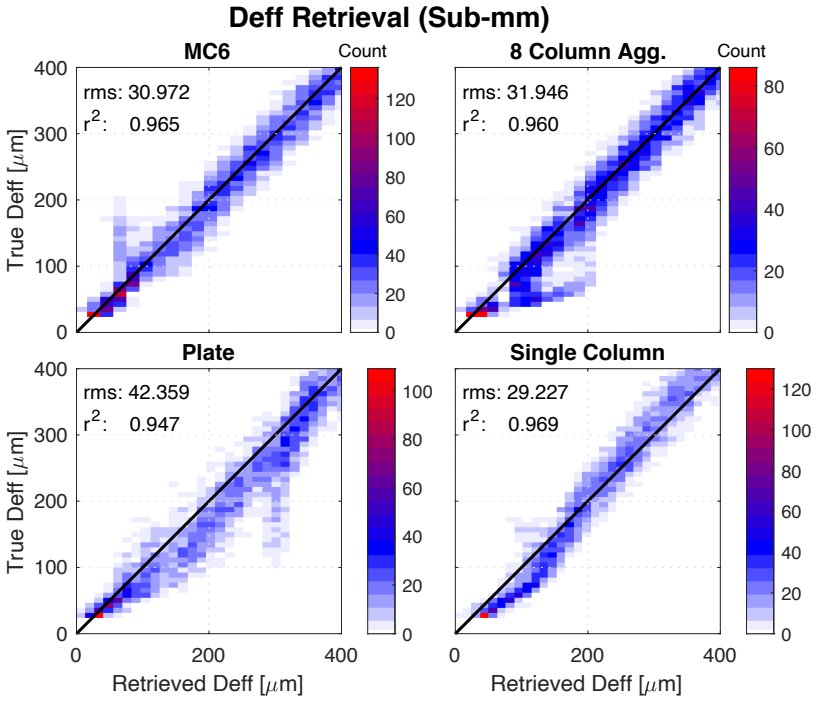

Figure 5.13: Same as Fig. 5.12, except D_{eff} is retrieved.

For the second scenario, the same sub-mm measurements are used (640 and 874 GHz) but a single IR measurement is included (12 μm). The results for retrieved *IWP* and D_{eff} are presented in Figs. 5.14 and 5.15, respectively. To reiterate, IR synthetic data and retrieval LUTs are both generated assuming the MC6 particle. When looking at the *IWP* retrievals in Fig. 5.14, it is again evident that *IWP* retrieved assuming the plate particle has the worst agreement with the true *IWP*. When comparing Fig. 5.14 to its counterpart without IR measurements (Fig. 5.12), the plate particle benefitted most from the addition of IR measurements. This is due to the differing shapes used to generate the sub-mm (plate) and IR (MC6) retrieval LUTs, while all synthetic data is generated assuming the MC6 particle. The takeaway here is that when combining measurements from two different spectral regimes, in this case sub-mm and IR, it is necessary that the

assumed habits be consistent (i.e., mass and volume). More simply, of the four particle shapes assumed two are bulky aggregates and two are single particles with differing aspect ratios, and retrievals of *IWP* when combining IR and sub-mm measurements should assume a consistent shape (i.e., both bulky particles or single particles with commensurate masses and volumes).

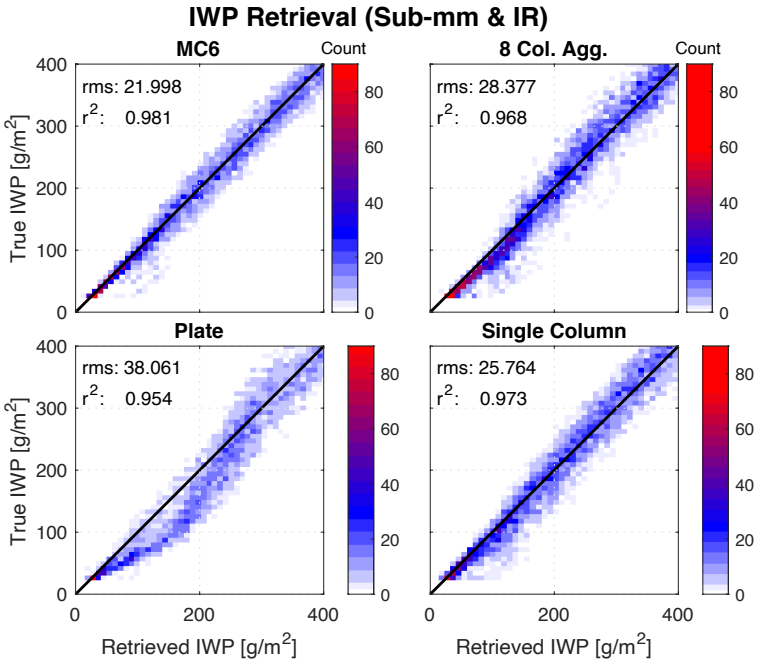

Figure 5.14: Retrieved *IWP* for all ice particle shapes considered, using sub-mm and IR measurements. Each of the four sub-panels correspond to a different ice particle habit, labeled at the top.

Figure 5.15 shows the retrieved D_{eff} for this scenario. The same bias in D_{eff} is seen for moderate sized ice particles (~75-150 μm), which is again due to the nonlinear response of sub-mm TB and ΔTB for these particle sizes. The fact that the addition of IR measurements does not abate the bias of retrieved D_{eff} for this particle size range means that there is insufficient information content provided by the IR measurements or the

degree of nonlinearity in sub-mm regime is too high to mitigate the issue of multi-valued solutions.

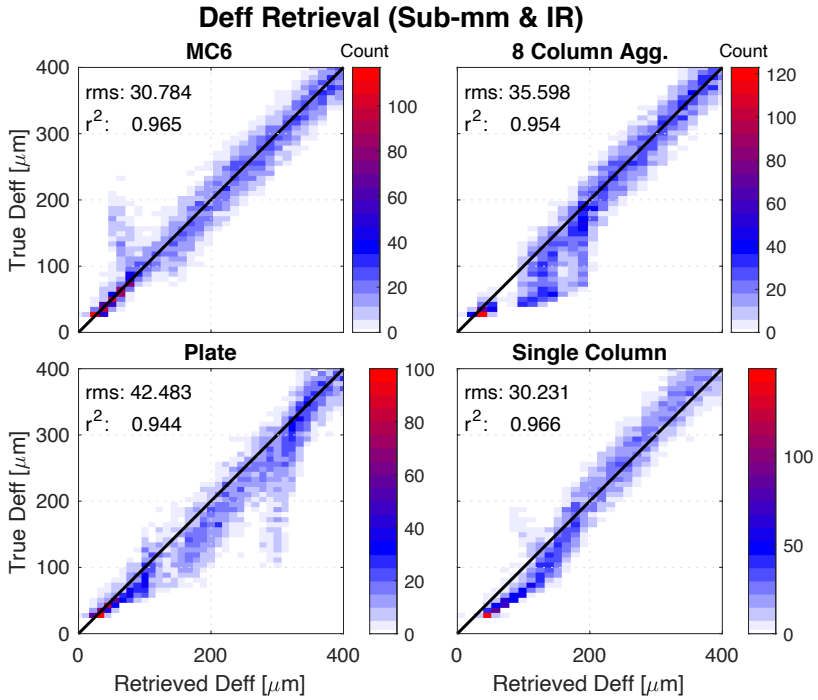

Figure 5.15: Same as Fig. 5.14, except D_{eff} is retrieved.

5.2.2. Particle shape and information content

In this section we investigate the information content provided in these sets of measurements for different particle habits. To do this, we compute *SIC* and *DOF* for discrete bins over the entire parameter space. For each bin, the retrieval is iterated 500 times and the mean *SIC* and *DOF* for all iterations is computed. *SIC* for the first (sub-mm only) and second (sub-mm and IR) scenarios is shown in Figs. 5.16 and 5.17, respectively. Considering Fig. 5.16, it is evident that *SIC* is smallest for all assumed particles when *IWP* and D_{eff} are both large. This is expected since the ΔTB signal saturates when *IWP* becomes large (i.e., attenuates within the cloud due to multiple

scattering). *SIC* is also small in some cases for optically thin clouds, when *IWP* and D_{eff} are small. In the case of optically thin clouds, ΔTB is small because there is little difference in the clear sky and cloud induced *TB*. Recall *SIC* is essential the measure of the relative improvements to our *a priori* knowledge that results from the addition of measurements. Therefore, it makes sense that *SIC* is smaller here for these sub-mm measurements because we are "asking" them to improve *a priori* knowledge of simply the radiative background (i.e., the water vapor profile). In addition, Fig. 5.16 shows that *SIC* varies little for the different shapes assumed here.

We draw similar conclusions when looking at *SIC* for the second scenario (Fig. 5.17). *SIC* again decreases towards zero when *IWP* and D_{eff} are large. However, comparing this figure to its counterpart from the first scenario (Fig. 5.16) it is evident that the magnitude of *SIC* increased throughout the parameter space, and particularly when *IWP* and D_{eff} are small. Taking the rationale for low *SIC* for sub-mm measurements in optically thin clouds a step further, it is straightforward to intuit that adding IR measurements provides the largest increase to *SIC* in the areas of low *IWP* and D_{eff} where they have the highest sensitivity.

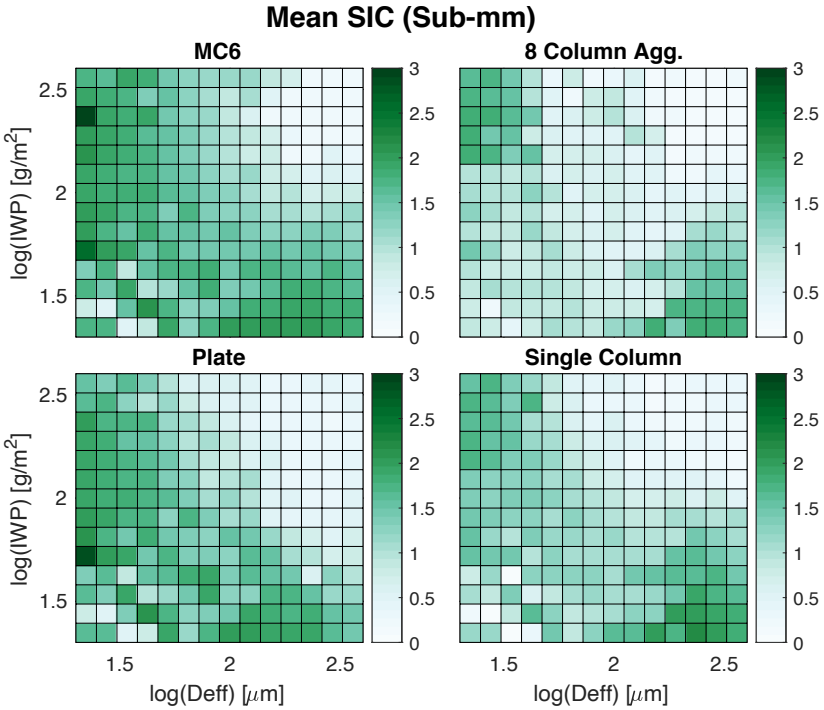

Figure 5.16: Mean *SIC* of retrievals for all ice particle shapes, using sub-mm measurements.

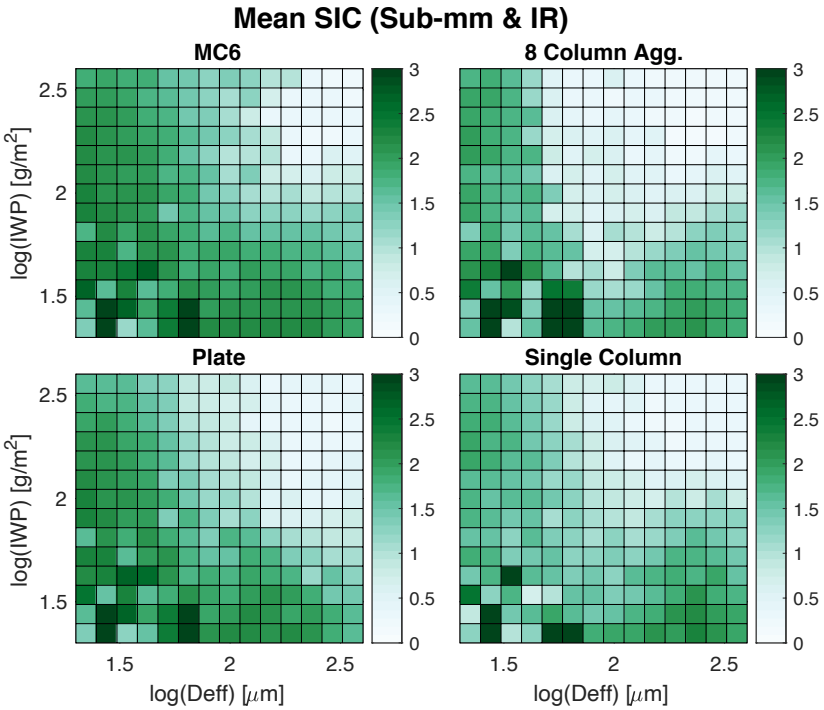

Figure 5.17: Mean *SIC* of retrievals for all ice particle shapes, using sub-mm and IR measurements.

To further address first two questions posed at the beginning of this section and understand the influence of assumed ice particle shape on sub-mm ice cloud property retrievals and the benefits of including IR measurements, we compute the *DOF* for all shapes. The *DOF* for the first (640 and 874 GHz) and second scenario (640, 874 GHz, 12 μm) are shown in Figs. 5.18 and 5.19, respectively. Recall that *DOF* is equivalent to the number of independent pieces of information from the measurements. When comparing the panels in Fig. 5.18, we again see that there is little to no information for optically thick clouds (large *IWP* and D_{eff}), and information is decreased for optically thin clouds (small *IWP* and D_{eff}). It is again the case that *DOF* does not vary significantly among the different particle shapes, but it is evident there is a loss of information in particular regions of the parameter space for different shapes.

Now let us compare Figs. 5.18 and 5.19 which correspond to the two scenarios. The most obvious takeaway is that adding IR measurements increased the information content for all shapes, particularly for moderate *IWP* and D_{eff} values. As a technical reminder, the retrieval can still converge on a solution that is not "optimal", meaning the cost function converged, but to a larger value than what is prescribed for an "optimal" retrieval. This criterion is typically set to equal the number of elements, m, in the measurement vector. However, for this work we select a threshold for an optimal solution to be $2m$. Consequently, if the percent of pixels which provide an optimal solution in one bin is more than one standard deviation from the median value for the entire parameter space, we do not average the values of *DOF* or *SIC* in that pixel and is marked white.

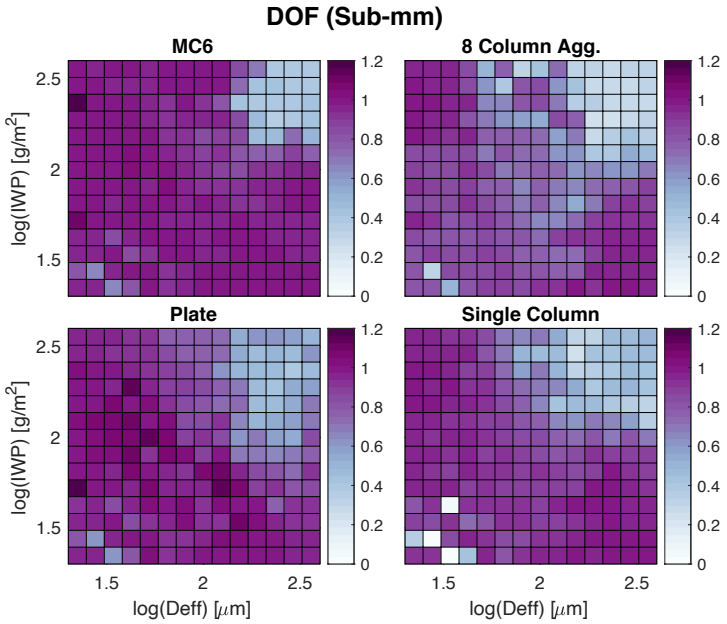

Figure 5.18: *DOF* of retrievals for all ice particle shapes, using sub-mm measurements.

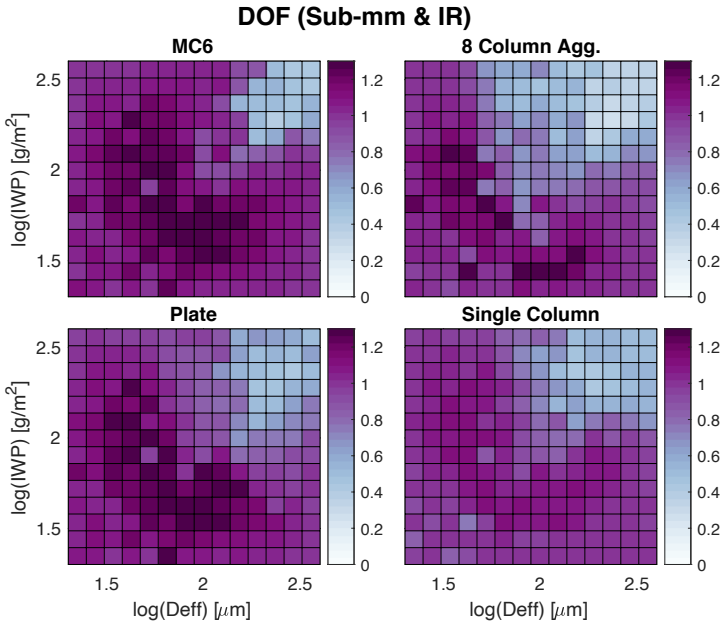

Figure 5.19: *DOF* of retrievals for all ice particle shapes, using sub-mm and IR measurements.

Lastly, we address the third scientific question posed and investigate what information could be gained from the addition of polarized measurements, and in

particular *PD*. To do this we again compute *SIC* and *DOF*, and the results are shown in Figs. 5.20 and 5.21, respectively. However, since the previous figures demonstrated an increase of information content from the addition of IR measurements, in this analysis we only consider the second scenario (640 and 874 GHz, 12 μm). Comparing the *SIC* with the addition of polarization (Fig. 5.20) to its counterpart without polarization (Fig. 5.17) it is evident that the magnitude of *SIC* is increased from a maximum of ~3 to ~8 when polarization is included. *SIC* increases the most for optically thin clouds, at least in the case of the control (MC6) and plate particle. When comparing the magnitude and distribution of *SIC* for the different particle shapes, note that the single column has the lowest *SIC* over the entire parameter space, but particularly in the case of optically thick clouds (large *IWP* and D_{eff}). However, when looking at the plate particle (bottom left of Fig. 5.20) we see that *SIC* is actually increased for the optically thick case. This points to the potential of using a mixture of habits, in this case an aggregate of columns and a single plate, in conjunction with polarized sub-mm and IR measurements to provide more information about particle size and IWP under optically thick cloud conditions.

The *DOF* for this scenario are shown in Fig. 5.21. Most notably, when comparing this figure to its counterpart without polarization (Fig. 5.19), we see that the magnitude of *DOF* increases from the addition of polarization. Recall from Chapter 4 that *DOF* is the number of independent pieces of information carried out by the measurements, and therefore ranges from zero to the number of elements in the state vector. When polarization is included, we now see *DOF* values that approach 2, which corresponds to full information. So, if the measurement error variance-covariance matrix

is diagonal (i.e., meaning no correlation between the measurements), one could think of each diagonal element of **A** (the averaging kernel matrix) to be the partial *DOF* corresponding to that state vector element. This figure shows the total *DOF*, but since some values are close to 2, that means there is almost full information on each parameter provided by the measurements. It is again interesting to note that compared to other particles or when polarization is not included, there is a noticeable increase of information for high *IWP* and D_{eff} when considering the plate particle. This further hints at the possibility of utilizing a mixture of particle shapes to increase information content throughout the entire parameter space.

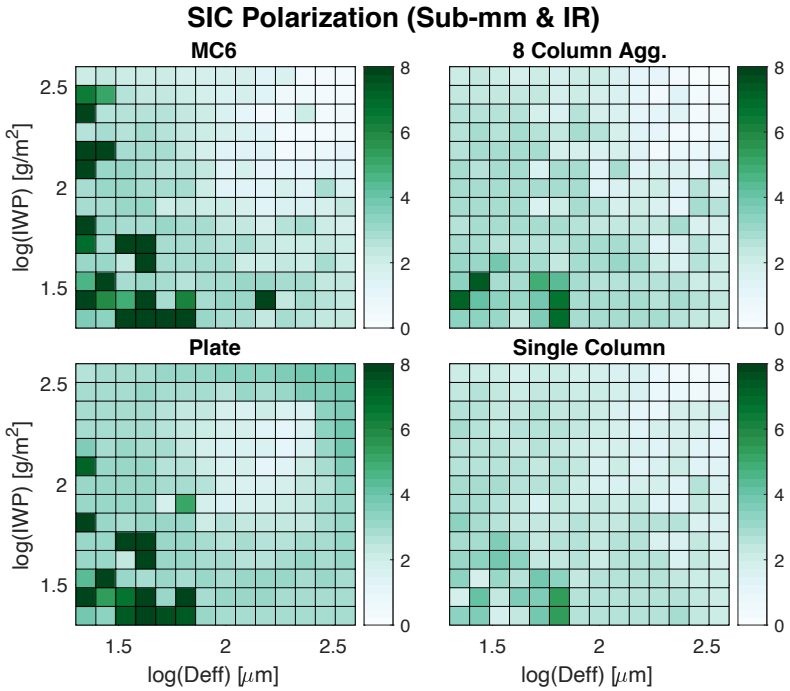

Figure 5.20: *SIC* of retrievals for all particle shapes, using polarized sub-mm and IR measurements.

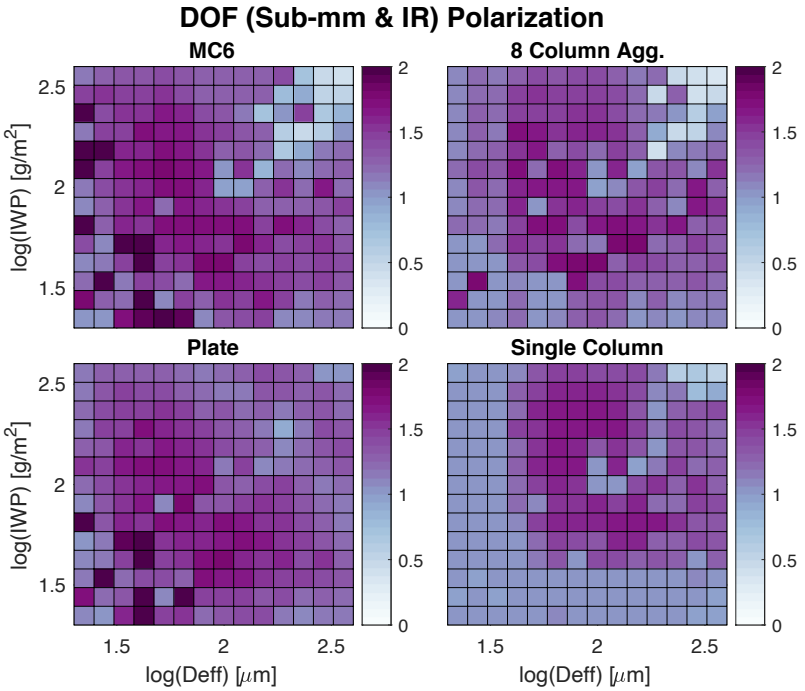

Figure 5.21: *DOF* of retrievals for all ice particle shapes, using polarized sub-mm and IR measurements.

5.2.3. Conclusions

To remotely sense ice cloud properties, it is necessary to assume a particular ice particle habit (shape) for the purpose of light scattering and radiative transfer calculations. Analyses presented in this section are conducted to better our understanding of how assuming a specific particle shape to represent natural ice particles biases sub-mm retrievals of *IWP* and D_{eff}, how the addition of IR measurements may improve such a bias, and lastly what information might be gained from adding polarized measurements (*PD*). Polarized and un-polarized *TBs* are synthesized assuming an aggregate of severely roughened hexagonal columns, which is consistent with the one employed for MODIS Collection 6 (MC6) ice cloud products. We perform retrievals with LUTs considering four different particle shape models: the MC6 particle (as a

control), an aggregate of smooth hexagonal columns, a single plate, and a single hexagonal column. The scattering phase functions for the two aggregate particles are very similar, so we do not expect a significant difference between these two particles. However, both the single plate and column particles have phase functions such that the scattered intensity is smaller for these particles, particularly in the side and backscattering directions. Therefore, we expect significant differences between the single particles and bulky aggregate particles.

The root mean square (RMS) errors of retrieved *IWP* and D_{eff} for the control particle (MC6) as well RMS differences between the control and that corresponding to a particular particle are presented in Table 5.1. As shown in the table, sub-mm only retrievals of *IWP* deviated little from the control case when the aggregate of smooth columns or single hexagonal column is assumed. However, the RMS of *IWP* when assuming a plate particle is considerably larger. Similar results are seen for sub-mm only retrievals of D_{eff}, with exception of the single column particle which actually had a slightly lower RMS than the control particle. The RMS of *IWP* and D_{eff} for the control particle decrease slightly when IR measurements are added. However, with the exception of the single plate particle, RMS actually increased for all other particles. Overall, the single plate particle provided again provided largest difference between true and retrieved *IWP* and D_{eff} values. As a reminder, because the primary goal of this is to understand the impact of particle shape on sub-mm *TBs*, and subsequently ice cloud property retrievals, the shape assumed for all IR synthetic data and retrieval LUTs is the control (MC6) particle. Overall, the retrievals presented in this section show that there is

a nonnegligible bias of retrieved *IWP* and D_{eff} from the assumption of ice particle shape. Biases of retrieved *IWP* were larger than those for D_{eff}, and in both cases the bias is the largest when a single plate particle is assumed. An additional takeaway from the retrievals presented in section 5.2.1 is that when combining measurements from two different spectral regimes, in this case sub-mm and IR, it is necessary that the assumed habits be consistent (i.e., in mass and volume).

Table 5.1: *Error of retrieved IWP and D_{eff} from assuming different ice particle shape models. The RMS for the control (MC6) particle is provided and RMS associated with the other particle models is reported as the difference from the control. Sub-mm frequencies include 640 and 874 GHz, and IR wavelength is 12 μm.*

	Sub-mm		**Sub-mm & IR**	
Habit Type	*IWP* (g/m^2)	D_{eff} (μm)	*IWP* (g/m^2)	D_{eff} (μm)
MC6 (control)	22.84	30.97	22.00	30.78
Smooth Column Agg.	+5.22	+0.97	+6.38	+4.81
Single Plate	+19.88	+11.39	+16.06	+11.70
Single Column	+2.83	-1.75	+3.77	-0.55

In addition to quantifying how assumed ice particle shape impacts ice cloud property retrievals, we explored the influence of shape on the information content provided in the measurements. There is a less noticeable difference in the two metrics of information content utilized here (*SIC* and *DOF*) among the assumed habits than is demonstrated in the retrievals. However, when comparing the two scenarios (sub-mm only, sub-mm and IR), it is evident that there is a significant increase in both *DOF* and *SIC* from the addition of IR measurements. This is particularly the case for moderate *IWP* and D_{eff} values, where IR measurements are sensitive. These results further

demonstrate the benefit of combining IR and sub-mm measurements for the retrieval of ice cloud properties.

Lastly, we investigated the benefit (in terms of information content) from adding polarization measurements to the retrieval. The addition of polarization increased the maximum magnitude of *SIC* from ~3 to 8. Among the different particle shapes assumed, the single column had the lowest *SIC* and *DOF*. However, when considering the plate particle, information content is increased compared to all other cases (even the control) for optically thick clouds (large *IWP* and D_{eff}). The maximum magnitude of *DOF* increased from ~1.3 in the case of no polarization to ~2 when polarization is added. Because there are two parameters being retrieved in these analyses, the theoretical maximum *DOF* attainable is 2. Therefore, for optically thin clouds (low *IWP* and D_{eff}) where *DOF* approaches 2, the addition of polarization means that there is almost full information on each parameter provided by the measurements. Just as with *SIC*, assuming a plate particle in the retrieval increases the *DOF* for optically thick clouds, an area of the parameter space where little to no information is seen in all other cases. The principal takeaway from these results is that it may be useful to employ a mixture of particle shape models, particularly a bulky (aggregate) and single particle shape model, in conjunction with polarized sub-mm and IR measurements to increase the information content for optically thick clouds, which sub-mm and IR otherwise demonstrate little to no sensitivity.

As a caveat, the analyses in this section are performed assuming the ice particle is completely randomly oriented in space. Therefore, these results do not necessarily

extend to the case in which the particle has some preferential orientation. The impact of particle shape on its single scattering properties, and subsequently the retrieval of ice cloud properties, is expected to be larger when some preferential orientation is assumed. This is especially true when polarization is necessary. Further investigation of how assuming a particular particle orientation influences polarized and unpolarized *TB* is presented in Chapter 6.

6. SUB-MM POLARIZATION SIGNALS OF ICE CLOUDS

Recall from Chapter 3, the polarization of electromagnetic radiation can be described by the Stokes parameters. From these parameters, one can compute brightness temperatures at two orthogonal polarization states (vertical and horizontal), as well as the difference between the two, or the polarization difference (*PD*). Physically, *PD* is induced by different scattering efficiencies of ice particles at these two different polarization states. Therefore, *PD* can provide rich information on ice cloud microphysical properties, such as particle size, shape and orientation. In Chapter 5, we discussed how particle shape impacts sub-mm *TB* and *PD* in terms of ice cloud property retrievals and information content. This chapter builds on the previous discussions of polarization and aims to provide a more holistic understanding of ice cloud polarizations in the sub-mm spectral region. In Section 6.1 we present further investigation of the value added by polarized measurements to retrievals of ice cloud microphysical properties and comment on the practical difficulties of incorporating *PD* in such retrievals. The impacts of particle orientation on sub-mm *TB* and *PD*, particularly for horizontally oriented particles is provided in Section 6.2. In Section 6.3 we investigate polarization signals for mixtures of randomly and horizontally oriented particles, as well as the potential to infer the fraction of oriented particles from polarized measurements.

6.1. Impact of polarization on ice cloud property retrievals

This section further explores the benefits of measured ice cloud polarization signatures to infer ice cloud properties. We also discuss the difficulties associated with

implementing sub-mm polarization measurements. To this end, we pose the following scientific questions:

1. How does the addition of polarimetric measurements improve sub-mm retrievals of ice cloud microphysical properties, such as D_{eff}?
2. What subsets of frequencies provides the most benefit, particularly in terms of D_{eff}?
3. Does the ratio of polarization difference at different bands provide additional useful information?

For these simulations we assume a single layer ice cloud from 9 to 11 km comprising randomly oriented aggregates of severely roughened hexagonal columns, and an *IWP* of 100 g/m^2. With these assumptions we compute *PD* for various sub-mm and infrared combinations, which is provided in Figure 6.1. Before discussing the values in Fig 6.1, it is important to further discuss the origin of polarization signals. When ice particles exhibit no preferential orientation (randomly oriented), polarization signals arise from radiation which is scattered into the line of sight. Recall that in this case only the phase matrix contains non-zero off-diagonal elements. Therefore, in the case of positive *PD*, the scattering efficiency at vertically polarized radiation is larger than its horizontal counterpart. Now returning to Fig. 6.1, it is evident that for the sub-mm channels *PD* increases rapidly as D_{eff} increases until reaching a maximum at some critical D_{eff}, then decreases towards zero. This is because as particles become larger multiple scattering begins to dominate, and there is less vertically polarized radiation scattered into the line of sight. It is also important to note that this critical D_{eff} is different

for all three sub-mm channels and becomes larger as frequency decreases. Because the opacity is greater at higher frequencies which are more sensitive to smaller particles, *PD* begins to decrease at smaller particle sizes for higher frequencies (e.g., ~65 μm at 874 GHz and ~95 μm at 640 GHz).

An important takeaway from Fig. 6.1 in terms of ice cloud property retrievals is that most of the sub-mm channels exhibit significant sensitivity to D_{eff}, and the *PD* at several closely spaced channels could be useful for its retrieval. However, there is an issue of multivalued solutions that must be cautiously navigated, meaning that two different particle sizes can produce the same *PD*. One way to mitigate this dilemma is to add additional measurements. For example, the ratio of *PD* at a window channel (640 GHz) and water vapor absorption line (325 GHz) monotonically decreases as D_{eff} increases. Although it quickly approaches zero, the high sensitivity lends confidence to its ability to retrieve D_{eff}, particularly for D_{eff} less than ~100 μm. Conversely, *PD* at 12 μm monotonically increases with increasing D_{eff}. The prevailing consensus is that it is not necessary to consider polarization for IR measurements. However, based on Fig. 6.1 (and further discussions below), we argue that including IR *PD* can provide useful information to constrain D_{eff} retrievals, particularly for large particles where sub-mm sensitivity is low.

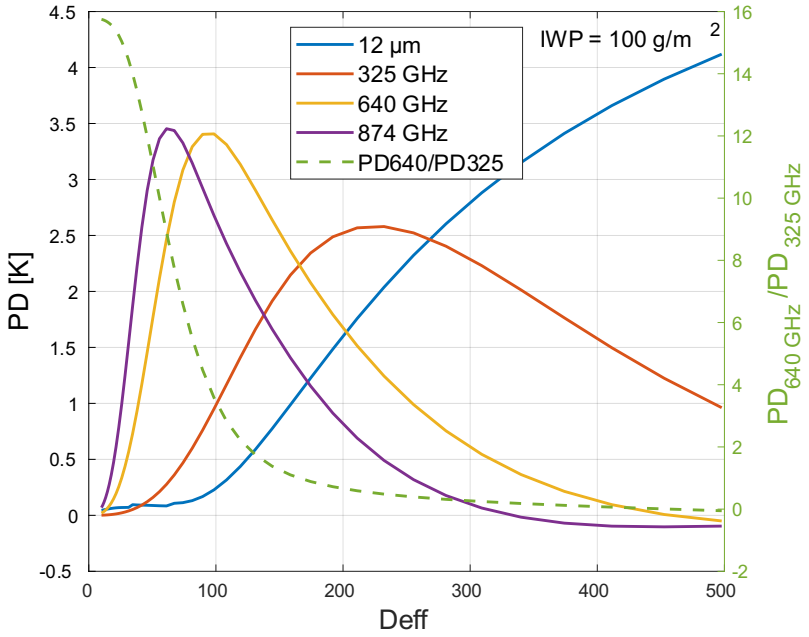

Figure 6.1: *PD* sensitivity to D_{eff} for sub-mm and IR channels when *IWP* = 100 g/m^2. Colored lines denote different measurement bands, and the dashed line denotes the ratio of *PD* at two sub-mm frequencies (640 and 325 GHz).

In Chapter 5, we demonstrated how information content, such as *DOF* and *SIC*, is increased by adding polarization measurements. As a next step, utilize the measurements shown in Fig. 6.1 to determine which frequency, or set of frequencies, improves retrievals of D_{eff}. The results of these retrievals are presented in Fig. 6.2. As a benchmark to compare against other retrievals, we retrieve D_{eff} using *TBs* at 640 GHz, 874 GHz, and 12µm without considering polarization (top left panel of Fig. 6.2). The remaining retrievals all consider polarization, such as is shown the upper right panel which includes *PD* at 640, 874 GHz, and 12µm. An additional sub-mm channel is added in the bottom left panel (325, 640, 874 GHz; 12 µm). Finally, in the bottom right panel we include the ratio of two sub-mm *PDs* (325, 640, 874, 640/325 GHz; 12 µm). Note

that all retrievals shown also use *TBs*, or more precisely ΔTB, and are supplemented with *PD* (i.e., the measurement vector contains both *TB* and *PD* for a given frequency). In these simulations we again assume the particle shape model is an aggregate of roughened hexagonal columns following a gamma particle size distribution.

As is evident from the RMS errors, Fig. 6.2 demonstrates the relative improvement of retrieved D_{eff} from the addition of polarization. For example, the top left panel in which polarization is not considered exhibits poor consistency between retrieved and true D_{eff} for mid-sized particles (~125-325 μm), producing an RMS of ~42.48 μm. The top right panel utilizes the same channels but considers polarization for all three. You can see from this panel that the addition of polarization reduces the RMS to 35.60 μm and improves retrieval performance for D_{eff} greater than ~200 μm. However, retrieval performance decreased for particles less than this size. This is due to the multi-valued nature of the problem when considering *PD*. This is further clarified by looking at Fig. 6.1, which shows for example that a *PD* of 2.5 K corresponds to two different D_{eff} values for both 640 and 874 GHz. It is straightforward to imagine that the two D_{eff} values which correspond to a *PD* of 2.5 K represent two different minimums in the cost function. Therefore, it is possible the retrieval becomes trapped in one of these minimums, eventually converging on a solution which corresponds to a local minimum and not a global minimum, which corresponds to the true value. This is evident in the retrievals. For example, when the true D_{eff} is 50 μm, some retrieved values are as large as 100-150 μm. This indicates that the retrieval was trapped and ultimately converged on

the solution corresponding to the right side of the *PD* peak in Fig. 6.1, when the true solution is on the opposite side.

As a first attempt to mitigate this issue, we include an additional sub-mm channel at 325 GHz and the results are in the bottom left panel of Fig. 6.2. In this case the RMS has again decreased and is now roughly 30.8 μm. Also note that compared to the top right panel where retrieved D_{eff} often overestimates the true value, the opposite is now true. Finally, we add the ratio of *PD* at two channels (640, 325 GHz) and the results are shown in the bottom left panel of Fig. 6.2. Looking at this panel we see that the RMS has again decreased slightly to ~30.2 μm, and less underestimation of the true D_{eff} is present than was the case for the previous panel. For the simulations presented in this section, there is not a considerable difference between these final two retrievals. If in fact, there is only a nominal improvement in all cases provided by the additional measurement in the last panel (640/325 GHz), then the most sensible choice for a retrieval would be the one corresponding to the bottom left panel, even though the final retrieval includes a ratio of existing channels and needs no new measurements (i.e., 448 GHz). This is simply because the Optimal Estimation framework used in these retrievals requires inversions of matrices, and a larger measurement vector equates to a higher computational demand to compute the inverse of these matrices.

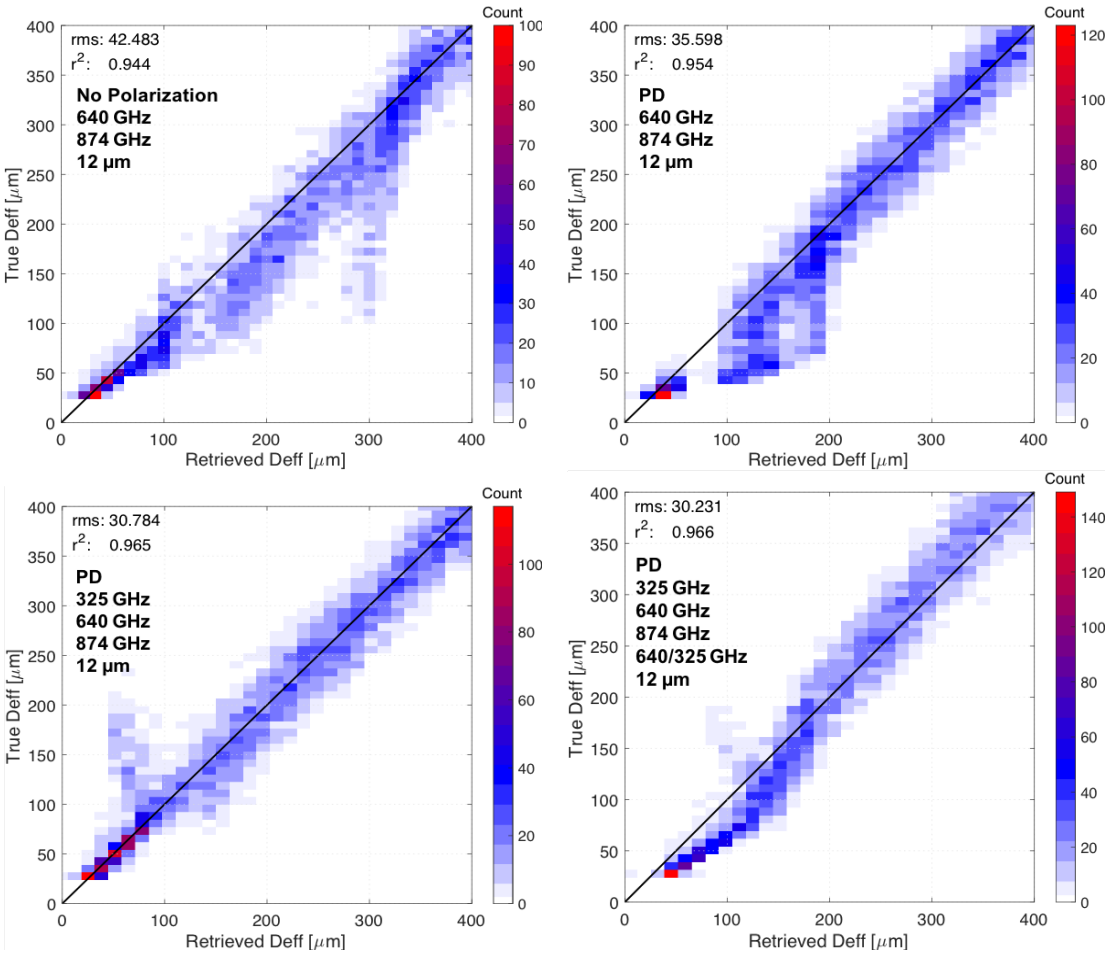

Figure 6.2: Retrieved D_{eff} using four different polarized sub-mm and IR measurement combinations. Top left: 640, 874 GHz, and 12 µm (no polarization), Top right: *PD* (640GHz, 874 GHz; 12 µm), Bottom left: *PD* (325, 640, 874 GHz; 12 µm), Bottom right: *PD* (325, 640, 874, 640/325 GHz; 12 µm).

While there is rich information content present in polarized measurements, this section highlights the practical difficulties of incorporating *PD* in retrievals, such as the issue of multivalued solutions. Figure 6.2 demonstrates the relative improvement of adding polarization to retrieve $D_{eff,}$ with the configuration in the bottom right panel producing overall the closest agreement between real and retrieved values. However, further simulations are necessary to test the accuracy of this configuration in retrievals of

both D_{eff} and *IWP* over a wider range of atmospheric and cloud conditions. A sample of some such simulations is presented in Chapter 7. It is important to reiterate that polarization is influenced by cloud microphysical properties, such as particle composition, shape, and orientation. In Chapter 5 we investigated the consequences, in terms of cloud property retrievals and information content, of assuming a particular particle shape model to represent natural ice particles. In this section we build on that analysis and present essentially a simple channel selection study based on the relative improvement of incorporating polarized measurements in cloud property retrievals. However, these results only apply to clouds in which ice particles are randomly oriented. Ignoring orientation can negatively bias vertically polarized observations and positively bias horizontally polarized observations. A further analysis how particle orientation impacts polarization is provided in the next section.

6.2. Impacts of particle orientation on *TB* and *PD*

For the previous analyses in this chapter, we assume ice particles to be completely randomly oriented in space, which is a common assumption in ice cloud remote sensing. However, studies have demonstrated that ice particles do not necessarily possess a random orientation. Gong and Wu (2017) used measurements from the spaceborne Global Precipitation Measurement (GPM) Microwave Imager (GMI) to show that polarized microwave scattering signals attributed to ice clouds can be explained by the non-sphericity and orientation of the particles. A study by Zeng et al. (2018) also used polarized measurements from GMI (at 166 GHz) to analyze the distribution of ice particle orientation in optically thick ice clouds. Zeng et al. (2018)

used *PD* to indicate the general orientation of ice particles, with positive *PD* values suggesting horizontally oriented particles and the magnitude of *PD* directly proportional to the percentage of horizontally oriented ice particles. In this study they concluded that horizontally oriented ice particles in thick clouds are common from the tropics to high latitude. Therefore, when incorporating polarized sub-mm measurements in ice cloud property retrievals it is essential to understand how the orientation of non-spherical ice particles influences polarization. It is important here to note that we currently have no instrument or method capable of determining the particle shape and orientation, and therefore results presented in this section are strictly indicative of the error stemming from assuming a randomly oriented particle.

To understand the errors of sub-mm *TB* and *PD* which result from the assumption that non-spherical ice particles be randomly oriented, we simulate *TBs* and *PDs* associated with random and azimuthal orientations. As a point of clarification, when particles are said to be preferentially or azimuthally oriented, we assume that the particles are randomly oriented in the azimuth. While it is possible that certain particles under the influence of electrostatic forces or wind shear can possess a systematic azimuthal alignment, this situation is not considered in this study. Ice particle scattering properties delineate the interaction between the particles and electromagnetic radiation, and therefore these properties directly affect simulations and retrievals of sub-mm and IR observations of ice clouds. This reduces the amount of information which can be retrieved from observations, and consequently full exploitation of polarization signals in retrievals requires scattering properties of oriented particles. Therefore, for these

simulations we utilize the single scattering property database for azimuthally oriented particles, as outlined in Brath et al. (2020), which includes scattering properties for two particle shapes, a hexagonal plate and an aggregate of plates. The shapes are indicated in Fig. 6.3.

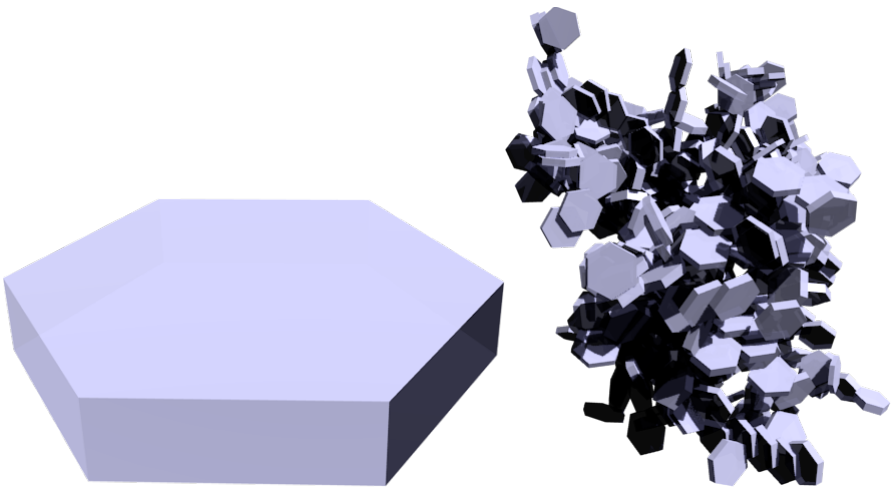

Figure 6.3: Illustration of the ice particle models used in the particle orientation analysis. On the left is a hexagonal plate and an aggregate of hexagonal plates is shown on the right. Adapted from Brath et al., 2020.

The Brath database also provides scattering properties of these particles for varying tilt (or canting) angles, which corresponds to azimuthally oriented particles with a specific orientation to the horizon (Brath et al., 2020). A graphical representation of basic horizontal and tilted orientations is provided in Fig. 6.4. Specific details of how scattering properties for oriented particles are calculated is beyond the scope of this work. The reader is directed to Brath et al. (2020) for such details.

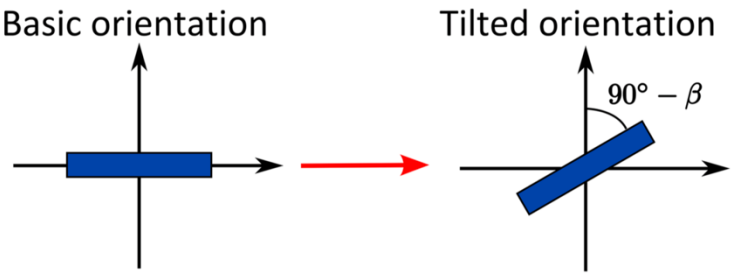

Figure 6.4: Graphical representation of azimuthal orientation and tilt angle $\boldsymbol{\beta}$. Adapted from Brath et al., 2020.

In order to isolate how the orientation of these two assumed particle shapes impacts polarized sub-mm *TBs*, we make a simple assumption that all particles in the cloud are the same size (i.e., monodisperse distribution). This removes any possible influence on the calculations from a particular particle size distribution. Under this monodisperse assumption, the particle number density (*PND*) within the cloud is given as,

$$PND = \frac{3IWC}{4\pi\rho r^3}, \tag{6.1}$$

where *IWC* is the ice water content, or mass density of ice within the cloud, ρ is the density of pure ice (taken as 917 kg/m^3), and r is the equal volume sphere radius of the particle. Assuming a monodisperse *PSD*, a viewing zenith angle of 53.5˚, and a 2 km thick ice cloud from 9 to 11 km, we compute *TB* for both *V* and *H* polarizations at two sub-mm frequencies (670, 886 GHz). Note that these frequencies differ slightly from those used previously (640, 874 GHz), and are selected because these are frequencies at which the single scattering properties explicitly calculated. Calculating *TB* at 640 and 874 GHz would require interpolation of the single scattering property database to these frequencies, and therefore to avoid the possibility of interpolation errors influencing the

results, 670 and 886 GHz are selected. Given the size of the scattering database, this also significantly reduces computational burden.

Figure 6.5 shows *PD* and *TB* as a function of volume equivalent diameter (D_{veq}) at 670 (top panel) and 886 GHz (bottom panel) when assuming a randomly oriented single plate shape. Each colored line denotes a different *IWP*, ranging from 50 to 400 g/m^2. Looking at Fig. 6.5 it is evident the *PD* curves exhibit a similar bell shape as is shown in Fig. 6.1. For smaller particles, *PD* increases with increasing *IWP* until you a critical particle size (e.g., ~175 μm at 670 GHz). Once particles become larger than this size, multiple scattering dominates, and the *PD* signal saturates and eventually decreases. Again, note that *PD* reaches a maximum value at smaller particle sizes for 886 GHz than at 670 GHz, because multiple scattering starts to occur at smaller particles for higher frequencies. As previously mentioned, sub-mm *TB* (or ΔTB) is proportional to *IWP*, at least up to a certain *IWP* value at which the signal is saturated. This is further evident when looking at the right column of Fig. 6.5. For example, in the top right panel, *TB* at 200 μm decreases at roughly the same rate as *IWP* doubles. Looking at 886 GHz (bottom right of Fig. 6.5), it is apparent that for a 200 μm particle the *TB* difference from *IWP* of 200 to 400 g/m^2 is much less than the difference between 100 and 200 g/m^2. This is indicative of increased multiple scattering, and consequently higher extinction of sub-mm radiation within the cloud.

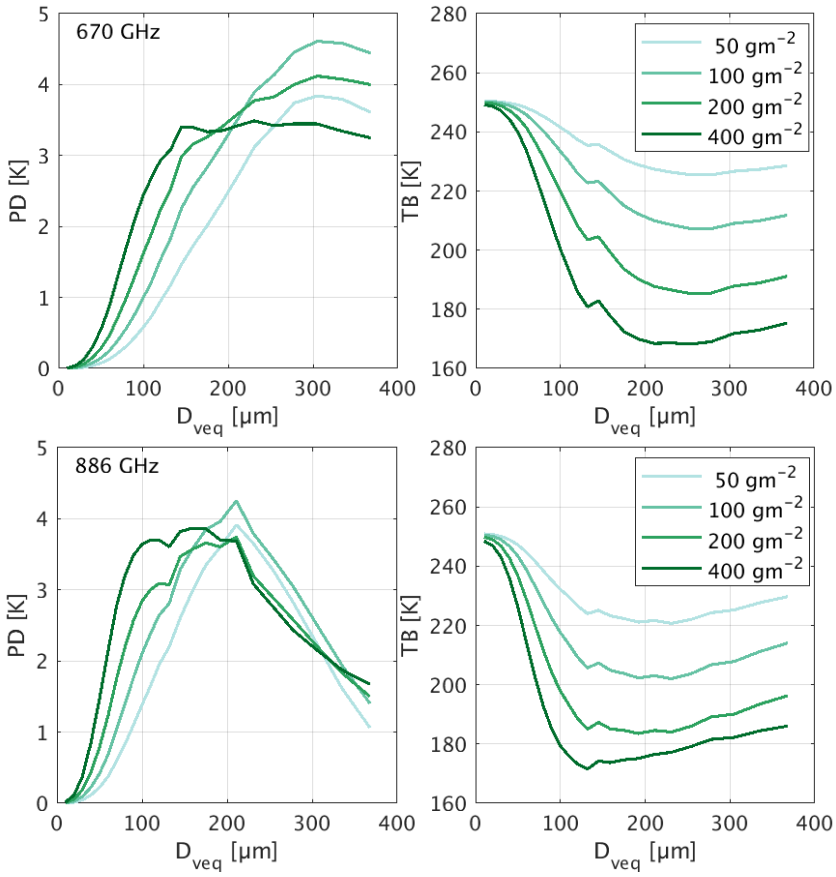

Figure 6.5: *PD* and *TB* sensitivity to particle size, assuming randomly oriented ice particles. The top (bottom) row corresponds to 670 (886) GHz. A randomly oriented single hexagonal plate is the assumed particle shape. Each line corresponds to a specific *IWP*, becoming darker as *IWP* increases.

Now that we have some understanding how *PD* and *TB* vary with particle size and *IWP* when assuming a randomly oriented hexagonal plate particle, we run the same simulation considering an azimuthally oriented particle with no titling angle ($\beta = 0$). These results are shown in Fig. 6.6. The first thing to note is the magnitude of the polarization signal is well over an order of larger. The maximum *PD* at both frequencies when assuming a randomly oriented particle ranges from 3.4 to 6.5 K depending on *IWP* and particle size. Under the assumption of an azimuthally oriented plate, we now see *PD*

values of over 100 K (at 664 GHz). This is a significant enhancement of the polarization signal, and therefore I think it is an important aside to consider what it means to have a positive *PD* and how we can then physically relate this to particle orientation. First, since we define *PD* as the difference between vertical and horizontally polarization states, a large positive *PD* indicates that vertically polarized *TB* is significantly larger than its horizontal counterpart. As discussed in the previous section, when particles are randomly oriented, the polarization signal results from radiation which is scattered into the line of sight. Let us now consider the impact of extinction on the polarization signal.

Attenuation of radiation by a particle can impact both the intensity and polarization state of the light. For azimuthally oriented particles, the sign of *PD* is influenced by two competing mechanisms. One such mechanism is dichroism, which is this precisely the situation described above where the particle attenuates radiation at different polarization directions differently. This is manifested by a non-diagonal extinction matrix. The other mechanism as mentioned above is radiation which is scattered into the line of sight. For downward looking simulations, as those presented here in which the scattering objects are between the sensor and the primary radiation source, dichroism is predominately the reason for the large positive *PD* values. More precisely, this partial vertical polarization is the result of a positive *Q* component of the Stokes vector, or the difference in the vertical and horizontal intensity components. As a caveat, the *PD* values shown in Fig. 6.6 are larger than what is expected from actual spaceborne observations. This is because assumptions made here, such as a

monodisperse size distribution and that every particle in the cloud is azimuthally orientated, are not representative of naturally occurring cloud conditions.

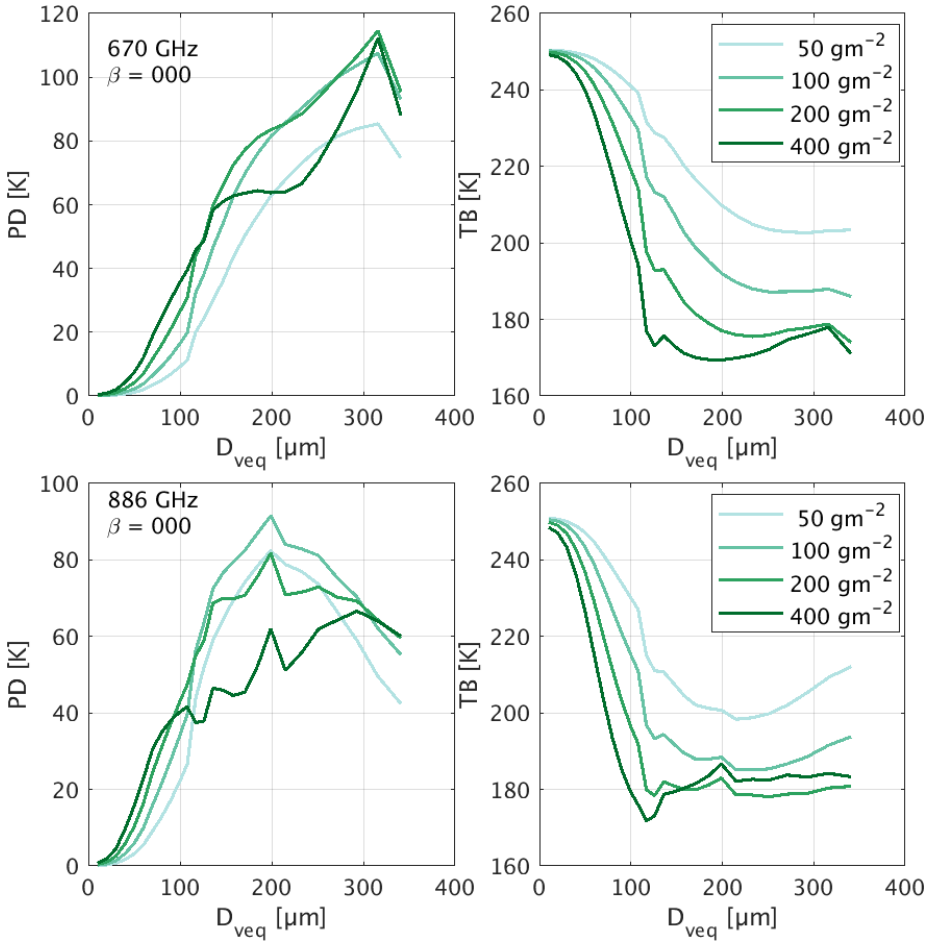

Figure 6.6: *PD* and *TB* sensitivity to particle size, assuming azimuthally oriented ice particles with tilt angle of $\beta = 0^{\circ}$.

Although *PD* has significantly increased as a result of the particle's horizontal orientation (for the reasons mentioned above) the change in *TB* is significantly smaller, which can be seen by comparing the right columns of Figs. 6.5 and 6.6. However, note there is now much less sensitivity of *TB* to *IWP*, particularly as *IWP* gets larger than 100

g/m^2. For the largest *IWP* considered (400 g/m^2), we now see *TB* start to increase at roughly 250 and 120 μm for 670 and 886 GHz, respectively. The interpretation of this behavior is as follows. As *IWP* or particle size increases, we expect an enhancement of the scattering effect, which results from an increase in particle number density or scattering efficiencies. Once particle sizes and *IWP* become large enough, the optical depth of the cloud increases and the multiple scattering effect dominates, and it is possible multiple scattering increases stochasticity in the scattering process. Furthermore, because the opacity is larger for high frequency channels which are more sensitive to smaller *IWP* and particle sizes, we see *PD* (*TB*) begin to decrease (increase) at smaller particle sizes and *IWPs* at 886 GHz compared to 670 GHz.

The results shown in Fig. 6.6 assume an azimuthally oriented particle with no tilting or canting angle ($\beta = 0^{\circ}$). Generally speaking, scattering data of azimuthally randomly oriented particles depends on incidence angle as well as two scattering angles (Brath et al., 2020). Complexity is further increased by adding a tilt angle. To understand the impact of tilting on simulated *PD* and *TB*, we assume an azimuthally oriented particle with a tilt angle of 30˚. The results are provided in 6.7, and as expected the magnitude of *PD* is significantly less than when $\beta = 0^{\circ}$, but larger than in the case of total random orientation. To glean more insight, consider scattering properties, such as the extinction matrix *K*. Extinction of the difference between vertical and horizontal polarization is described by the K_{21} element of the matrix. As previously mentioned, when a particle is randomly oriented K_{21} is zero. However, in the case of an azimuthally oriented particle, this element exhibits a significant dependence on tilt angle (as well as

incidence angle). The magnitude of K_{21} is the largest when β is 0˚ and has a negative value. As β increases, the magnitude of K_{21} increases until it becomes positive at a β of roughly 55˚ and the largest positive K_{21} occurs when $\beta = 90^{\circ}$. This explains why *PD* decreases as you increase β from 0˚ (Fig. 6.6) to 30˚ (Fig. 6.7). The sensitivity of K_{21} to β also depends on the size parameter. For small to moderate size parameters the sensitivity is the largest, and large size parameters exhibit little to no sensitivity of K_{21} to β.

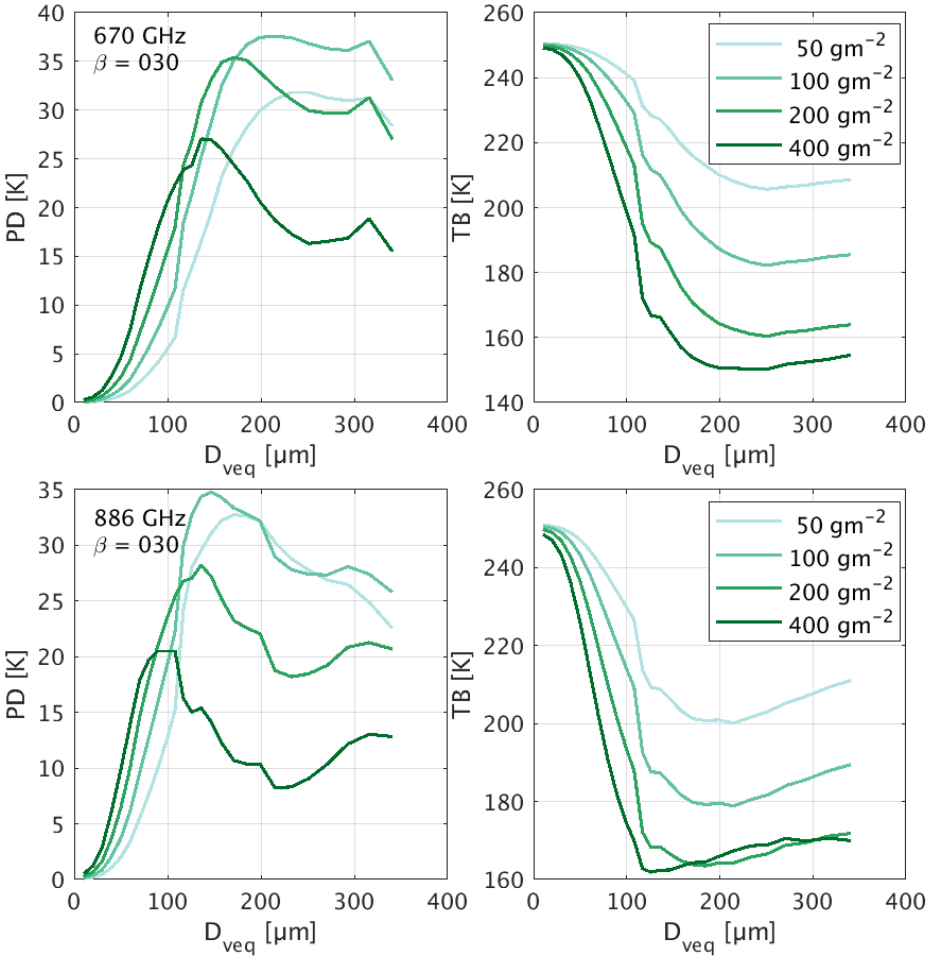

Figure 6.7: Same as Fig. 6.6 except with a particle tilt angle of $\beta = 30^{\circ}$.

6.3. Mixture of randomly and horizontally oriented particles

From the previous section, we now have some insight into what drives the polarization signature corresponding to hexagonal plate particles that are totally random and azimuthally randomly oriented, as well as the influence of particle tilt angle on the polarization signature. For those simulations we made the assumptions that the particle size distribution is monodisperse and that all particles within the cloud possess the same orientation and tilting angle. However, we know this is not physically representative of ice clouds, and previous studies have shown that particles of a certain size and location in the cloud exhibit an azimuthal orientation, with the rest of the particles in the cloud being randomly oriented. Therefore, the aim of this section is to understand how polarization signatures vary when we assume certain percentages of the particles (by mass) azimuthally oriented, with the remainder being totally oriented.

To accomplish this, our simulation setup is as follows. First, we retain the same *IWP* values used in the previous section and assume that certain percentages of the total mass of ice corresponds to azimuthally oriented particles, with the remainder being randomly oriented. For example, assuming 10% of the particles corresponding to an *IWP* of 100 g/m^2 are azimuthally oriented means that we now have IWP_a = 10 g/m^2 and IWP_t = 90 g/m^2, where the subscripts *a* and *t* correspond to azimuthal and total, respectively. We also assume that all azimuthally oriented particles are located at the top of the cloud, since previous studies have shown these particles typically occur at the top of the cloud. Think of this as stratifying the cloud into two layers, with randomly oriented particles comprising the bottom layer and azimuthally oriented particles comprising the top layer.

The cloud top height and geometric thickness are the same as assumed in the previous section. We can now describe *PD* in terms of *IWP*, D_{veq}, β, and *f*, where *f* is the fraction of particles that are horizontally oriented.

Figures 6.8 and 6.9 show *PD* (left column) and *TB* (right column) as a function of D_{veq} when azimuthally oriented particles comprise 5% (top row), 10% (middle row), and 30% (bottom row) at 670 and 886 GHz, respectively. When looking at *PD* in Fig. 6.8, first notice that as the fraction of particles that are azimuthally oriented increases (from top row to bottom), the magnitude increases. Regardless of *f*, there are nice relationships between *PD* and *IWP* as well as *TB* and *IWP*, particularly as the particle size approaches 100 μm. Another interesting result is that *TB* is essentially invariant with *f*, at least for the values shown here. Figure 6.9 shows similar trends for *PD* and *TB* computed at 886 GHz. However, as mentioned previously, because the opacity is larger at higher frequency channels which are more sensitive to smaller *IWP* and particle sizes, we see *PD* begin to decrease at smaller particle sizes and *IWPs* at 886 GHz compared to 670 GHz. This evident when looking at *PD* for $f = 30°$ (bottom left panel). *PD* at the largest *IWP* (darkest green line) is starting to decrease as the particle size becomes large. Although, Figs. 6.8 and 6.9 only provide results at $f = 5$, 10, and 30%, the trends described above hold for 5, 10, 20, 30, 40, and 50% fractions of azimuthally oriented particles, but in order to conserve space are not provided.

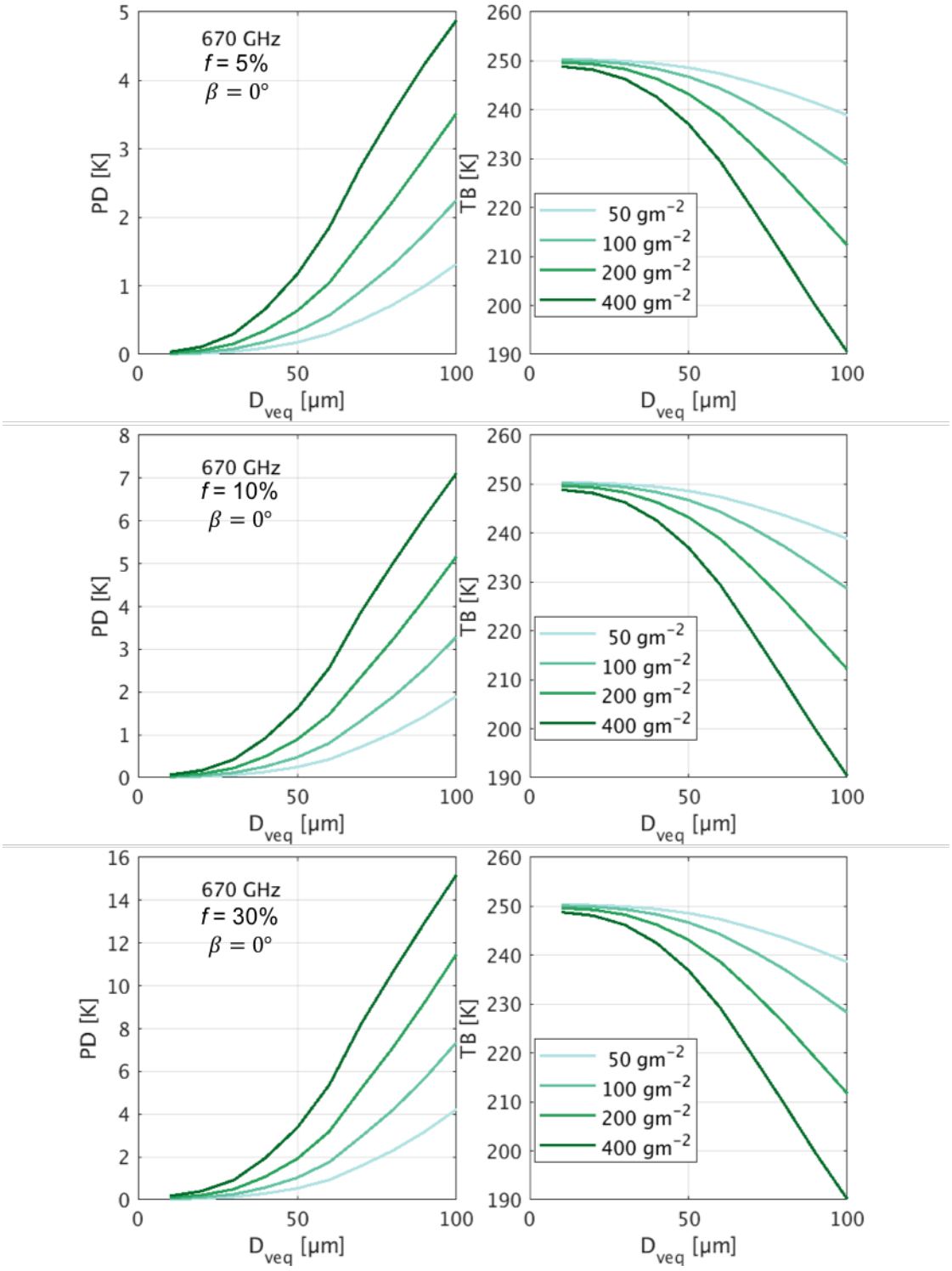

Figure 6.8: *PD* and *TB* sensitivity at 670 GHz to particle size, assuming azimuthally oriented ice particles with tilt angle $\beta = 0^{\circ}$. The top (middle, bottom) row corresponds to 5% (10%, 30%) fraction (*f*) of azimuthally oriented particles. The colors correspond to different *IWP* values.

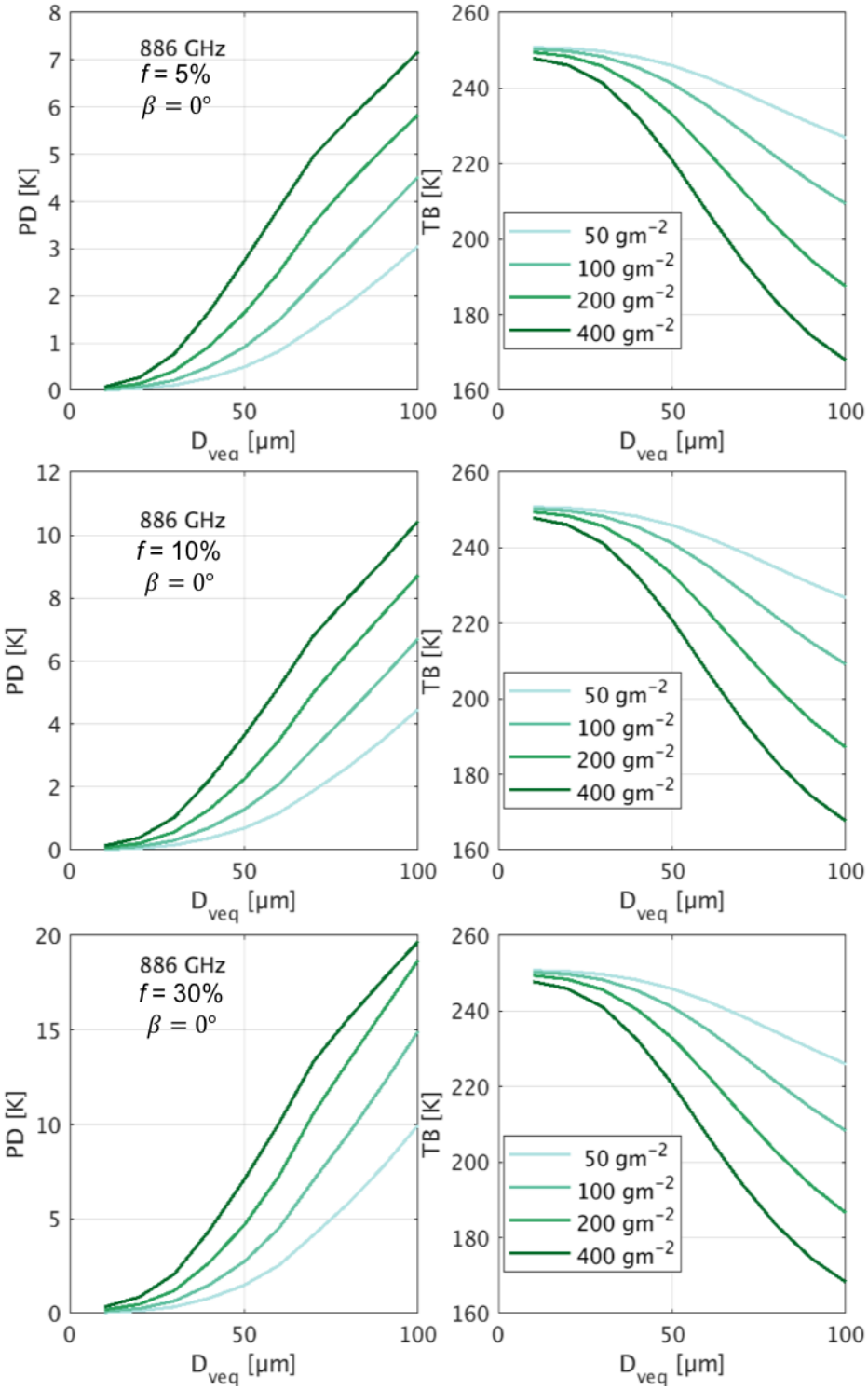

Figure 6.9: *PD* and *TB* sensitivity at 886 GHz to particle size, assuming azimuthally oriented ice particles with tilt angle $\beta = 0^{\circ}$. The top (middle, bottom) row corresponds to 5% (10%, 30%) fraction (*f*) of azimuthally oriented particles. The colors correspond to different *IWP* values.

In the previous section, we demonstrated that *PD* and *TB* can vary significantly with tilt angle β. The logical next step is to determine if the relationships between *IWP*, *PD*, and *f* shown in Figs. 6.8 and 6.9 hold when we assume some tilting angle for the azimuthally oriented particles. To accomplish this, we simulate *PD* and *TB* in the previous fashion and simply change β. The results of these simulations are provided in Figs. 6.10 and 6.11 for 670 and 886 GHz, respectively. The first thing to notice about Figs. 6.10 and 6.11 is that the magnitude of *PD* decreased as β increased to 30°, which makes sense based on previous figures and discussions. Maximum *PD* values at 670 GHz when $\beta = 0°$ are approximately 5, 7, and 17 K for *f* values of 5, 10, and 20%, respectively. When $\beta = 30°$, the corresponding *PD* maximums for *f* values of 5, 10, and 30% decrease to roughly 4, 5, 10 K. The same is true when looking at the results for 886 GHz. It is also worth noting again the *TB* is essentially invariant with *f* and β, at least for the values of *f* and β considered here. There are several important points from Figs. 6.8 through 6.11 which should be emphasized:

1. *TB* and *PD* are both exhibit high sensitivity to particle size and *IWP*, regardless of β, *f*, or frequency. This is particularly true for large particles.
2. Simulated *TBs* are essentially invariant with *f* and β.
3. The magnitude of simulated *PD* at a given particle size and *IWP* increases as the proportion of azimuthally oriented particles, *f*, increases.

It is important to again note that the results presented here only apply to a single hexagonal plate particle with a monodisperse particle size distribution, and a tropical summer atmosphere. The most noteworthy takeaway from these simulations is provided

in point 3 above, which raises the question: Is it possible, given a particular particle size and *IWP,* to use the corresponding *PD* measurements to determine the fraction of ice particles which are azimuthally oriented?

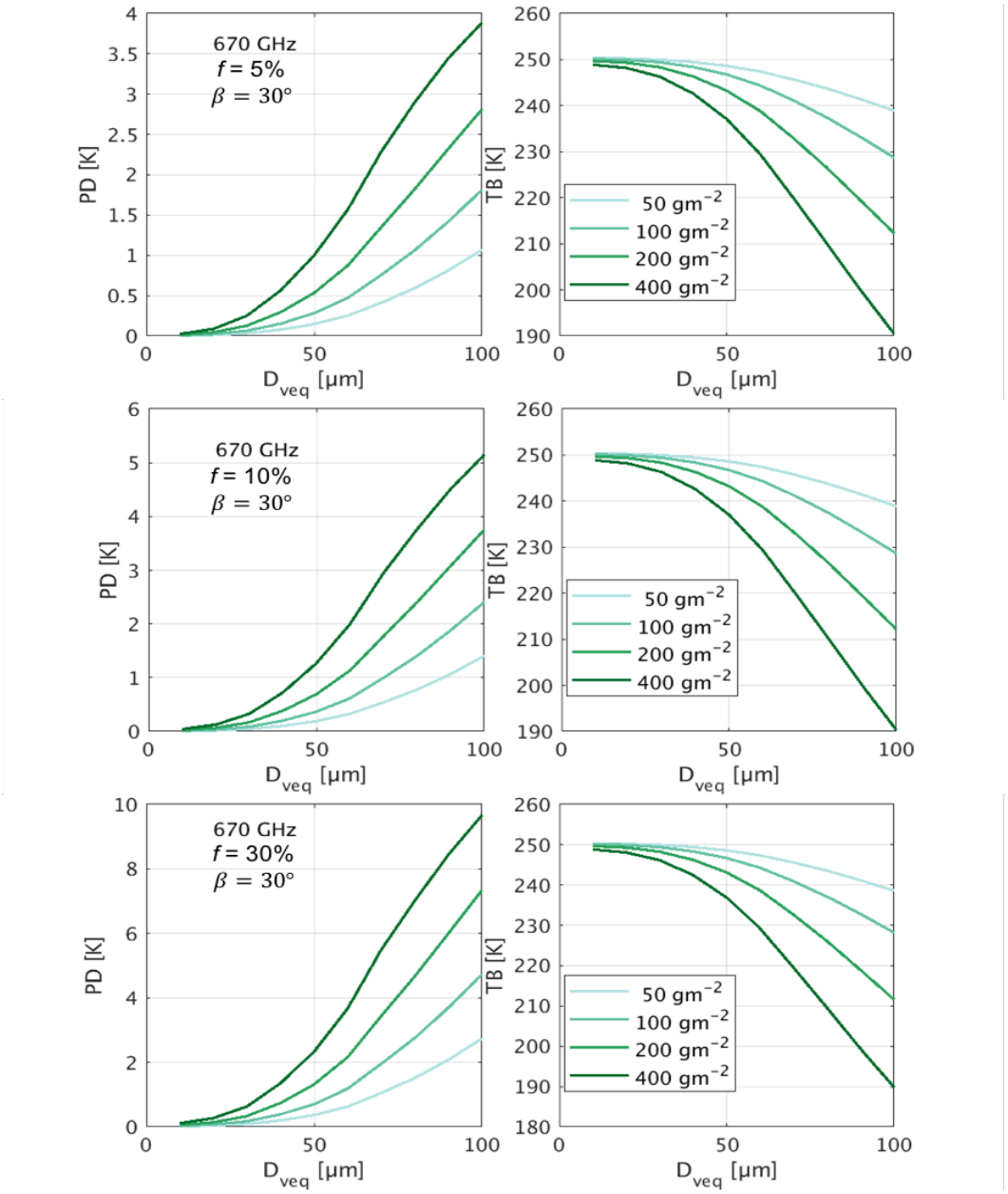

Figure 6.10: Same as Fig. 6.8, except $\beta = 30°$.

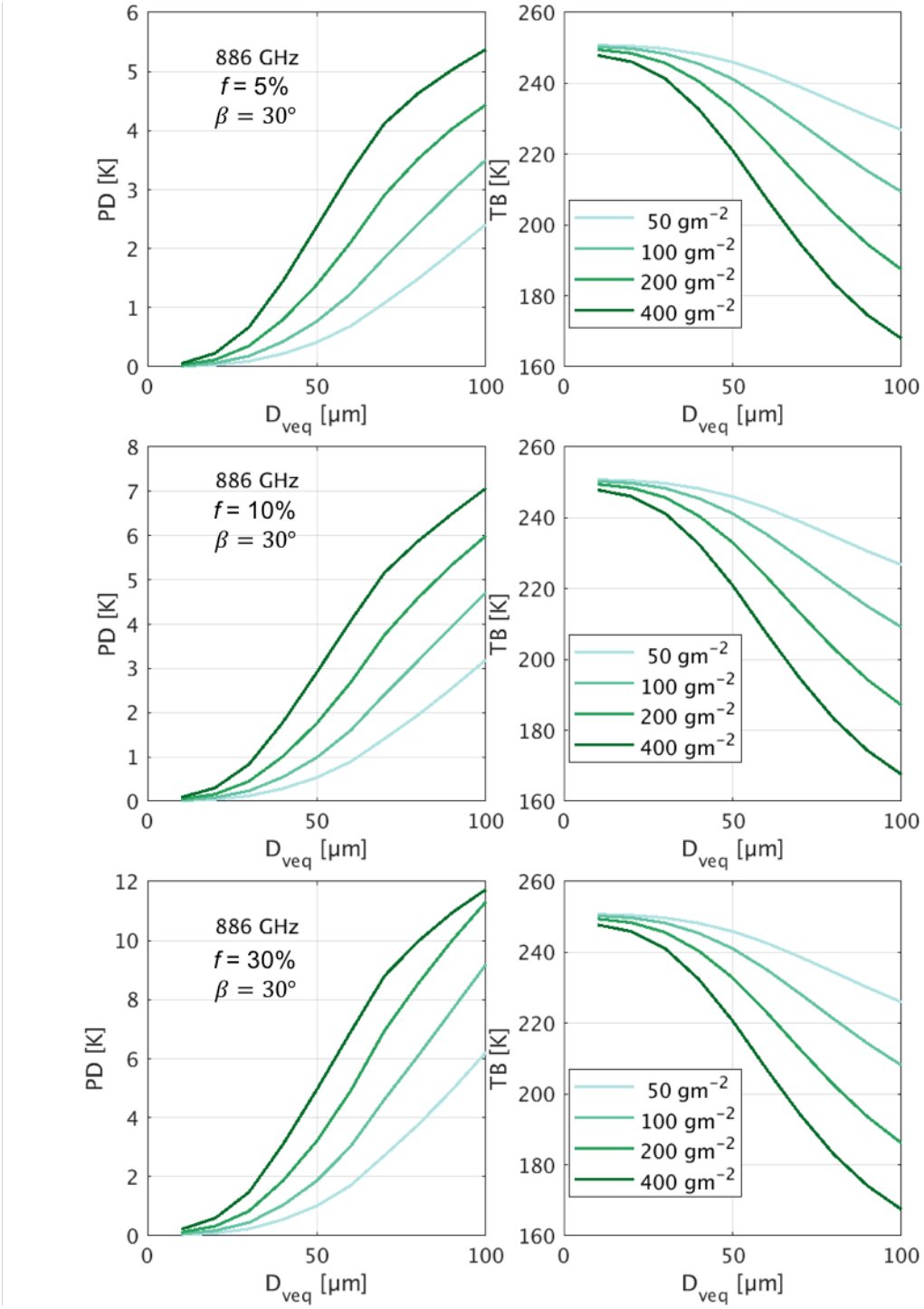

Figure 6.11: Same as Fig. 6.9, except $\beta = 30°$.

To address the question posed above, we now assume a particular *IWP* and particle size, then plot *PD* and *TB* as a function of the percentage of azimuthally oriented particles present in the cloud. The results for 670 and 886 GHz are provided in Figs. 6.12 and 6.13, respectively. These figures show *PD* (left column) and *TB* (right column) as a function of percent mix, meaning the percent of total *IWP* that is azimuthally oriented. The different shades of red lines correspond to different *IWP* values, with the darkest line corresponding to the highest *IWP*. When looking at Fig. 6.12, the first thing to note is there is a very linear response of *PD* and *TB* to the fraction of horizontally oriented particles for a particular particle size and *IWP*. When comparing *PD* (left column) to *TB* (right column), it is evident that *TB* shows little sensitivity to *f*. Conversely, *PD* is significantly more sensitive to the mixing fraction of azimuthally and randomly oriented particles, particularly as *IWP* and particle size becomes large. Note that when the particle size is small (top row Fig. 6.12), *PD* responds similarly to changes in *f* and *IWP*, compared to large particle sizes. However, the magnitude of *PD* corresponding to these *IWP* values is small (less than 1K), meaning the signal to noise ratio is low and consequently it may not be possible to extricate the signal from the noise. However, this is not an issue though for larger particle sizes (~50 μm or larger), particularly when *IWP* is large. It is important to note, we computed *PD* and *TB* (as in Fig. 6.12) for particle sizes ranging from 10-100 μm in increments of 10 μm, but only show a subset (20, 50 and 100 μm) to conserve space. These additional figures all show the same results however, of a very linear relationship between *PD* and percent mix.

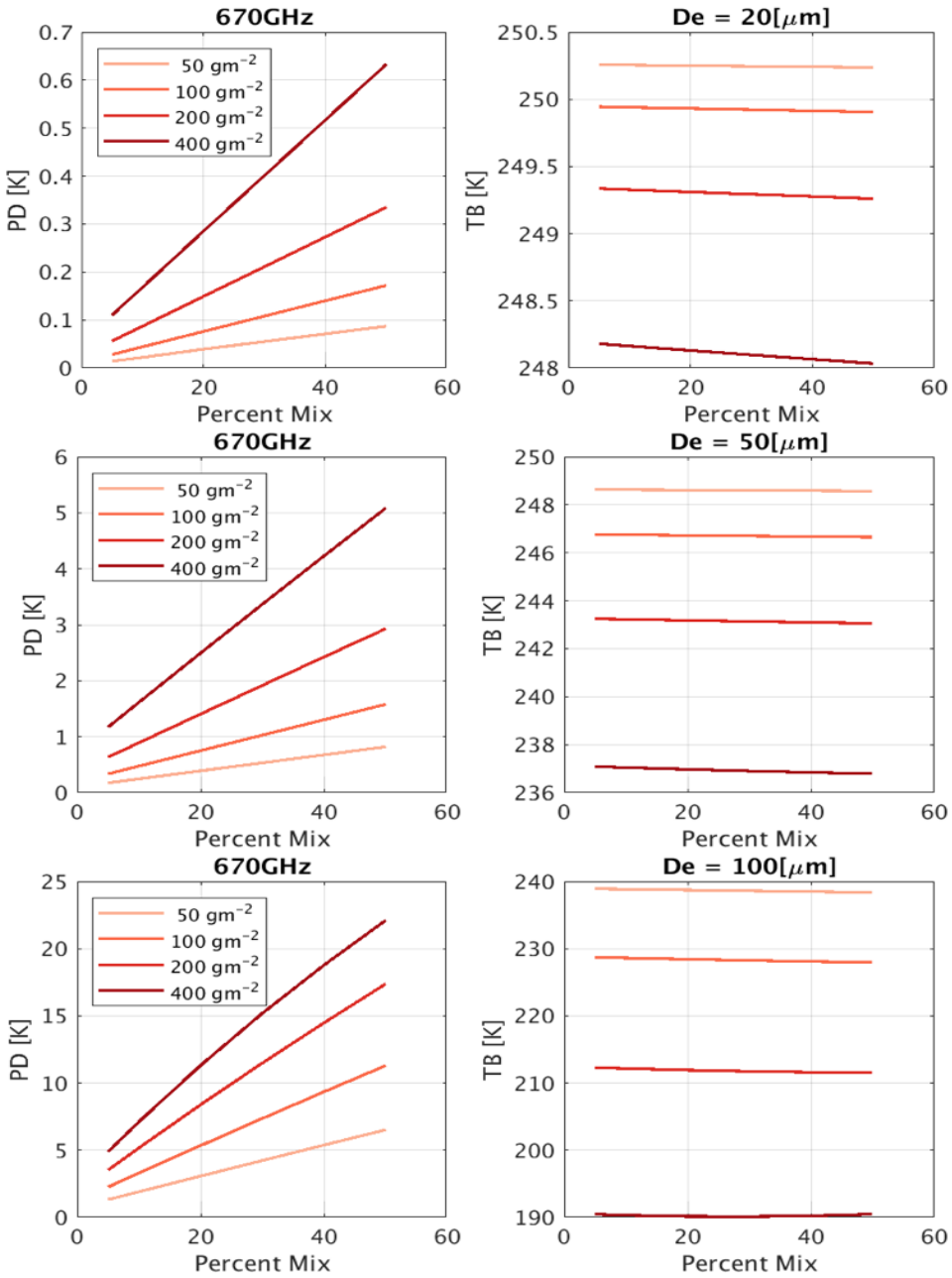

Figure 6.12: *PD* and *TB* sensitivity at 670 GHz to particle orientation mixing fraction (*f*), assuming oriented particles with $\beta = 0^{\circ}$. The top (middle, bottom) row corresponds to a D_{veq} of 20 μm (50 μm, 100 μm). The colors denote different *IWP* values.

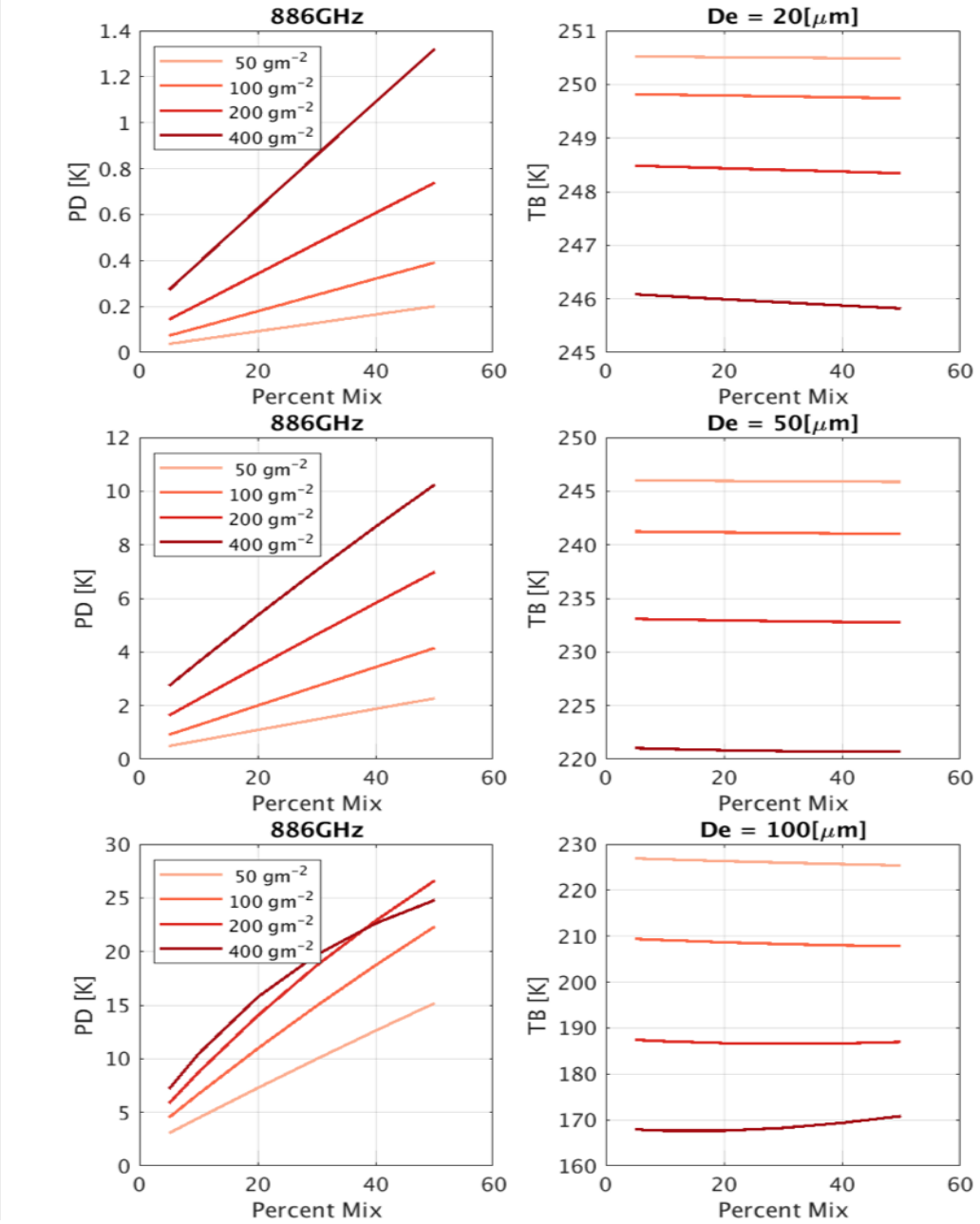

Figure 6.13: *PD* and *TB* sensitivity at 886 GHz to particle orientation mixing fraction (*f*), assuming oriented particles with $\beta = 0^{\circ}$. The top (middle, bottom) row corresponds to a D_{veq} of 20 μm (50 μm, 100 μm). The colors denote different *IWP* values.

Figure 6.13 shows the results at 886 GHz. Similar linear responses of *PD* to percent mix are again evident. However, note *PD* (left column) for large particles

(bottom row) now shows *PD* at the largest *IWP* (400 g/m^2) decreasing after reaching ~30% mix and is actually smaller than *PD* corresponding to 200 g/m^2 after ~40% mix. Recall that as *IWP* or particle size increases, we expect an enhancement of the scattering effect, which results from an increase in particle number density or scattering efficiencies. When particle size or *IWP* becomes large enough, the optical depth of the increases such that the multiple scattering effect dominates. Also note that the magnitude of *PD* for 886 GHz is roughly two times larger than for 670 GHz for the two smallest particle sizes shown in the figures but is proportional *PD* at 670 GHz for the largest particle size (100 μm). These figures were also produced assuming $\beta = 30°$, but look nearly identical to Figs. 6.12 and 6.13 that assume $\beta = 0°$. The only noticeable difference is that the magnitude of *PD* for $\beta = 30°$ is less than Figs. 6.12 and 6.13, and therefore the results for $\beta = 30°$ are not included here.

6.4. Conclusions

As previously mentioned, *PD* can provide rich information about cloud microphysical properties, such as ice particle shape, size and orientation. In this chapter, we investigate the impact of polarization measurements on cloud property retrievals. Figure 6.2 demonstrates the relative improvement of adding polarization to retrieve D_{eff} with the bottom right panel producing overall the closest agreement between real and retrieved values. In this chapter we also explored how particle orientation influences simulated *TB* and *PD*. Lastly, we investigated the impacts of assuming a mixture of azimuthally and randomly oriented particles. The linear response of *PD* to the percentage of azimuthally oriented particles lends confidence to the potential of using

PD at the sub-mm frequencies to infer, or retrieve, the fraction of horizontally oriented particles within the cloud. One important closing note is to recall that the magnitude of *PD* is much smaller for randomly oriented particles than their azimuthally oriented counterparts. This is important because the large Q, or the second element of the Stokes vector, can significantly influence simulated intensity values if one is not solving the vector radiative transfer equation.

7. ICE CLOUD PROPERTY RETRIEVALS

In Chapter 4 we provided a simple channel selection study based on the orthogonality (sensitivity) of LUTs for a variety of sub-mm and infrared channels. From this study we concluded that the combination of two sub-mm channels (640, 874 GHz) and one infrared (12 μm) demonstrated the highest sensitivity for *IWP* less than 200 g/m^2 and D_{eff} less than 100 μm. However, this analysis did not include the effects of polarization. In Chapter 6, we presented an additional channel selection analysis which focused on the relative improvements of adding polarized measurements, or more precisely *PD*, to retrieve D_{eff}. In this Chapter we build on the two previous channel selection analyses and present examples of retrieved *IWP* and D_{eff} for different combinations of frequencies, both with and without polarization, in order to determine which combination of measurements provides the closest estimate to the true values.

7.1. Synthetic data

Before defining the various measurement frequencies to be used, it is useful to provide a brief discussion concerning the synthetic data to be used in the retrievals. In an effort to make the synthetic data as physically realistic as possible, *TB* and *PD* in the presence of ice clouds are simulated with atmospheric and cloud characteristic data from several CloudSat products, as outlined in Chapter 4. Since this work is primarily focused on retrieval of tropical ice cloud properties, we only select data within $\pm 20°$ latitude. From this data we extract cloud characteristics such as cloud top/base height. Figure 7.1 is a 2D histogram showing the cloud top height (ordinate) and cloud geometric thickness

(abscissa) from CloudSat. This figure shows a wide range of cloud top heights, from ~7 to 18 km, with the highest concentration of pixels having a top height of ~13 km.

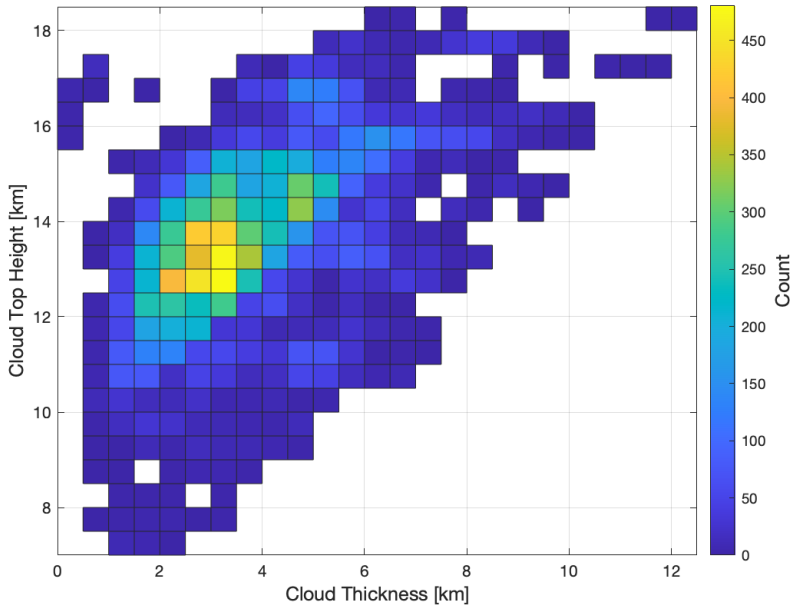

Figure 7.1: 2D histogram of cloud top heights and geometric thicknesses assumed in generating synthetic measurements.

From this CloudSat data, we obtain *IWP* and D_{eff}, which are necessary to simulate measurements and are also used as the "true" *IWP* and D_{eff} to compare against their retrieved counterparts. Figure 7.2 is a 2D histogram describing the range and concentrations of *IWP* (abscissa) and D_{eff} (ordinate). This figure shows that for the majority of the pixels *IWP* is less than 200 g/m^2 and D_{eff} is less than 100 µm, which corresponds to the range of cloud conditions designated for the channel selection study presented in Chapter 4 and discussed at the beginning of this chapter. However, much

larger values of *IWP* are also shown in Fig. 7.2, which are typically problematic for sub-mm retrievals.

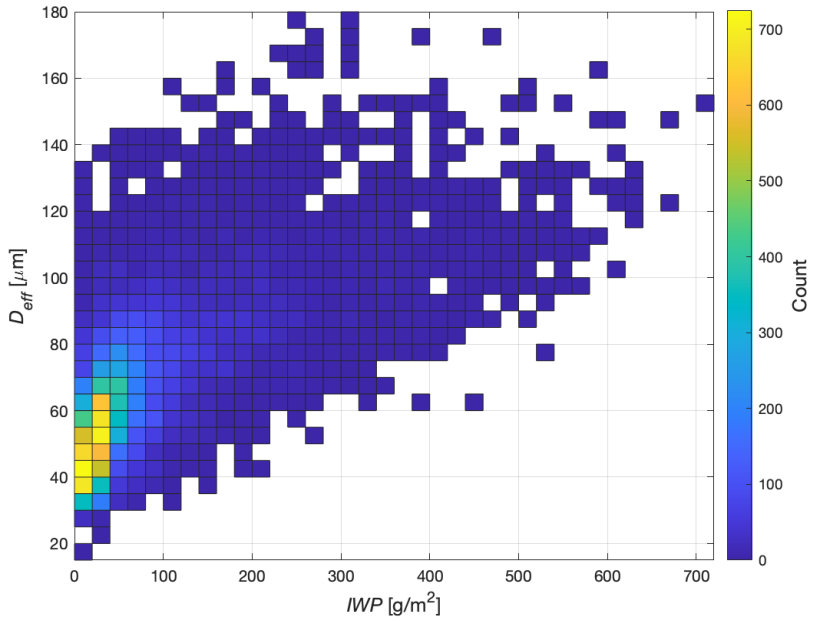

Figure 7.2: 2D histogram of *IWP* and D_{eff} values assumed in generating synthetic measurements. These values are used as the "true" values to compare against retrieved values.

In addition to the cloud property information shown in Figs. 7.1 and 7.2, we also require vertical profiles of pressure, temperature, and concentrations of absorbing species. The most important among these in the sub-mm spectral region is water vapor, particularly for high frequencies where water vapor screening can be problematic. Figure 7.3 shows the volume mixing ratios (VMR) of the main absorbing species considered in these simulations as a function of pressure. Note the significant variance of water vapor (top panel) compared to O_2 and O_3. Therefore, in order to reduce the computational burden and to add simplicity in generating the synthetic data, we simply compute the mean profile for O_2 and O_3 and assume that profile when simulating *TB* and *PD* for all

pixels. All temperature and specific humidity profiles are obtained from the ECMWF-AUX product in order to maintain consistency with CloudSat retrievals. Previous sensitivity studies demonstrated assuming a mean profile of O_2 and O_3 VMRs produced changes in *TB* and *PD* that are much less than those ascribed to measurement uncertainty or noise.

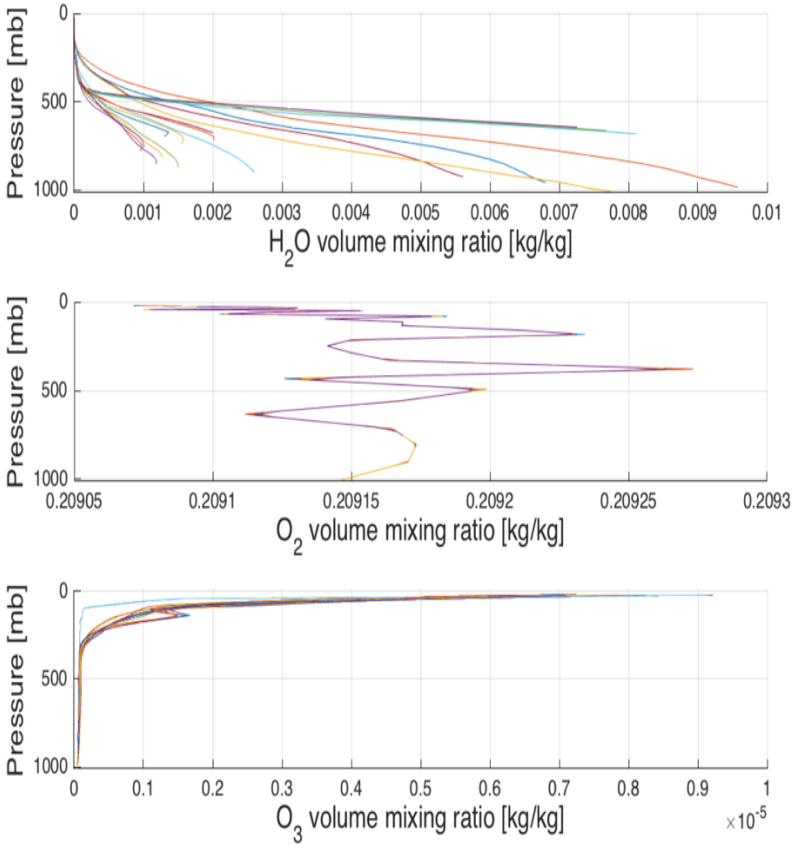

Figure 7.3: VMR profiles for the main absorbing species included in generating synthetic measurements.

In all simulations an aggregate of severely roughened hexagonal columns is assumed as the ice particle shape model. We also assume that particles are randomly oriented and follow a gamma size distribution with and effective variance of 0.1. The viewing zenith angle is set at 53.5°, which is consistent with existing microwave conical scanners. Details specific to the retrieval setup, including the measurement bands, is presented in the next section.

7.2. Ice cloud property retrievals

With the aforementioned CloudSat data (Figs. 7.1 through 7.3) and assumptions of the particle habit and particle size distribution, we can now simulate *TB* and *PD* for the purpose of the retrievals. In this chapter we consider four different sub-mm frequencies (325, 448, 640, 874 GHz) and one IR wavelength (12 μm). From these bands, we identify 12 different measurement combinations, which are provided in Table 7.1. For ease of reference, each combination is given a particular ID number. The superscript $^+$ by a particular channel means that polarization, or *PD*, is included in addition to *TB*. For example, 640 GHz listed in the table will contribute only *TB* to the measurement vector, whereas 640^+ will contribute *TB* and *PD*. There is an exception, however, which is noted by the asterisk in ID 112. In this case, only *PD* at 325 GHz is included in the measurement vector. The same is the case for $640^+/325^+$, where strictly the ratio of *PD* is included. These combinations are selected based on sensitivity and numerical analyses in an effort to provide estimates of *IWP* and D_{eff} that most closely match the true values.

Table 7.1 *Measurement combinations used in example retrievals. All units are GHz, with the exception of 12, which is in μm. Values with a superscript denote polarization is included (i.e., both TB and PD are in the measurement vector, and an asterisk denotes only PD is included but not TB.*

ID Number	Values				
101	640	874			
102	640	874	12		
103	325	448	640	874	
104	640^{+}	874^{+}			
105	640^{+}	874^{+}	12^{+}		
106	640	874	12^{+}		
107	325	448	640	874	12
108	448	640	874		
109	448	640	874	12	
110	448^{+}	640^{+}	874^{+}	12^{+}	
111	325^{+}	448^{+}	640^{+}	874^{+}	12^{+}
112	$*325^{+}$	640^{+}	874^{+}	12^{+}	$*640^{+}/325^{+}$

As a point of clarification, all sub-mm channels shown in Table 7.1 use the difference between cloudy *TB* and that associated with a clear sky, or ΔTB. Therefore, success of the retrieval depends on our ability to obtain an accurate representation of clear-sky *TB*, which can be a large obstacle for sub-mm remote sensing of ice cloud properties. One way to obtain clear-sky *TB* is by simultaneously retrieving the water vapor profile and subsequently calculating *TB* via a radiative transfer simulator. However, for the purposes of the retrievals presented in this thesis, we use a proxy value. Numerical simulations showed that *TB* at 448 GHz, which is a water vapor absorption band, closely approximates the clear-sky *TB* over a wide range of cloud conditions. Figure 7.4 shows clear-sky *TB* as a function of frequency for a tropical, mid-latitude winter, and sub-arctic summer atmosphere, where water vapor profiles are expected to vary significantly. Notice at 448 GHz, *TB* is approximately the same for all three conditions.

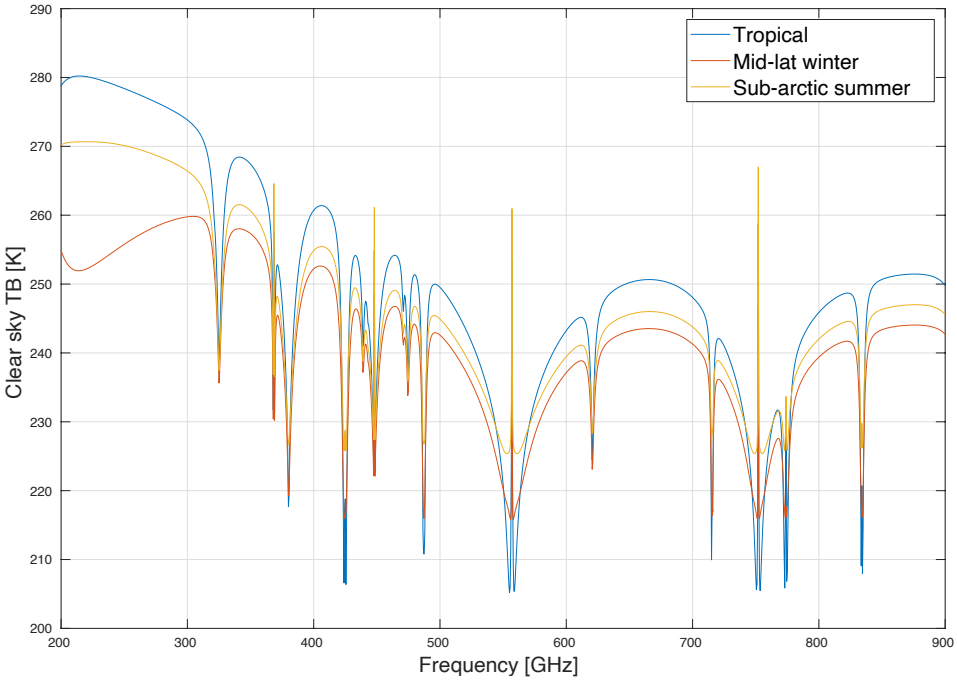

Figure 7.4: Clear-sky *TB* as a function of frequency for three atmospheric scenarios. Lines correspond to tropical, mid-latitude winter, and sub-arctic summer atmospheres.

Going one step further, we compute *TB* at 448 GHz in the presence of ice clouds, and for a wide range of *IWP* and D_{eff}. Figure 7.5 shows ΔTB as a function of *IWP* and D_{eff}. As is evident from the figure, the magnitude of ΔTB is small over the entire range of *IWP* and D_{eff} values. Therefore, for all retrievals conducted in this chapter, *TB* at 448 GHz is used as a proxy for clear-sky *TB*, even 448 GHz is not used to explicitly infer *IWP* or D_{eff}.

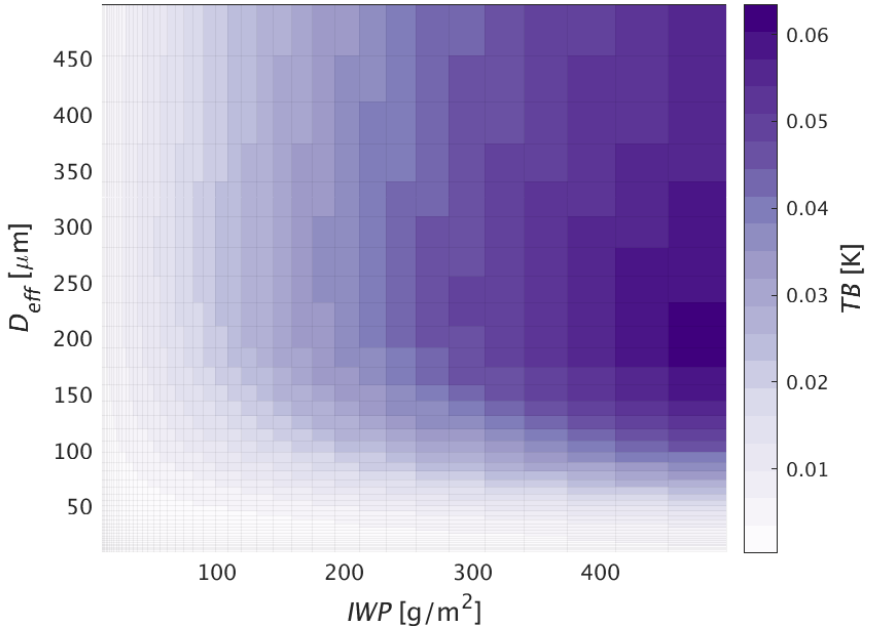

Figure 7.5: ΔTB as a function of IWP and D_{eff} at 448 GHz. ΔTB is defined as $TB_{clear\ sky} - TB_{cloudy}$.

In order to determine the quality of retrievals using the different band combinations, we compute the root mean square (RMS) error and R^2 value for both IWP and D_{eff}. Recall when discussing the retrieval methodology in Chapter 4, that it is necessary to provide some *a priori* value of the parameters to be retrieved. It is common practice to select a climatological value, however, for the purpose of the retrievals presented here we simply take the mean values of IWP and D_{eff} to be the *a priori* estimate. There is a total of 17076 pixels (measurements) comprising this synthetic dataset, with a mean IWP and D_{eff} of 67.1 g/m^2 and 63.7 μm, respectively. Instead of showing a figure for all 12 retrievals shown in Table 7.1, the results are provided for convenience in Table 7.2. However, some example figures are provided below for clarity.

Table 7.2: *Error of retrieved IWP and D_{eff} for the different measurement combinations. Note the superscript $^{+}$ denotes that polarization is included in the retrieval, and an asterisk denotes only PD is included but not TB.*

		IWP		***D_{eff}***	
ID #	Values	RMS	R^2	RMS	R^2
101	640, 874	24.57	0.929	15.82	0.651
102	640, 874, 12	26.53	0.919	14.69	0.744
103	325, 448, 640	24.66	0.929	15.77	0.660
104	640^{+}, 874^{+}	24.66	0.927	15.84	0.657
105	640^{+}, 874^{+}, 12^{+}	25.32	0.925	15.10	0.741
106	640, 874, 12^{+}	25.77	0.922	14.97	0.727
107	325, 448, 640, 874, 12	26.45	0.918	14.90	0.741
108	448, 640, 874	24.63	0.928	15.83	0.651
109	448, 640, 874, 12	26.54	0.919	14.70	0.743
110	448^{+}, 640^{+}, 874^{+}, 12^{+}	25.39	0.923	15.15	0.738
111	325^{+}, 448^{+}, 640^{+}, 874^{+}, 12	26.08	0.917	14.86	0.742
112	$*325^{+}$, 640^{+}, 874^{+}, 12^{+}, $*640^{+}/325^{+}$	18.02	0.962	7.36	0.937

One initial takeaway from Table 7.2 is that the RMS of retrieved *IWP* is larger than the RMS for D_{eff}, however D_{eff} retrievals have a larger R^2. This is due to the large bias of retrieved *IWP* for large *IWP* values where sub-mm channels lose sensitivity. Also, note that ID 112 exhibited a much better performance than its counterparts. To understand this behavior, let us look at an example retrieval. Figure 7.6 shows retrieved *IWP* (left) and D_{eff} (right) corresponding to ID 101 in Table 7.2. When looking at the left panel, it is evident that retrieved *IWP* more closely approximates the true value for low *IWP*. This makes sense because sub-mm sensitivity to *IWP* is greatly reduced as *IWP* becomes larger, primarily due to the multiple scattering effect becoming dominant. Another noteworthy feature in Fig. 7.6 is the striping pattern present in both *IWP* and D_{eff}. This stripe occurs at the *a priori* values because there is insufficient information content in the measurements, and consequently the retrieval converges on the *a priori*

value. This is not surprising because there are only 2 elements in the measurement vector.

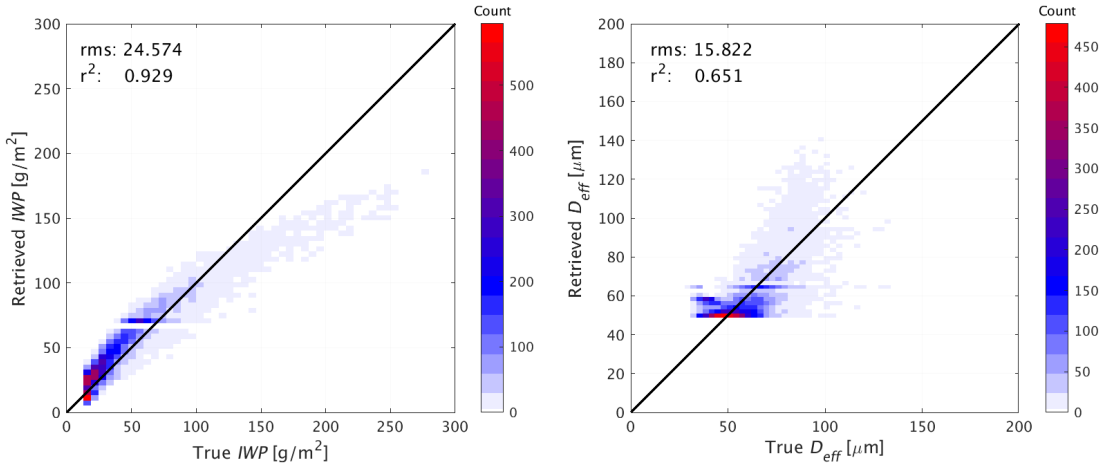

Figure 7.6: Retrieved *IWP* and D_{eff} corresponding to ID 101 in Tables 7.1 and 7.2. *IWP* (D_{eff}) is shown in the left (right) panel.

In order to mitigate this information content problem seen in Fig. 7.6 it is necessary to add additional measurements. However, ignoring the results in Table 7.2, the choice of which measurements to include is not trivial. In Fig. 7.6 we see that retrieved D_{eff} poorly estimates the true value, particularly for smaller D_{eff}. Therefore, it is likely prudent to include polarization measurements which are sensitive to D_{eff}, or even the ratio of *PD* at two channels, as was shown in Fig. 6.1 to be very sensitive to small and moderate sized particles. This procedure is almost akin to solving a puzzle. We know an area of the parameter space which lacks sensitivity, and we then select different measurements based the physical characteristics which might make them beneficial in the retrieval. In this case, the last puzzle piece corresponds to ID 112 in Tables 1 and 2. This configuration contains 325 GHz, but only *PD*. This is because there is only minimal

sensitivity to *IWP* for moderate sized *IWP*, although is sensitive to D_{eff}. ID 112 also incorporates *TB* and *PD* at 640 GHz, 874 GHz, and 12 μm, as well as the ratio of *PD* (640/325 GHz). It is evident from Table 7.2 that this combination showed the best retrieval performance, so let us now look at the results, shown in Fig. 7.7.

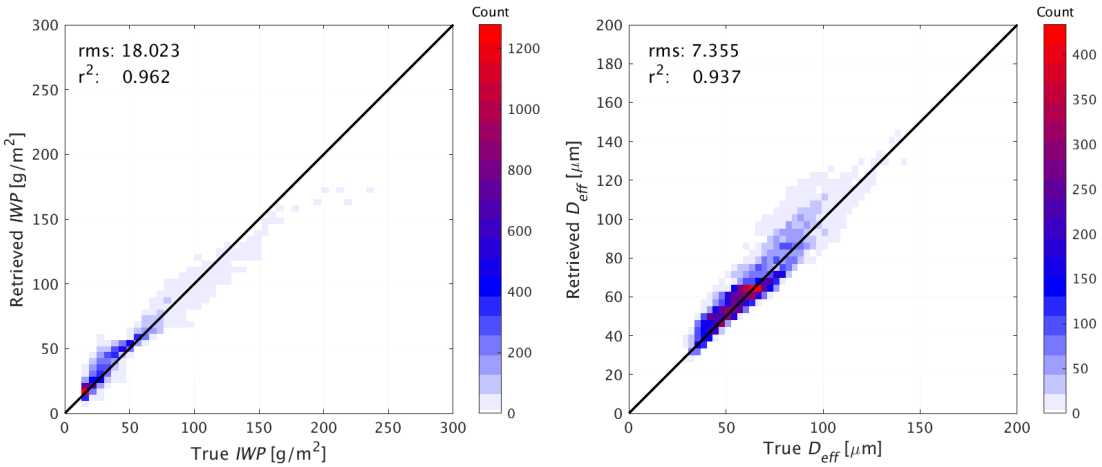

Figure 7.7: Retrieved *IWP* and D_{eff} corresponding to ID 112 in Tables 7.1 and 7.2. *IWP* (D_{eff}) is shown in the left (right) panel

When looking at Fig. 7.7, we see a better agreement for retrieved and true *IWP* values when *IWP* is large. There is also a significant improvement seen for moderate D_{eff} values, which is due to the addition of the ratio of two sub-mm *PDs*. Overall, this selection of measurements provides a much better estimation of the true values that the other combinations. Based on these results, we feel confident that retrievals conducted with these spaceborne sub-mm and IR polarimetric measurements can accurately infer ice cloud properties such as *IWP* and D_{eff}.

8. SUMMARY AND OUTLOOK

The overarching goal of this thesis was to improve our understanding of how sub-mm wave radiation interacts with ice clouds, and subsequently develop a methodology to infer, or retrieve, ice cloud properties from spaceborne polarized sub-mm and IR measurements. An additional aim of this thesis is to provide insight to those working towards future sub-mm sensor launches, such as those by NASA and other international agencies, as outlined in Chapter 2. The approach to accomplish this involved three key aspects.

The first aspect involved conducting a series of numerical sensitivity analyses to ascertain how sub-mm radiances respond to changes in ice cloud properties, such as cloud ice mass (*IWP*), particle size (D_{eff}), shape and orientation, and cloud top height. A discussion of these sensitivity studies is provided in Chapter 5. Our results confirmed that sub-mm radiation is most sensitive to small D_{eff} and low *IWP*. We further showed that sensitivity to particle shape is low but incorporating a mixture of ice particle shape models in retrievals could provide additional information content to a wider range of *IWP* and D_{eff} values. The analyses in Chapter 7 showed that sub-mm *PD* is extremely sensitive to particle orientation. From our analyses we conclude that the sensitivity to particle shape is increased when particles are assumed to be azimuthally (horizontally) oriented.

The second aspect was the development of a retrieval algorithm capable of reliably characterizing ice cloud properties with sub-mm and IR measurements. An

optimal estimation-based framework is selected for the retrieval along with the Levenberg-Marquardt iteration scheme, which is appropriate for nonlinear inverse problems. Details of the retrieval are provided in Chapter 4. We also chose to incorporate information content as an additional metric of quantifying retrieval quality. Taken together, retrieval accuracy and information content effectively provide a quantitative description of the retrieval process from observations to final products. Retrieval performance for different combinations of sub-mm frequencies, both with and without polarization, is presented in Chapter 7.

Finally, we analyzed sub-mm polarized scattering signals of ice clouds to determine their sensitivities to particle shape and orientation. From these analyses we conclude that the effect of particle orientation on polarized cloud scattering signatures in the sub-mm spectral region cannot be ignored. Furthermore, the large Q (second element of Stokes vector) due to horizontally oriented particles can significantly influence simulated intensity values when solving the scalar versus the vector radiative transfer equation. We also investigated the impacts of mixtures of horizontally and randomly oriented particles within clouds, and this analysis lends confidence to the ability of polarized sub-mm measurements to infer the fraction of horizontally oriented particles in the cloud. These analyses are provided in Chapter 6.

This doctoral research project contributes to furthering our understanding of how sub-mm radiation interacts with ice clouds and provides insight and tools useful to retrieve ice cloud properties from spaceborne sub-mm measurements. In particular, a novel part of the algorithm presented here is that is utilizes polarized *TBs* in both the

high-frequency sub-mm and IR wavelength regimes, of which there is a lack of studies exploring the benefits. Furthermore, the myriad numerical analyses conducted to quantify the sensitivity of simulated *TBs* to assumed ice cloud properties, such as particle shape and orientation, provides information concerning the uncertainty of retrieved cloud microphysical properties. At the time of writing this dissertation, we believe that this study provides the most exhaustive assessment of uncertainties in simulated sub-mm and IR measurements due to model assumptions, and the subsequent implications in terms of retrieved cloud properties and measurement information content. Knowledge of these uncertainties is a useful tool for future researchers, not only for constraining existing retrievals, but aids the development of new retrieval algorithms to infer ice cloud properties from sub-mm and IR polarized measurements. However, as the need and desire for polarized measurements increases, a rigorous characterization of cloud 3D effects is necessary, but is beyond the scope and framework of the presented research. While systematic biases due to field of view averaging are less impactful in the sub-mm spectral region (as compared to thermal IR), it is important future work to quantify these beam-filling effects, in addition to actual 3D radiative transfer effects.

Furthermore, while we showed the implications of particle orientation on polarized measurements to be significant, the ratio of azimuthally oriented to randomly oriented particles is small in most cases. Therefore, even though this signal is large, given the difficulty and complexity of assuming azimuthally oriented particles in cloud property retrievals as we have shown, we recommend that ice particle models be randomly oriented, and the presence of oriented particles be treated in terms of the

measurement error covariance. Lastly, in addition to informing future research efforts to constrain ice cloud property retrievals and develop new spectrally consistent synergistic algorithms ranging from the thermal IR to the sub-mm, more broadly this research contributes to one of NASA's overarching goals in Earth Science: *advance the understanding of the change in Earth's radiation balance…that result from changes in atmospheric composition.*

9. REFERENCES

Akima, H. (1970). A New Method of Interpolation and Smooth Curve Fitting Based on Local Procedures. *J. ACM, 17*(4), 589–602. doi:10.1145/321607.321609

Bi, L., & Yang, P. (2014). Accurate simulation of the optical properties of atmospheric ice crystals with the invariant imbedding T-matrix method. *Journal of Quantitative Spectroscopy and Radiative Transfer, 138*, 17-35. doi:https://doi.org/10.1016/j.jqsrt.2014.01.013

Brath, M., Ekelund, R., Eriksson, P., Lemke, O., & Buehler, S. A. (2020). Microwave and submillimeter wave scattering of oriented ice particles. *Atmos. Meas. Tech., 13*(5), 2309-2333. doi:10.5194/amt-13-2309-2020

Buehler, S. A., Defer, E., Evans, F., Eliasson, S., Mendrok, J., Eriksson, P., . . . Gasiewski, A. J. (2012). Observing ice clouds in the submillimeter spectral range: the CloudIce mission proposal for ESA's Earth Explorer 8. *Atmos. Meas. Tech., 5*(7), 1529-1549. doi:10.5194/amt-5-1529-2012

Buehler, S. A., Jiménez, C., Evans, K. F., Eriksson, P., Rydberg, B., Heymsfield, A. J., . . . Davis, C. P. (2007). A concept for a satellite mission to measure cloud ice water path, ice particle size, and cloud altitude. *Quarterly Journal of the Royal Meteorological Society, 133*(S2), 109-128. doi:https://doi.org/10.1002/qj.143

Buehler, S. A., Mendrok, J., Eriksson, P., Perrin, A., Larsson, R., & Lemke, O. (2018). ARTS, the Atmospheric Radiative Transfer Simulator – version 2.2, the

planetary toolbox edition. *Geosci. Model Dev., 11*(4), 1537-1556. doi:10.5194/gmd-11-1537-2018

Defer, E., Galligani, V. S., Prigent, C., & Jimenez, C. (2014). First observations of polarized scattering over ice clouds at close-to-millimeter wavelengths (157 GHz) with MADRAS on board the Megha-Tropiques mission. *Journal of Geophysical Research: Atmospheres, 119*(21), 12,301-312,316. doi:https://doi.org/10.1002/2014JD022353

Del Genio, A. D. (2002). GCM Simulations of Cirrus for Climate Studies. In *Cirrus*: Oxford University Press.

Ding, J., Bi, L., Yang, P., Kattawar, G. W., Weng, F., Liu, Q., & Greenwald, T. (2017). Single-scattering properties of ice particles in the microwave regime: Temperature effect on the ice refractive index with implications in remote sensing. *Journal of Quantitative Spectroscopy and Radiative Transfer, 190*, 26-37. doi:https://doi.org/10.1016/j.jqsrt.2016.11.026

Eliasson, S., Buehler, S. A., Milz, M., Eriksson, P., & John, V. O. (2011). Assessing observed and modelled spatial distributions of ice water path using satellite data. *Atmos. Chem. Phys., 11*(1), 375-391. doi:10.5194/acp-11-375-2011

Emde, C., Buehler, S. A., Davis, C., Eriksson, P., Sreerekha, T. R., & Teichmann, C. (2004). A polarized discrete ordinate scattering model for simulations of limb and nadir long-wave measurements in 1-D/3-D spherical atmospheres. *Journal of Geophysical Research: Atmospheres, 109*(D24). doi:10.1029/2004jd005140

Eriksson, P., Buehler, S. A., et al. (2020a). ARTS User Guide. Version 2.22.

Eriksson, P., Buehler, S. A., et al. (2020b). ARTS Theory Guide. Version 2.22.

Eriksson, P., Rydberg, B., Mattioli, V., Thoss, A., Accadia, C., Klein, U., & Buehler, S. A. (2020c). Towards an operational Ice Cloud Imager (ICI) retrieval product. *Atmos. Meas. Tech., 13*(1), 53-71. doi:10.5194/amt-13-53-2020

Evans, K. F., Evans, A. H., Nolt, I. G., & Marshall, B. T. (1999). The Prospect for Remote Sensing of Cirrus Clouds with a Submillimeter-Wave Spectrometer. *Journal of Applied Meteorology, 38*(5), 514-525. doi:10.1175/1520-0450(1999)038<0514:Tpfrso>2.0.Co;2

Evans, K. F., & Stephens, G. L. (1995). Microweve Radiative Transfer through Clouds Composed of Realistically Shaped Ice Crystals. Part II. Remote Sensing of Ice Clouds. *Journal of the Atmospheric Sciences, 52*(11), 2058-2072. doi:10.1175/1520-0469(1995)052<2058:Mrttcc>2.0.Co;2

Evans, K. F., & Stephens, G. L. (1995). Microwave Radiative Transfer through Clouds Composed of Realistically Shaped Ice Crystals. Part I. Single Scattering Properties. *Journal of the Atmospheric Sciences, 52*(11), 2041-2057. doi:10.1175/1520-0469(1995)052<2041:Mrttcc>2.0.Co;2

Evans, K. F., Walter, S. J., Heymsfield, A. J., & Deeter, M. N. (1998). Modeling of Submillimeter Passive Remote Sensing of Cirrus Clouds. *Journal of Applied Meteorology, 37*(2), 184-205. doi:10.1175/1520-0450(1998)037<0184:Mosprs>2.0.Co;2

Evans, K. F., Walter, S. J., Heymsfield, A. J., & McFarquhar, G. M. (2002). Submillimeter-Wave Cloud Ice Radiometer: Simulations of retrieval algorithm

performance. *Journal of Geophysical Research: Atmospheres, 107*(D3), AAC 2-1-AAC 2-21. doi:https://doi.org/10.1029/2001JD000709

Evans, K. F., Wang, J. R., O'C Starr, D., Heymsfield, G., Li, L., Tian, L., . . . Bansemer, A. (2012). Ice hydrometeor profile retrieval algorithm for high-frequency microwave radiometers: application to the CoSSIR instrument during TC4. *Atmos. Meas. Tech., 5*(9), 2277-2306. doi:10.5194/amt-5-2277-2012

Evans, K. F., Wang, J. R., Racette, P. E., Heymsfield, G., & Li, L. (2005). Ice Cloud Retrievals and Analysis with the Compact Scanning Submillimeter Imaging Radiometer and the Cloud Radar System during CRYSTAL FACE. *Journal of Applied Meteorology, 44*(6), 839-859. doi:10.1175/jam2250.1

Gasiewski, A. J. (1992). Numerical sensitivity analysis of passive EHF and SMMW channels to tropospheric water vapor, clouds, and precipitation. *IEEE Transactions on Geoscience and Remote Sensing, 30*(5), 859-870. doi:10.1109/36.175320

Gong, J., & Wu, D. L. (2017). Microphysical properties of frozen particles inferred from Global Precipitation Measurement (GPM) Microwave Imager (GMI) polarimetric measurements. *Atmos. Chem. Phys., 17*(4), 2741-2757. doi:10.5194/acp-17-2741-2017

Hegerl, G. C., Crowley, T. J., Allen, M., Hyde, W. T., Pollack, H. N., Smerdon, J., & Zorita, E. (2007). Detection of Human Influence on a New, Validated 1500-Year Temperature Reconstruction. *Journal of Climate, 20*(4), 650-666. doi:10.1175/jcli4011.1

Hioki, S., Yang, P., Kattawar, G. W., & Hu, Y. (2016). Truncation of the scattering phase matrix for vector radiative transfer simulation. *Journal of Quantitative Spectroscopy and Radiative Transfer, 183*, 70-77. doi:https://doi.org/10.1016/j.jqsrt.2016.06.011

Hogan, R. J., Mittermaier, M. P., & Illingworth, A. J. (2006). The Retrieval of Ice Water Content from Radar Reflectivity Factor and Temperature and Its Use in Evaluating a Mesoscale Model. *Journal of Applied Meteorology and Climatology, 45*(2), 301-317. doi:10.1175/jam2340.1

Hulst, H. C. v. d. (1957). *Light scattering by small particles*: Wiley.

IPCC (2014). *Climate Change 2014: Synthesis Report. Contribution of Working Groups I, II, and III to the Fifth Assessment Report of the Intergovernmental Panel on Climate Change* [Core Writing Team, R.K. Pachauri and L.A. Meyer (eds.)]. IPCC, Geneva, Switzerland, 151 pp.

Jiménez, C., Buehler, S. A., Rydberg, B., Eriksson, P., & Evans, K. F. (2007). Performance simulations for a submillimetre-wave satellite instrument to measure cloud ice. *Quarterly Journal of the Royal Meteorological Society, 133*(S2), 129-149. doi:https://doi.org/10.1002/qj.134

John, V. O., & Soden, B. J. (2006). Does convectively-detrained cloud ice enhance water vapor feedback? *Geophysical Research Letters, 33*(20). doi:https://doi.org/10.1029/2006GL027260

Kazumori, M., & English, S. J. (2015). Use of the ocean surface wind direction signal in microwave radiance assimilation. *Quarterly Journal of the Royal Meteorological Society, 141*(689), 1354-1375. doi:10.1002/qj.2445

Kikuchi, K.-i., Nishibori, T., Ochiai, S., Ozeki, H., Irimajiri, Y., Kasai, Y., . . . Shiotani, M. (2010). Overview and early results of the Superconducting Submillimeter-Wave Limb-Emission Sounder (SMILES). *Journal of Geophysical Research: Atmospheres, 115*(D23). doi:https://doi.org/10.1029/2010JD014379

L'Ecuyer, T. S., Gabriel, P., Leesman, K., Cooper, S. J., & Stephens, G. L. (2006). Objective Assessment of the Information Content of Visible and Infrared Radiance Measurements for Cloud Microphysical Property Retrievals over the Global Oceans. Part I: Liquid Clouds. *Journal of Applied Meteorology and Climatology, 45*(1), 20-41. doi:10.1175/jam2326.1

Levenberg, K. (1944). A METHOD FOR THE SOLUTION OF CERTAIN NON-LINEAR PROBLEMS IN LEAST SQUARES. *Quarterly of Applied Mathematics, 2*(2), 164-168. Retrieved from http://www.jstor.org/stable/43633451

Li, J.-L. F., Waliser, D. E., Chen, W.-T., Guan, B., Kubar, T., Stephens, G., . . . Horowitz, L. (2012). An observationally based evaluation of cloud ice water in CMIP3 and CMIP5 GCMs and contemporary reanalyses using contemporary satellite data. *Journal of Geophysical Research: Atmospheres, 117*(D16). doi:https://doi.org/10.1029/2012JD017640

Liou, K.-N. (1986). Influence of Cirrus Clouds on Weather and Climate Processes: A Global Perspective. *Monthly Weather Review, 114*(6), 1167-1199. doi:10.1175/1520-0493(1986)114<1167:Ioccow>2.0.Co;2

Liou, K.-N., & Yang, P. (2016). *Light Scattering by Ice Crystals : Fundamentals and Applications*. Cambridge, UNITED KINGDOM: Cambridge University Press.

Liou, K. N. (2002). Introduction to Atmospheric Radiation (2nd Edition). In: Elsevier.

Liu, Y., Buehler, S. A., Brath, M., Liu, H., & Dong, X. (2018). Ensemble Optimization Retrieval Algorithm of Hydrometeor Profiles for the Ice Cloud Imager Submillimeter-Wave Radiometer. *Journal of Geophysical Research: Atmospheres, 123*(9), 4594-4612. doi:https://doi.org/10.1002/2017JD027892

Miao, J., Johnsen, K. P., Buehler, S., & Kokhanovsky, A. (2003). The potential of polarization measurements from space at mm and sub-mm wavelengths for determining cirrus cloud parameters. *Atmos. Chem. Phys., 3*(1), 39-48. doi:10.5194/acp-3-39-2003

Miao, J., Rose, T., Kunzi, K., & Zimmermann, P. (2002). A Future Millimeter/Sub–Millimeter Radiometer for Satellite Observation of Ice Clouds. *International Journal of Infrared and Millimeter Waves, 23*(8), 1159-1170. doi:10.1023/A:1019655507759

Miao, J. G., Buehler, S., Kunzi, K., Ieee, & Ieee. (2001). The polarization characteristics of randomly oriented nonspherical ice particles in mm and sub-mm frequency range: Implications to the remote sensing of cirrus clouds using satellite

microwave radiometry. In *Igarss 2001: Scanning the Present and Resolving the Future, Vols 1-7, Proceedings* (pp. 2442-2444). New York: Ieee.

Michele, S. D., & Peter, B. (2005). Passive microwave radiometer channel selection based on cloud and precipitation information content estimation. In. Shinfield Park, Reading: ECMWF.

Mishchenko, M. I. (1991). Light scattering by randomly oriented axially symmetric particles. *Journal of the Optical Society of America A, 8*(6), 871-882. doi:10.1364/JOSAA.8.000871

Mishchenko, M. I., Travis, L. D., & Lacis, A. A. (2002). *Scattering, absorption, and emission of light by small particles. Michael I. Mishchenko, Larry D. Travis, Andrew A. Lacis*: Cambridge University Press.

Murtagh, D., Frisk, U., Merino, F., Ridal, M., Jonsson, A., Stegman, J., . . . Oikarinen, L. (2002). An overview of the Odin atmospheric mission. *Canadian Journal of Physics, 80*(4), 309-319. doi:10.1139/p01-157

Noel, V., Chepfer, H., Haeffelin, M., & Morille, Y. (2006). Classification of Ice Crystal Shapes in Midlatitude Ice Clouds from Three Years of Lidar Observations over the SIRTA Observatory. *Journal of the Atmospheric Sciences, 63*(11), 2978-2991. doi:10.1175/jas3767.1

Noel, V., & Sassen, K. (2005). Study of Planar Ice Crystal Orientations in Ice Clouds from Scanning Polarization Lidar Observations. *Journal of Applied Meteorology, 44*(5), 653-664. doi:10.1175/jam2223.1

Ramaswamy, V., & Ramanathan, V. (1988). Solar Absorption by Cirrus Clouds and the Maintenance of the Tropical Upper Troposphere Thermal Structure. *Journal of the Atmospheric Sciences, 46*(14), 2293-2310. doi:10.1175/1520-0469(1989)046<2293:Sabcca>2.0.Co;2

Rees, W. G. (2012). *Physical Principles of Remote Sensing*. Cambridge, UNKNOWN: Cambridge University Press.

Rodgers, C. D. (2000). *Inverse Methods for Atmospheric Sounding*: Word Scientific Publishing.

Rosenkranz, P. W. (1993). Absorption of microwaves by atmospheric gases. In M. A. Janssen (Ed.), *Atmospheric Remote Sensing by Microwave Radiometry* (pp. 37-79): John Wiley & Sons, Inc. .

Rosenkranz, P. W. (1998). Water vapor microwave continuum absorption: A comparison of measurements and models. *Radio Science, 33*(4), 919-928. doi:10.1029/98rs01182

Rydberg, B., Eriksson, P., & Buehler, S. A. (2007). Prediction of cloud ice signatures in submillimetre emission spectra by means of ground-based radar and in situ microphysical data. *Quarterly Journal of the Royal Meteorological Society, 133*(S2), 151-162. doi:https://doi.org/10.1002/qj.151

Solomon, S., Qin, D., Manning, M., Marquis, M., & Averyt, K. (2007). *AR4 Climate Change 2007: The Physical Science Basis*.

Sourdeval, O., Labonnote, L. C., Brogniez, G., Jourdan, O., Pelon, J., & Garnier, A. (2013). A variational approach for retrieving ice cloud properties from infrared

measurements: application in the context of two IIR validation campaigns. *Atmos. Chem. Phys., 13*(16), 8229-8244. doi:10.5194/acp-13-8229-2013

Stephens, G. L. (2005). Cloud Feedbacks in the Climate System: A Critical Review. *Journal of Climate, 18*(2), 237-273. doi:10.1175/jcli-3243.1

Stephens, G. L., Vane, D. G., Tanelli, S., Im, E., Durden, S., Rokey, M., . . . Marchand, R. (2008). CloudSat mission: Performance and early science after the first year of operation. *Journal of Geophysical Research: Atmospheres, 113*(D8). doi:10.1029/2008jd009982

Stroud, W. G. (1960). Initial results of the TIROS I meteorological satellite. *Journal of Geophysical Research (1896-1977), 65*(5), 1643-1643. doi:https://doi.org/10.1029/JZ065i005p01643

Sundqvist, H. (2002). On Cirrus Modeling for General Circulation and Climate Models. In *Cirrus*: Oxford University Press.

Toon, O. B., Starr, D. O., Jensen, E. J., Newman, P. A., Platnick, S., Schoeberl, M. R., . . . Pickering, K. E. (2010). Planning, implementation, and first results of the Tropical Composition, Cloud and Climate Coupling Experiment (TC4). *Journal of Geophysical Research: Atmospheres, 115*(D10). doi:10.1029/2009jd013073

Waliser, D. E., Li, J.-L. F., Woods, C. P., Austin, R. T., Bacmeister, J., Chern, J., . . . Wu, D. (2009). Cloud ice: A climate model challenge with signs and expectations of progress. *Journal of Geophysical Research: Atmospheres, 114*(D8). doi:https://doi.org/10.1029/2008JD010015

Wang, J. R., Liu, G., Spinhirne, J. D., Racette, P., & Hart, W. D. (2001). Observations and retrievals of cirrus cloud parameters using multichannel millimeter-wave radiometric measurements. *Journal of Geophysical Research: Atmospheres, 106*(D14), 15251-15263. doi:https://doi.org/10.1029/2000JD900262

Winker, D. M., Pelon, J., Coakley, J. A., Jr., Ackerman, S. A., Charlson, R. J., Colarco, P. R., . . . Wielicki, B. A. (2010). The CALIPSO Mission: A Global 3D View of Aerosols and Clouds. *Bulletin of the American Meteorological Society, 91*(9), 1211-1230. doi:10.1175/2010bams3009.1

Wu, D. L., Austin, R. T., Deng, M., Durden, S. L., Heymsfield, A. J., Jiang, J. H., . . . Waliser, D. E. (2009). Comparisons of global cloud ice from MLS, CloudSat, and correlative data sets. *Journal of Geophysical Research: Atmospheres, 114*(D8). doi:https://doi.org/10.1029/2008JD009946

Wu, D. L., Jiang, J. H., Read, W. G., Austin, R. T., Davis, C. P., Lambert, A., . . . Waters, J. W. (2008). Validation of the Aura MLS cloud ice water content measurements. *Journal of Geophysical Research: Atmospheres, 113*(D15). doi:https://doi.org/10.1029/2007JD008931

Wu, D. L., Piepmeier, J. R., Esper, J., Ehsan, N., Racette, P. E., Johnson, T. E., . . . Bryerton, E. (2019). IceCube: Spaceflight Demonstration of 883-GHz Cloud Radiometer for Future Science. In T. S. Pagano, C. D. Norton, & S. R. Babu (Eds.), *Cubesats and Smallsats for Remote Sensing Iii* (Vol. 11131). Bellingham: Spie-Int Soc Optical Engineering.

Xie, X., & Miao, J. (2011). Polarization difference due to nonrandomly oriented ice particles at millimeter/submillimeter waveband. *Journal of Quantitative Spectroscopy and Radiative Transfer, 112*(6), 1090-1098. doi:https://doi.org/10.1016/j.jqsrt.2010.11.020

Xie, X., Miao, J., & Wang, W. (2009). Microwave radiative transfer in scattering atmosphere: Effects of complex permittivity of ice spherical crystals. *Journal of Quantitative Spectroscopy and Radiative Transfer, 110*(13), 1124-1131. doi:https://doi.org/10.1016/j.jqsrt.2009.02.032

Xie, X. X., Lohnert, U., Kneifel, S., & Crewell, S. (2012). Snow particle orientation observed by ground-based microwave radiometry. *Journal of Geophysical Research-Atmospheres, 117*, 12. doi:10.1029/2011jd016369

Xie, X. X., Miao, J. G., & Wang, W. (2009). Microwave radiative transfer in scattering atmosphere: Effects of complex permittivity of ice spherical crystals. *Journal of Quantitative Spectroscopy & Radiative Transfer, 110*(13), 1124-1131. doi:10.1016/j.jqsrt.2009.02.032

Yang, P., & Liou, K. N. (1996). Geometric-optics-integral-equation method for light scattering by nonspherical ice crystals. *Applied Optics, 35*(33), 6568-6584. doi:10.1364/ao.35.006568

Yang, P., Wei, H., Huang, H.-L., Baum, B. A., Hu, Y. X., Kattawar, G. W., . . . Fu, Q. (2005). Scattering and absorption property database for nonspherical ice particles in the near- through far-infrared spectral region. *Applied Optics, 44*(26), 5512-5523. doi:10.1364/AO.44.005512

Zeng, X., Skofronick-Jackson, G., Tian, L., Emory, A. E., Olson, W. S., & Kroodsma, R. A. (2018). Analysis of the Global Microwave Polarization Data of Clouds. *Journal of Climate, 32*(1), 3-13. doi:10.1175/jcli-d-18-0293.1